Pontifícia Universidade Católica
do Rio de Janeiro


**Cesar Augusto Lampe Linhares da Fonseca**

# Analyzing the use of active pins in safety bearing

**Dissertação de Mestrado**

Dissertation presented to the Programa de Pós-Graduação em Engenharia Mecânica of the Departamento de Engenharia Mecânica do Centro Técnico Científico da PUC-Rio, as partial fulfillment of the requirements for the degree of Mestre em Engenharia Mecânica.

Advisor: Hans Ingo Weber
Co-advisor: Ilmar Ferreira Santos

Rio de Janeiro,

February de 2013

PONTIFÍCIA UNIVERSIDADE CATÓLICA
DO RIO DE JANEIRO

**Cesar Augusto Lampe Linhares da Fonseca**

# Analyzing the use of active pins in safety bearing

Thesis presented to the Programa de Pós-Graduação em Engenharia Mecânica of the Departamento de Engenharia Mecânica do Centro Técnico Científico da PUC-Rio, as partial fulfillment of the requirement for the degree of Mestre em Engenharia Mecânica. Approved by the following commission:

**Prof. Hans Ingo Weber**
Advisor
Departamento de Engenharia Mecânica – PUC-Rio

**Prof. Arthur Martins Barbosa Braga**
Departamento de Engenharia Mecânica – PUC-Rio

**Prof. Horst Ecker**
Institut für Mechanik und Mechatronik – TU Vienna

**Romulo Reis Aguiar**
Brazil Research & Geoengineering Center – Schlumberger

**Prof. José Eugênio Leal**
Coordinator of the Centro Técnico Científico - PUC-Rio

Rio de Janeiro, 15th February 2013

**Cesar Augusto Lampe Linhares da Fonseca**

Master student of the Mechanical Engineering Department of Pontifical University Catholic in Rio de Janeiro (PUC-Rio). Had his bachelor degree in Control and Automation Engineering at the same institution. Worked as intern at the brazilian national oil company, Petrobras and recently worked as project engineer in the development of diagnostic software of turbines.



Ficha Catalográfica

Fonseca, Cesar Augusto Lampe Linhares da

Analyzing the use of active pins in safety bearings / Cesar Augusto Lampe Linhares da Fonseca ; advisor: Hans Ingo Weber ; co-advisor: Ilmar Ferreira Santos. – 2013.
112 f. : il. (color.) ; 30 cm.

Dissertação (mestrado)–Pontifícia Universidade Católica do Rio de Janeiro, Departamento de Engenharia Mecânica, 2013.
Inclui bibliografia

1. Engenharia mecânica – Teses. 2. Dinâmica rotativa. 3. Rotores. 4. Atrito. 5. Impacto. 6. Velocidade crítica. 7. Roçamento. 8. Circular. I. Weber, Hans Ingo. II. Santos, Ilmar Ferreira. III. Pontifícia Universidade Católica do Rio de Janeiro. Departamento de Engenharia Mecânica. IV. Título.

CDD: 621

To my parents, family and Ana Luisa,
with love

## Acknowledgement

I wish to say thanks to Prof. Dr. Hans I. Weber and wife, Prof. Dr. Djenane Pamplona for being more than good advisors and supporters in difficult times, but also good life-giving council persons.

To Prof. Dr. José Alberto Parise for lending his laboratory to perform one of the presented experimental tests.

To Prof. Dr. Mauro Speranza and Prof. Dr. Carlos Almeida, who showed friendly support during my master years.

To my friends from the laboratory from PUC-Rio, João Luiz Ramos, Guilherme Rodrigues, Roberta Lima, Américo Cunha, Marcelo Pereira, Bruno Cayres, Leonardo Pereira, Ricardo C. Marques Mario Sandoval, Marcos Paulo Barreto, Mario Escalante, Julien Mauprivez and Marcelo Piovan. True friendships that happen once per lifetime and have created my best academics years so far.

To William Cardozo, who lend me the step motors.

To Prof. Dr. Ilmar F. Santos and Philip F. Fleischer, whose overseas help was important to conclude this work.

To my longtime friends, Ian Dunker Lyra, Ananda Altoé, Frederico Sato, Carlos Eduardo Fucci.

To our technician Mr. Wagner, without whom the laboratory would not run at all.

To Caio Ayres, who did the CAD drawings.

Also, we are thankful to the University PUC-Rio, Danmarks Tekniske Universitet and CNPq for assistance and financial support.

# Abstract

Lampe Linhares da Fonseca, Cesar Augusto; Weber, Hans Ingo (Advisor); Ferreira Santos, Ilmar (Co-advisor). **Analyzing the use of active pins in safety bearing.** Rio de Janeiro, 2013. 113p. MSc. Dissertation - Departamento de Engenharia Mecânica, Pontifícia Universidade Católica do Rio de Janeiro.

This work intends to show the possibility of using active pins in rotating machines to reduce amplitudes of orbits at critical situations through an analytical investigation with experimental validations. The pins shall operate as a safety measure when the rotor becomes unstable or starts to oscillate by any reason. To this purpose a thorough study is made of the influence of the presence of pins inside the retainer bearing. Four pins were installed within two existing test rigs in the laboratory. Their actuation comes from step motors, which insert them until a certain length in the inner side of the retainer bearing, or the gap between the rotor and the bearing wall. First, a mathematical approach of the involved phenomena is developed, providing the equations to perform numerical simulations of the system. Then, experiments where performed in the test rigs and relevant data were collected and compared to the simulation results. They showed positive accordance, which helped to validate the concept of properly inserting active pins inside the retainer bearings to avoid possible hazardous conditions, such as, friction, full annular rubbing, and abrasive effects.



## Keywords

Rotordynamics; rotors; friction; impacts; critical velocity; annular rub;

# Resumo

Lampe Linhares da Fonseca, Cesar Augusto; Weber, Hans Ingo. **Análise do uso de pinos ativos em mancais de segurança.** Rio de Janeiro, 2013. 113p. Dissertação de Mestrado - Departamento de Engenharia Mecânica, Pontifícia Universidade Católica do Rio de Janeiro.

Este trabalho pretende demonstrar a possibilidade de usar pinos ativos em máquinas rotativas de forma a reduzir as amplitudes de órbitas em situações críticas através de uma investigação analítica com validação experimental. Os pinos funcionam como medida de segurança quando o rotor se torna instável ou começa a oscilar por qualquer razão. Para este propósito, foi realizado um estudo completo da influência da presença dos pinos dentro do mancal de retenção. Quatro pinos foram posicionados em duas bancadas de testes já existentes no laboratório. A atuação deles provém de motores de passo, que os inserem até um determinado comprimento na parte interna do mancal, isto é, a folga radial entre o rotor e a parede do mancal. Primeiramente, uma análise matemática dos fenômenos envolvidos foi desenvolvida, fornecendo as equações necessárias para as simulações numéricas do sistema. Em seguida, foram realizados testes experimentais nas bancadas e informações relevantes foram adquiridas e comparadas com os resultados das simulações. Eles demonstraram estar consistentes, o que ajudou a validar o conceito de inserção de pinos ativos no mancal de segurança, de modo a evitar possíveis condições perigosas, como atrito, roçamento total e efeitos abrasivos.



## Palavras-chave

Dinâmica rotativa; rotores; atrito; impacto; velocidade crítica; roçamento circular;

*“Life is like riding a bicycle. To keep your balance you must keep moving.”*
Albert Einstein

## Contents

## List of Variables

$m$: Disc mass

$I$: Polar inertia

$I_a$: Cylinder later inertia

$\varepsilon$: Unbalance (disc center to center of mass)

$k_1$: Shaft stiffness

$k_2$: Stiffness during contact on the bearing wall

$k_p$: Stiffness during contact on a pin

$c_1$: Damping coefficient

$c_2$: Damping while impacting on the bearing wall

$c_p$: Damping while impacting on a pin

$R_b$: Bearing inner radius

$R_d$: Disc radius

$R_g$: Gyration radius

$r_0$: Gap

$J$: Moment of area of inertia

$E$: Young modulus

$L$: Shaft length

$\mathsf{A}$: Shaft cross section area

$\rho$: Shaft mass density

$x$: Horizontal coordinate of the disc center

$y$: Vertical coordinate of the disc center

$\theta$: Angular position of the disc rotor

$X$: Normalized horizontal coordinate of the disc center

$Y$: Normalized vertical coordinate of the disc center

$\varphi$: Angular position of the rotor center to the origin

| | |
|---|---|
| $\boldsymbol{r}$: | Radial position of the disc center |
| $\omega$: | Critical speed |
| $\Omega$: | Angular velocity |
| $T$: | Torque |
| $\alpha$: | Beam vibration mode; angular position of the hit on a pin |
| $\xi$: | Normalized beam length |
| $w, v$ | Displacement $x, y$ of the vibrating beam |
| $\mu$: | Friction coefficient |

# List of Figures

# List of Tables

# 1
# Introduction

The study of rotor dynamics is a topic which is getting more attention decade after decade. Rotors and axles are the main mechanical elements when converting one form of energy into another. They are present in our daily life since ancient times. They are found as components on common things from razors and small motors, to medium-size machines like the wheel hub axis of cars, electric motors, and to large-size machines like industrial compressors and pumps, aircraft engines, electric power generators, and oil well drilling rigs. Rotor dynamics has been studied more closely, in order to prevent possible inherent defects or assembly and process failures, like imbalance and thermal bucking and to avoid undesirable phenomena, such as resonance and backwards whirl. The former appears in every system model in engineering with elastic and inertia properties, as a consequence when it is excited by an oscillatory force at a specific frequency. Its response reaches endless limits if damping is not considered. The latter effect happens in rotor dynamics when the rotor collides on the wall of a catcher bearing and starts spinning against its own rotation. For the industry, this means that friction starts between elements and may cause rotor element to failure.

Nonetheless, there are several effects that may happen inside the rotating machine, making the orbit amplitude get higher and higher, which may be strange to be found or too fast to be avoided. The gap between the rotor and the stator wall is a matter of design; its size determines how much the rotor is allowed to move inside the stator so that no contact occurs. In most cases the gap must be set to the minimum, even for the biggest existing turbines, like the Itaipu dam turbines, in South Brazil. For this dam, the gap between the Francis turbine with 12m of diameter and the containment ring is around 4mm. So, the control of the vibration is a big issue regarding all these problems described above.

The mathematical study of rotating objects began with Euler's equations of rotation. The first successful models were developed only in the end of 19th century by the Swedish engineer Gustaf de Laval in 1895, and the English Henry Homan Jeffcott, Professor of Engineering at the Royal College of Science for Ireland between 1910 and 1922. Although the first work ever published on this matter was by the German engineer August Föppl, history ignores his achievements. De Laval's mechanical model consists on adding eccentrically a concentrated mass on a rotating shaft. The interaction between them can be modeled as a damped mass-spring system with the materials' properties. It shall be presented several times in this dissertation.

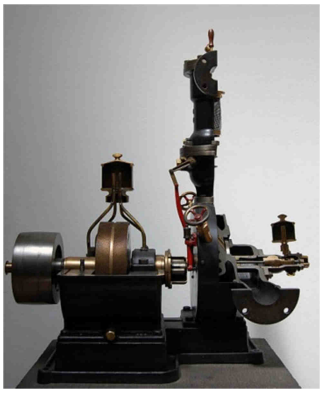

**Figure 1-1**: De Laval's steam turbine test rig [Deutsches Museum, Munich].

Since the works of Jeffcott and de Laval were widely read and their models were in fact identical, the model became known as the Jeffcott-de Laval rotor. It described the self-centering behavior of the rotor at high rotations, above the resonance. The resonance in rotating systems is explained in terms of the angular velocity, which is called the resonance condition and can appear many times. When one operates a rotating machine, the critical situations must be known and special care must be taken. In order to enhance their visualization the Campbell diagram, after Wilfred Campbell (Campbell, 1924), should be plotted. It is a chart containing all identified critical speeds as a function of the rotor rotational speed. Besides, since the rotor is excited by several oscillating forces, the lateral

movements can be seen as spectral functions. It means that the movement can be plotted not only over time but over the frequency domain. The signals collected from the sensors are analyzed using the Fourier Transform. The spectral graph illustrates which frequencies are dominant with respect to the others, see Figure 1-2.

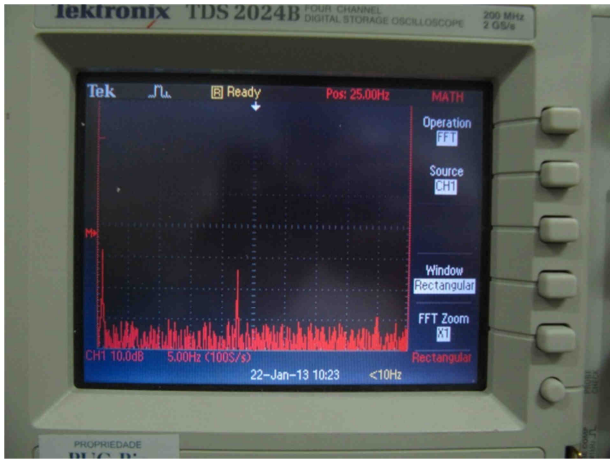


**Figure 1-2**: Raw sampling of lateral vibration data from the oscilloscope screen. The peak at 23Hz comes from imbalance, synchronous to the rotation.

In recent times, with the continuous progress in the computational field, the use of Finite-elements methods to determine the eigenfrequencies and modal frequencies spread. Nowadays, with available fast computers, it is possible to simulate the dynamics of the rotor with high precision and accuracy quite easily. Tools like Matlab® help to develop programs with its intrinsic mathematical and plotting functions. On the edge of technology lies the development of the magnetically levitated rotor, where an induced magnetic field lifts the shaft. This kind of rotor has high efficiency ratios thanks to the absence of friction in the gap. The shaft rises in the air or in vacuum, leaving negligible friction force to reduce its energy.

## 1.1. Bibliographic review

In the second half of the 20th century, the leading researchers Ehrich, Muzsinska, Bently, Lund, and Markert set for years the framework for rotor dynamics studies and most of them make big concern on how the resonance response should be lowered; the understanding of chaotic movements; and the development of bearings and controls to prevent crashes or impacts.

Ehrich's work (Ehrich, 1969) describes the influence of how supercritical resonance points present themselves and in influence.

Bently (Bently & Hatch, 2002) dedicated his entire life on experimental analysis and patented methods of acquiring data with the proximity sensor. His works with such sensors have changed the way vibration data could be gathered directly from inside the machine.

In his doctorate thesis, Szczygielsky (Szczygielsky, 1986) in Zurich analyzed the behavior of a rotor while it starts to hit several times on a plate. It worked as a limiter of the amplitudes; also, it describes the phases of impacts of the rotor during successful impacts.

Then, the work done by Fumagalli (Fumagalli, 1997) investigates the performance of the retainer bearings and verifies the applied contact models through experimental tests analyzing vibration data and force components.

In his master thesis, Meggiolaro (Meggiolaro, 1996) uses finite-element methods to combine the interaction of the rotor to the stator within a journal bearing. He exhibits the self-excited frequencies below the synchronous frequency and the response on the dynamics of the rotor.

Simon (Simon, 2000) has developed a series of numerical and practical studies of different concepts of safety bearings in his doctorate thesis. The bearings had different geometries in various polygonal shapes and he compares them to a usual round bearing.

Eckert and Popprath (Eckert & Popprath, 2007) discuss several contact models for rotor and stator and make a numerical study of them. In addition, they vary different parameters to investigate their influence in the contact dynamics and present the results with Poincaré maps.

Zülow and Liebich (Zülow & Liebich, 2009) have a similar idea to the one used in the present dissertation by adding external elements with a round top instead of active pins with solid face.

Segayer, (Segayer, 2000) has done in his dissertation the first works in the present test rigs. Then, Lahiri et al. (Lahiri, Santos, Weber, & Hartmann, 2012) presented basic studies for the concept of the present work.

This work intends to show the aspects written above with mathematical approach, a numerical simulation and experiments on test rigs.



## 1.2. Objectives and structure of this work

The goal of this work is to validate a new concept of safety bearing of rotors. The analysis is divided in three chapters. In the second chapter, a mathematical approach of the involved phenomena is developed and its numerical considerations. Physical properties like impact and friction force are presented to be used in the simulation.

The third chapter exhibits in graphs the results of the conducted simulations done, which uses the equations defined in the former chapter.

In the fourth chapter, the text describes the components of the experiments and illustrates them with sketches and photographs. The data was collected and their results from different situations are also shown in the illustrations.

The chapter number five is a compendium of work done with its final conclusions and considerations. Besides, it leaves some important notes to be used by anyone, who would like to continue from where it has stopped.

In the last part, three Appendixes detail the simulation and the experimental analysis set up with tables and CAD illustrations.

# 2
# Mathematical analysis of rotors

Every mechanical device has a mathematical model, which represents its behavior, through the equations of motion. These equations are obtained using Newton's law and Euler's law of motion or from the Lagrange variational formulation of energies. Figure 2-1 presents a sketch of the model of a vertical rotor intended to be analyzed. The elements of the rotor are its mass, its moments of inertia, together with springs and dampers. It is the simplest representation of a rotor in a test rig.



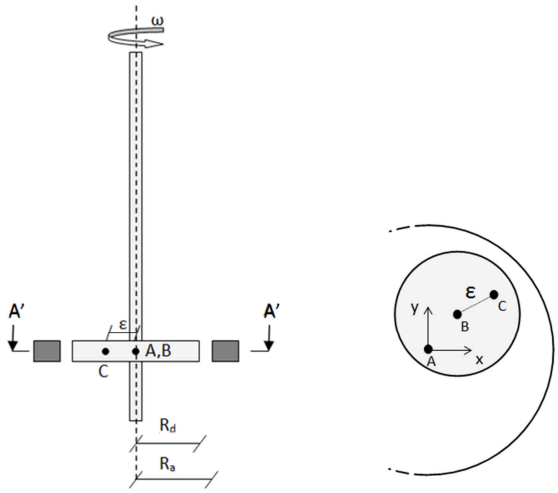


**Figure 2-1**: The vertical rotor model of a Laval rotor.

## 2.1.
## The Laval-Jeffcott model

The Laval-Jeffcott model has the following characteristics:

- The rotor shaft has to be considered as a one-dimensional massless beam;

- The rotor disc has three degrees of freedom: two displacement coordinates and a rotational one around its spinning axis ( no gyroscopic effects in this model);
- The elastic restitution coefficient comes from the geometric beam configuration;
- The damping coefficient is considered as coming from a viscous external force being applied on the disc of the rotor;
- The disc center of mass is dislocated with respect to the disc geometric center (which may arrive due to non-homogeneous mass distribution).

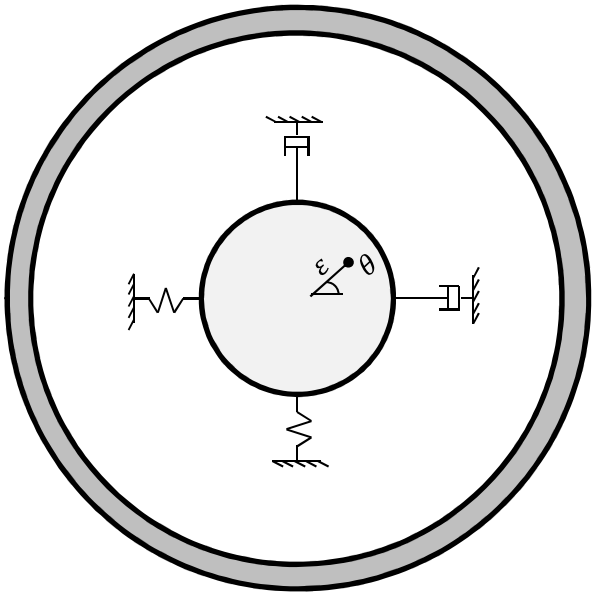


**Figure 2-2**: Representation of the implemented model.



## 2.2. The unbalanced Laval rotor at fixed coordinates

We start the modeling by establishing a fixed coordinate system, whose origin is at the center of the bearing. The bearing and the rotor are both cylindrical, one inside the other, with their symmetry axes parallel to each other (there is no tilting of the disc). The bearing is a fixed element whereas the rotor is free to move and to rotate inside the bearing. Taking into account the axial symmetry of such rotor-

bearing assembly, it is sufficient to consider a planar system with coordinates $x$ and $y$, as can be seen in Figure 2-3.

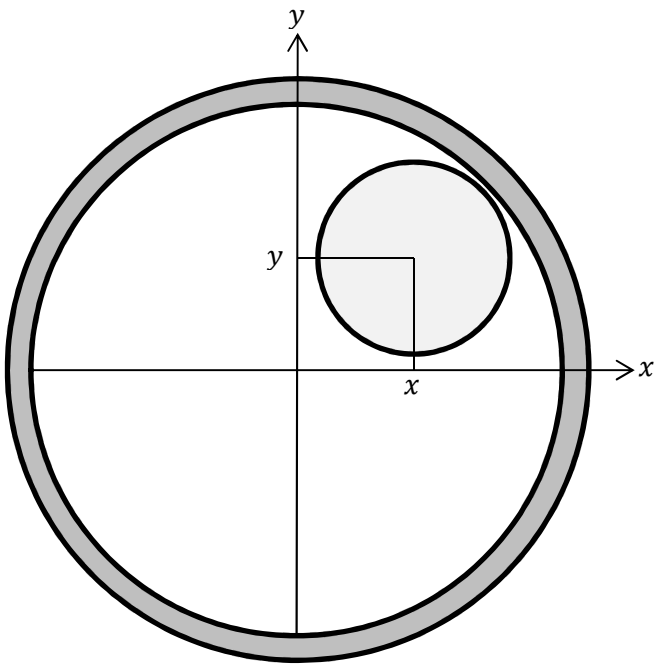


**Figure 2-3**: Coordinates of the system. The origin is at the center of the bearing. The point $(x, y)$ gives the position of the disc center.

Next, the distribution of the disc mass is not homogenous, so it has a center of mass dislocated with respect to the disc geometric center. The center of mass keeps a fixed radial distance parameter $\varepsilon$ to the center of the disc. The radius of the disc $R_d$ and the radius of the bearing $R_b$ must be known, so that the radial gap, $r_0$, is calculated as the difference between them.

By neglecting the gyroscopic effect, since the rotor moves only in a $xy$-plane, there are only two forces acting on the disc: the inertial force and the elastic force (Segayer, 2000). The former is proportional to the eccentric position $\varepsilon$ and to the disc squared angular velocity. The latter is the reaction of the shaft when it bends or deforms and its vector is positioned on the disc center. Further details are shown later in this chapter.

The elastic force is a linear function of $\boldsymbol{r}$, the radial distance of the disc center to the origin. However, when the rotor moves farther from the gap, $r_0$ or $|\boldsymbol{r}| \geq r_0$, the interaction of the between the rotor and the bearing wall, which

changes the elastic force. It is still a linear function, but with steeper slope. When the rotor displacement is greater than $r_0$, a contact between the disc edge and the bearing wall takes place. The disc penetration into the bearing wall can also be modeled as an elastic force with a much higher stiffness coefficient. In other words, the disc-wall contact stiffness is much bigger than the stiffness of the beam.

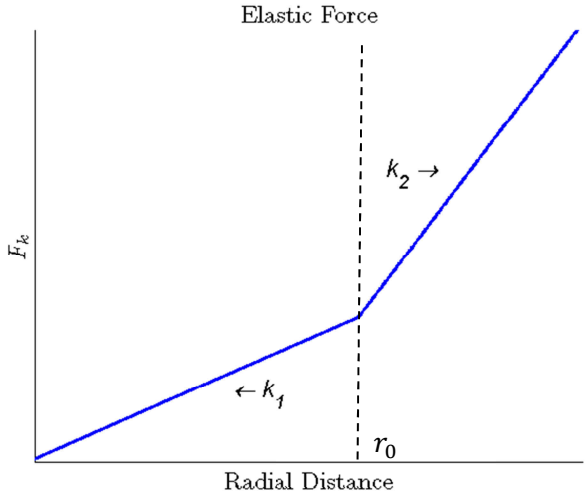


**Figure 2-4**: The elastic force variation with the radial distance $r$. (Isaksson, 1994)

Figure 2-4 is a qualitative representation of the elastic force as a function of the disc spatial displacement. Let us express the force $F_k$ as

$$\boldsymbol{F}_k = \begin{cases} k_1|\boldsymbol{r}|, & \text{if } r < r_0 \\ k_2|\boldsymbol{r}| - (k_2 - k_1)r_0, & \text{if } r \geq r_0. \end{cases} \quad (1)$$

It is important to stress that the model used in this work considers the bearing as a fixed massless object with elastic properties. Other models like one studied by (Isaksson, 1994) consider that the bearing is able to move with respect to the origin. The consideration of the angular velocity, when impact occurs, will be dealt later in Section 2.7.

## 2.3.
## Basic equations of rotor dynamics

### 2.3.1.
### Rotor's equation without contact

To obtain the equations of motion, we begin by locating the origin of the coordinate system at the center of the bearing. Figure 2-5 shows the bearing and the disc center displaced by $x$ at the horizontal direction and by $y$ at the vertical direction on the plane of the figure. Next we state the Newton's laws for our two-dimensional system:

$$F_x = m\frac{d^2}{dt^2}(x + \varepsilon\cos\theta), \tag{2}$$

$$F_y = m\frac{d^2}{dt^2}(y + \varepsilon\sin\theta). \tag{3}$$

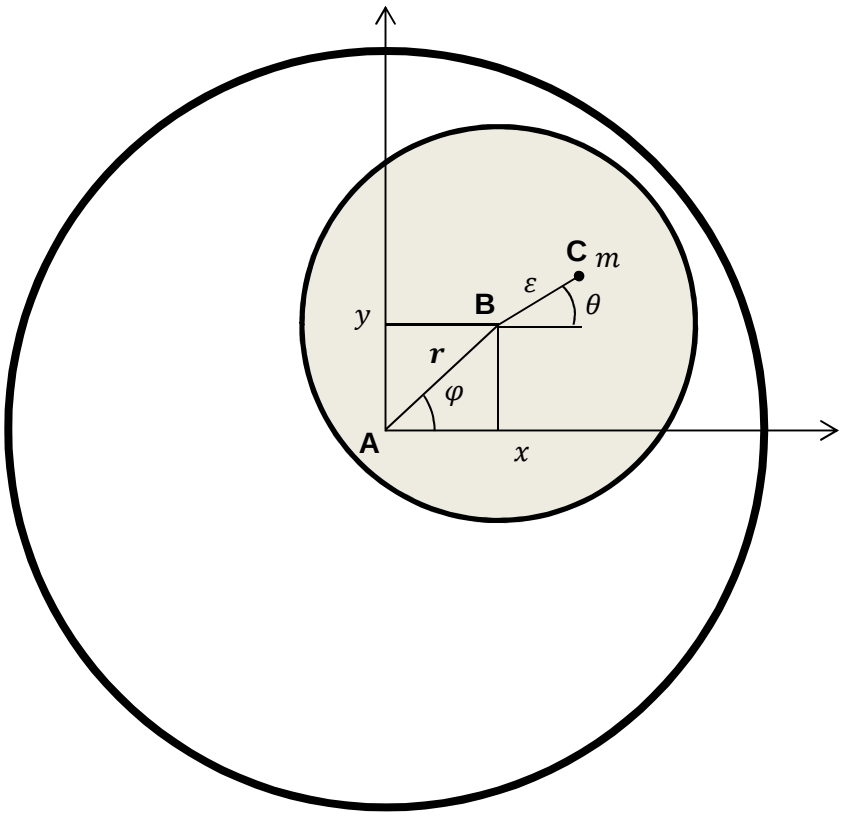


**Figure 2-5**: The disc and the bearing at a random position. The point A is the origin and the center of the bearing; Point B is the center of the rotor and where the shaft is fixed; Point C is where the center of mass $m$ is located.

The forces in equations (4) and (5) below are the elastic and damping forces caused by the rotor axis and from the environment:

$$F_x = -(k_1 x + c_1 \dot{x}), \tag{4}$$

$$F_y = -(k_1 y + c_1 \dot{y}). \tag{5}$$

Then equations (2) and (3) can be combined with (4) and (5), resulting in the following system of differential equations:

$$m\ddot{x} + c_1\dot{x} + k_1 x = m\varepsilon\ddot{\theta}\sin\theta + m\varepsilon\dot{\theta}^2\cos\theta, \tag{6}$$

$$m\ddot{y} + c_1\dot{y} + k_1 y = -m\varepsilon\ddot{\theta}\cos\theta + m\varepsilon\dot{\theta}^2\sin\theta. \tag{7}$$

These are the usual equations of rotor dynamics for the Laval-Jeffcott rotor. However, there is no equation for the angular acceleration of the rotor. For most analysis in rotor dynamics, either a constant angular acceleration or a constant angular velocity is applied. Also, the system is considered orthotropic, because the elastic constant is the same for both equations.

Nevertheless, the angular velocity is not considered constant in this work. To take into account its variation in time, a third equation of motion regarding the rotor moment of inertia and the torque applied has to be written as:

$$I\ddot{\theta} = T_a + \varepsilon k_1(y\cos\theta - x\sin\theta), \tag{8}$$

where $I$ is the polar rotor moment of inertia, given for a disc by

$$I = {}^1\!/_2\, m{R_d}^2 \tag{9}$$

and $T_a$ is the torque supplied by the motor.

### 2.3.2.
### Unbalanced response without damping and impact

The first solution to be analyzed here comes from equations (6) and (7), without the damping term. We consider a constant angular velocity, so we have $\ddot{\theta} = 0$. We wish to obtain the particular solutions of eqs. (6) and (7). First we introduce the resonance frequency $\omega$ and the actual angular velocity $\Omega$. The angular velocity relationship $\eta$ is commonly written as

$$\omega = \sqrt{\frac{k_1}{m}} \tag{10}$$

$$\eta = \sqrt{\frac{\Omega}{\omega}}. \tag{11}$$

Now, the particular solutions are obtained from the "ansatz"

$$\begin{aligned} x_\varepsilon &= \varepsilon\left(\frac{\eta^2}{1-\eta^2}\right)\cos\theta t, \\ y_\varepsilon &= \varepsilon\left(\frac{\eta^2}{1-\eta^2}\right)\sin\theta t, \end{aligned} \tag{12}$$

so that

$$|r_\varepsilon| = \sqrt{x_\varepsilon^2 + y_\varepsilon^2} = \left|\varepsilon\left(\frac{\eta^2}{1-\eta^2}\right)\right|. \tag{13}$$

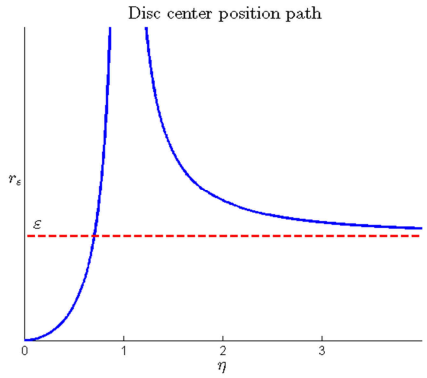


**Figure 2-6**: Magnitude of the orbit radius $r_\varepsilon$ as function of angular velocity relationship $\eta$.

Figure 2-6 is the representation of equation (13) which shows that at higher angular velocities, well above the resonance frequency $\omega$, the radial displacement reaches $\varepsilon$. When $\eta$ is equal to 1, it is said that the rotor is at the critical speed, which equals the resonance frequency and the rotor's amplitude is infinite.

### 2.3.3. Response with damping

From equation (6) and (7), the dynamical response is similar to the previous case but the radial distance does not grow to infinity as it crosses the the critical speed. Due to the presence of damping, it can be adjusted a limit for amplitude range increasing or decreasing the damping coefficient.

The solution is similar to the case before, but it can be better handled using polar coordinates $r, \varphi$. Introducing the position of the disc center as a complex number $r = x + iy$ we may transform eqs. (6) and (7) into

$$\ddot{r} + {}^{c_1}/_{m}\,\dot{r} + \omega^2 r = \varepsilon\Omega^2 e^{i\Omega t}. \tag{14}$$

$$\varphi = \tan^{-1} {}^{y}/_{x} \tag{15}$$

A damping factor

$$\xi = \frac{c_1}{2m\omega} \tag{16}$$

can be introduced in equation (16), becoming

$$\ddot{r} + 2\xi\omega\dot{r} + \omega^2 r = \varepsilon\Omega^2 e^{i\Omega t}. \tag{17}$$

The homogeneous solution of equation (17) is obtained through its characteristic equation:

$$\lambda^2 + 2\xi\omega\lambda + \omega^2 = 0, \tag{18}$$

whose the solution is

$$\lambda_{1,2} = \delta_d \pm i\omega_d, \tag{19}$$

which can be written as

$$\lambda_{1,2} = -\underbrace{\xi\omega}_{\delta_d} \pm i\,\underbrace{\omega\sqrt{\xi^2 - 1}}_{\omega_d}. \tag{20}$$

The square root in the above eq. classifies the damping as supercritical, critical or subcritical:

- When $\xi$ is greater than 1, then the system is considered supercritically damped. There are no overshoots and almost no oscillations.
- When $\xi$ is equal to 1, there is a double eigenvalue; this is the critical damping. So, if $\xi = 1$, then $c_1 = 2m\omega$.
- When $\xi$ is smaller than 1, the system becomes oscillatory and the smaller $\xi$ gets, the greater the peak becomes.

The homogeneous solution of equation (17) for the center of the disk is

$$r_h = Ae^{\lambda_1 t} + Be^{\lambda_2 t}. \tag{21}$$

For now, we are interested in the particular solution and not in the transient response. The particular solution of equation (17) is of the form

$$r(t) = r_\varepsilon(t)\, e^{i\Omega t}. \tag{22}$$

With this “ansatz” the radial equation is written

$$r_\varepsilon = \frac{\varepsilon\eta^2}{(1-\eta^2)+i2\xi\eta}. \tag{23}$$

In Figure 2-7, the stationary values of orbits radii given by (23) are plotted for different values of the damping factor.

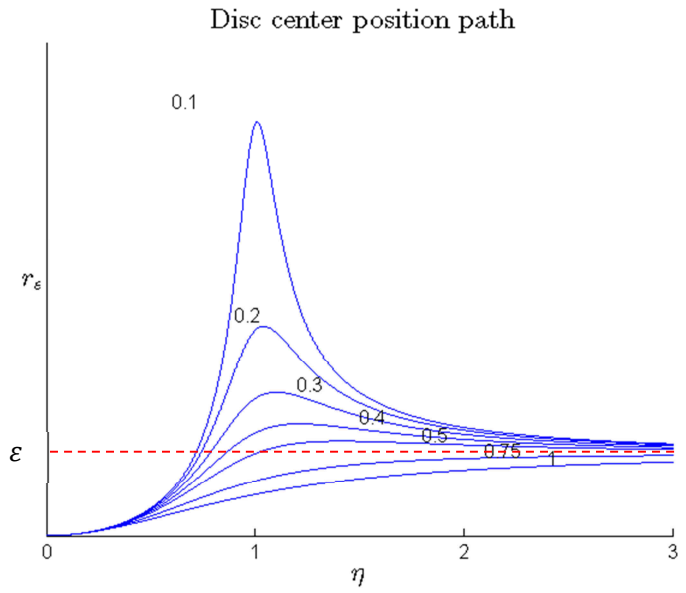


**Figure 2-7**: Orbit radius as a function of the angular velocity for different damping factors $\xi$ at certain angular velocity relationship $\eta$.

It can be seen that all curves are asymptotic to the value $\varepsilon$.

## 2.4. Rotor passage through the resonance

In the previous sections, it was shown that the critical velocity and resonance point, where the maximal values of radii occur, require special attention; therefore, it is a situation which should avoided. However, it is rather common that a machine shall operate above the critical speed. It is important not to remain near the resonance point, so one must know how fast the rotor must be accelerated in order to reduce the high vibration amplitudes. In this case we need to combine

homogeneous and particular solutions of equations and consider also the angular acceleration of the rotor.

The acceleration on rotors comes from an external source of power, like an electric motor or combustion engine providing torque. Although there are influences of the electric grid or from thermodynamical effects, it is supposed the torque is constantly supplied to the system. We start analyzing the transient part of the motion by solving equation (17) for $r(t)$ with the initial conditions $r(0) = 0$, $\dot{r}(0) = 0$ for the sum of the homogenous (21) and the particular (22) solutions, disregarding for the moment the angular acceleration.

$$r(t) = \left(Ae^{\lambda_1 t} + Be^{\lambda_2 t}\right) + r_\varepsilon e^{\mathrm{i}\Omega t}. \tag{24}$$

To obtain the integration constants $A$ and $B$ we need

$$\begin{aligned}\dot{r}(t) &= \left(A\lambda_1 e^{\lambda_1 t} + B\lambda_2 e^{\lambda_2 t}\right) + r_\varepsilon \mathrm{i}\Omega e^{\mathrm{i}\Omega t} \\ &= \delta_d e^{\delta_d t}(A\omega_d e^{\omega_d t} + B\omega_d e^{-\omega_d t}) + \\ &\quad + i\omega_d e^{\delta_d t}(A\omega_d e^{\omega_d t} - B\omega_d e^{-\omega_d t}) r_\varepsilon \mathrm{i}\Omega e^{\mathrm{i}\Omega t}\end{aligned} \tag{25}$$

Hence,

$$r(0) = A + B + r_\varepsilon \tag{26}$$

$$\dot{r}(0) = \delta_d(A + B) + i\omega_d(A - B) + i\Omega r_\varepsilon. \tag{27}$$

For this special case the solution to the system is

$$A = -r_\varepsilon\left(\frac{1}{2} + \frac{\Omega}{2\omega_d} - \frac{\delta_d}{2i\omega_d}\right) = -r_\varepsilon\left(\frac{1}{2} + \frac{\eta - i\xi}{2\sqrt{1-\xi^2}}\right) \tag{28}$$

$$B = -r_\varepsilon\left(\frac{1}{2} - \frac{\Omega}{2\omega_d} + \frac{\delta_d}{2i\omega_d}\right) = -r_\varepsilon\left(\frac{1}{2} - \frac{\eta - i\xi}{2\sqrt{1-\xi^2}}\right). \tag{29}$$

This will give in (24) is the complete solution to the response to an unbalanced force for a rotor that reaches the critical speed centered and suddenly is released.

However, to establish a constant angular velocity the torque $T_a$ given must equilibrate the torque of the unbalanced force. Then from equation (8) it must be given by

$$T_a \equiv \varepsilon k_1 (x \sin\theta - y \cos\theta),$$

so that the angular acceleration $\ddot{\theta}$ remains zero.

Now, if the rotor has a high unbalance parameter or a weak power source, it is possible that the rotor stays at great amplitudes without surpassing the resonance point. This is called the Sommerfeld effect. There is, though, a minimum torque which was obtained numerically by (Markert, Pfützner, & Gasch, 1980) with the approximation

$$T_{min} \approx 1.3 \left(\frac{\varepsilon}{R_g}\right)^{\frac{4}{3}} R_g^2 \omega^2 m, \tag{30}$$

or non-dimensionally written

$$\bar{T}_{min} \approx 1.3 \left(\frac{\varepsilon}{R_g}\right)^{\frac{4}{3}}. \tag{31}$$

## 2.5. The gyroscopic effect

All equations in the previous section constitute a representation of the rotor, which has its mass concentrated in one point or when the disc is located on a position in which it does not tilt, see Figure 2-8 . Nevertheless, in a real system, it is not possible to build a rotor's disc without any eccentric mass in just one point, or assemble it exactly at a non-tilting position. Figure 2-9 identifies the angles and tilts movements from the rotor.

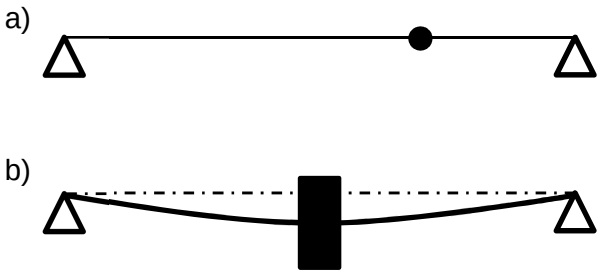


**Figure 2-8**: In a): A rotor with mass as a point. In b): A rotor's disk staying in a position, which it does not tilt at lower speeds.

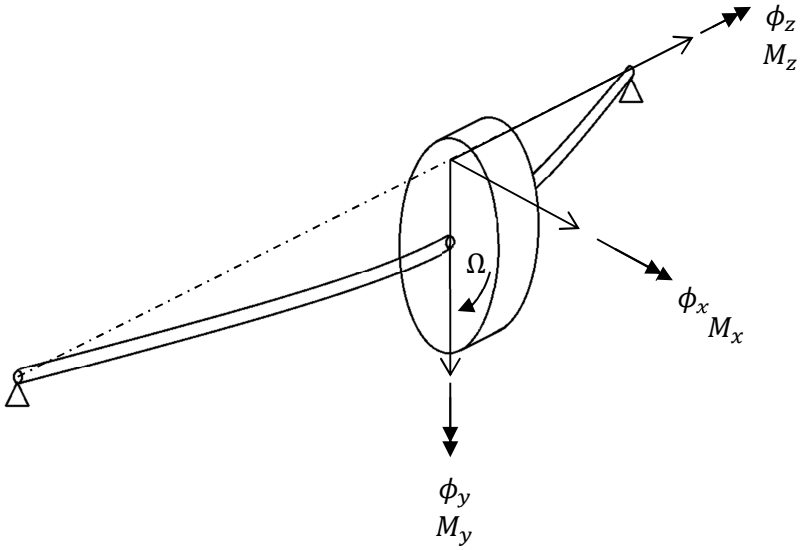


**Figure 2-9**: Orientation of the torques and angles (Gasch, Nordman, & Pfützner, Rotordynamik, 2002).



### 2.5.1. Equations of motion

The first step to build the equations with the gyroscopic effect is to require the dependence of the displacement with the rotation caused by the forces and momenta on the disc. The corresponding matrix is written as

$$\underline{\boldsymbol{f}} = \begin{bmatrix} k_{11} & k_{12} & & \\ k_{21} & k_{22} & & \\ & & k_{11} & -k_{12} \\ & & -k_{21} & k_{22} \end{bmatrix} \begin{bmatrix} x \\ \phi_x \\ y \\ \phi_y \end{bmatrix}. \tag{32}$$

For a homogeneous cantilever beam, the elastic coefficients are

$$k_{11} = \frac{12EJ}{L^3}; \qquad k_{22} = \frac{4EJ}{L}; \qquad k_{12} = k_{21} = \frac{6EJ}{L^2}.$$

Besides the coordinate system of Figure 2-9, assuming a new coordinate system $S$ located on the undeformed shaft position and the disc center is then displaced with $x_S$ and $y_S$ with respect to the origin and tilted with small angles $\phi_x$ and $\phi_y$, so that the sequence of rotation loses its importance, see Figure 2-10 and Figure 2-11.

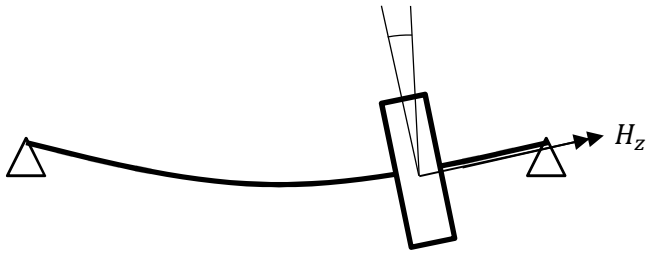


**Figure 2-10**: Tilting angle.

Now the momenta coordinates are

$$\begin{aligned} \boldsymbol{H}_{x'} &= I_a \dot{\phi}_{x'_S} \ , \\ \boldsymbol{H}_{y'} &= I_a \dot{\phi}_{y'_S} \ , \\ \boldsymbol{H}_{z'} &= I \dot{\phi}_{z'_S} \ , \end{aligned} \tag{33}$$

where $I_a$ and $I$ are defined as

$$I = \frac{m}{2} R_d^2, \ \ I_a = \frac{m}{12}\left(3R_d^2 + h_c^2\right).$$

Where $h_c$ is the thickness of the disc. The inertia tensor can be written in this coordinate system as

$$\underline{\boldsymbol{I}} = \begin{bmatrix} I_a & 0 & 0 \\ 0 & I_a & 0 \\ 0 & 0 & I \end{bmatrix}. \tag{34}$$

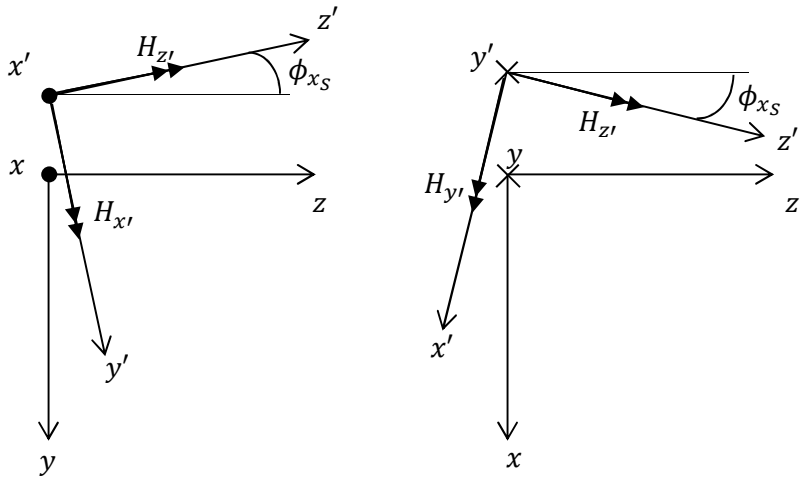


**Figure 2-11**: Momenta components.



In this chapter we will consider the momenta component $H_z = H_{z'}$ due to small angles and setting $\dot{\phi}_z = \Omega$ constant. Then

$$\begin{aligned} H_y &= H_{y'} + H_{z'}\phi_{x_s} \ , \\ H_x &= H_{x'} - H_{z'}\phi_{y_s} \ . \end{aligned} \tag{35}$$

and

$$\begin{aligned} H_y &= I_a\dot{\phi}_{y_s} + I\Omega\phi_{x_s} \ , \\ H_x &= I_a\dot{\phi}_{x_s} - I\Omega\phi_{y_s} \ . \end{aligned} \tag{36}$$

Since

$$\boldsymbol{M} = \frac{d\boldsymbol{H}}{dt},$$

then

$$\begin{aligned} M_y &= I_a\ddot{\phi}_{y_s} + I\Omega\dot{\phi}_{x_s} \ , \\ M_x &= I_a\ddot{\phi}_{x_s} - I\Omega\dot{\phi}_{y_s} \ . \end{aligned} \tag{37}$$

Writing equations (37) together with the Newton's laws in matricial form,

$$\begin{bmatrix} F_x \\ M_y \\ F_y \\ M_x \end{bmatrix} = \begin{bmatrix} m & 0 & & \\ 0 & I_a & & \\ & & m & 0 \\ & & 0 & I_a \end{bmatrix} \begin{bmatrix} \ddot{x}_s \\ \ddot{\phi}_{y_s} \\ \ddot{y}_s \\ \ddot{\phi}_{x_s} \end{bmatrix} + \begin{bmatrix} & & 0 & 0 \\ & & 0 & \Omega I \\ 0 & 0 & & \\ 0 & -\Omega I & & \end{bmatrix} \begin{bmatrix} \dot{x}_s \\ \dot{\phi}_{y_s} \\ \dot{y}_s \\ \dot{\phi}_{x_s} \end{bmatrix},$$

or

$$\boldsymbol{f} = \underbrace{\boldsymbol{M}}_{\textbf{Mass Matrix}} \ddot{\boldsymbol{q}} + \underbrace{\boldsymbol{G}}_{\textbf{Gyroscopic Matrix}} \dot{\boldsymbol{q}}. \tag{38}$$

Finally, to build the equation of motion, a term containing the stiffness matrix (32) is added to equation (38),

$$\begin{bmatrix} m & 0 & & \\ 0 & I_a & & \\ & & m & 0 \\ & & 0 & I_a \end{bmatrix} \begin{bmatrix} \ddot{x}_s \\ \ddot{\phi}_{y_s} \\ \ddot{y}_s \\ \ddot{\phi}_{x_s} \end{bmatrix} + \begin{bmatrix} & & 0 & 0 \\ & & 0 & \Omega I \\ 0 & 0 & & \\ 0 & -\Omega I & & \end{bmatrix} \begin{bmatrix} \dot{x}_s \\ \dot{\phi}_{y_s} \\ \dot{y}_s \\ \dot{\phi}_{x_s} \end{bmatrix} + \begin{bmatrix} k_{11} & k_{12} & & \\ k_{21} & k_{22} & & \\ & & k_{11} & -k_{12} \\ & & -k_{21} & k_{22} \end{bmatrix} \begin{bmatrix} x \\ \phi_x \\ y \\ \phi_y \end{bmatrix} = 0, \tag{39}$$

or, expressed in terms of the polar coordinates,

$$\begin{aligned} r_s &= x_s + iy_s \ , \\ r &= x + iy \ , \\ \phi_s &= \phi_{x_s} + i\phi_{y_s} \ , \\ \phi &= \phi_x + i\phi_y \ , \end{aligned} \tag{40}$$

$$\begin{bmatrix} m & 0 \\ 0 & I_a \end{bmatrix} \begin{bmatrix} \ddot{r}_s \\ \ddot{\phi}_s \end{bmatrix} + \begin{bmatrix} 0 & 0 \\ 0 & I\Omega \end{bmatrix} \begin{bmatrix} \dot{r}_s \\ \dot{\phi}_s \end{bmatrix} + \begin{bmatrix} k_{11} & -ik_{12} \\ ik_{12} & k_{22} \end{bmatrix} \begin{bmatrix} r \\ \phi \end{bmatrix} = 0. \tag{41}$$

With the unbalance condition

$$r_s = r + \varepsilon e^{i(\Omega t + \beta)} \tag{42}$$

and with a constant initial angle tilt $\alpha$, which comes from bad assembly or bent shaft, from the disc to the shaft

$$\phi_s = \phi + \alpha e^{i(\Omega t + \gamma)}, \tag{43}$$

it becomes the commonly known representation of a rotor equation system

$$\begin{bmatrix} m & 0 \\ 0 & I_a \end{bmatrix}\begin{bmatrix} \ddot{r} \\ \ddot{\phi} \end{bmatrix} + \begin{bmatrix} 0 & 0 \\ 0 & I\Omega \end{bmatrix}\begin{bmatrix} \dot{r} \\ \dot{\phi} \end{bmatrix} + \begin{bmatrix} k_{11} & -ik_{12} \\ ik_{12} & k_{22} \end{bmatrix}\begin{bmatrix} r \\ \phi \end{bmatrix} = \Omega^2 \begin{bmatrix} m\varepsilon e^{i(\Omega t+\beta)} \\ (I_a - I)\alpha e^{i(\Omega t+\gamma)} \end{bmatrix} \tag{44}$$

or written as

$$\underline{\boldsymbol{M}}\begin{bmatrix} \ddot{r} \\ \ddot{\phi} \end{bmatrix} + \underline{\boldsymbol{G}}\begin{bmatrix} \dot{r} \\ \dot{\phi} \end{bmatrix} + \underline{\boldsymbol{K}}\begin{bmatrix} r \\ \phi \end{bmatrix} = \boldsymbol{F}(\Omega, \mathrm{t}). \tag{45}$$

## 2.6. The natural frequencies of a beam as a continuous rotor

The model of a beam with distributed mass and excited by a distributed force $q(z,t)$ is

$$EJ\frac{\partial^4 w}{\partial z^4} + \frac{\partial^2 w}{\partial t^2} = q(z,t), \tag{46}$$

where the product of Young modulus $E$ and the area moment of inertia $J$ is constant throughout the domain. Then by defining

$$\xi = \frac{z}{L}; \quad \eta = \frac{w}{L}; \quad \tau = \frac{t}{L^2}\sqrt{\frac{EJ}{\rho A}}; \quad \psi = \frac{q(z,t)L^3}{EJ},$$

equation (46) becomes

$$\frac{\partial^4 \eta}{\partial \xi^4} + \frac{\partial^2 \eta}{\partial \tau^2} = \psi(\xi, \tau). \tag{47}$$

Through the method of separation of variables, we take the solution as

$$\eta(\xi,\tau) = \chi(\xi)\Theta(\tau) \tag{48}$$

Combining eqs. (47) and (48), one gets

$$\frac{\chi^{IV}(\xi)}{\chi(\xi)} = -\frac{\ddot{\Theta}(\tau)}{\Theta(\tau)} = \zeta^2, \tag{49}$$

where $\gamma$ is a constant given by

$$\zeta \equiv \alpha^2 = \sqrt{\frac{\rho A}{EJ}}\,\omega L^2. \tag{50}$$

The solutions for the spatial coordinate $\chi(\xi)$ are presented as

$$\chi(\xi) = a_1 \sin\alpha\xi + a_2 \cos\alpha\xi + a_3 \sinh\alpha\xi + a_4 \cosh\alpha\xi. \tag{51}$$

We may have infinite solutions for the parameters $\alpha$, each of them $(\alpha_1, \alpha_2, \alpha_3, \ldots)$ representing a natural frequency of vibration. To determine them, one must apply the boundary conditions for each case of beam configuration. They are presented on Table 2.1.

**Table 2.1**: Numerical frequencies for $\alpha^2$ for some boundary conditions. (Thomson, 1972).

| **Beam boundary conditions** | $\boldsymbol{\alpha_1^2}$ | $\boldsymbol{\alpha_2^2}$ | $\boldsymbol{\alpha_3^2}$ |
|---|---|---|---|
| Simply supported | 9.87 | 39.5 | 88.9 |
| Free-free | 22.4 | 61.7 | 121.0 |
| Cantilever | 3.52 | 22.4 | 61.7 |
| Hinged-free | 0 | 15.4 | 50.0 |

On rotors, one cannot observe as a two-dimensional plane problem, so there are two equations that need to be analyzed, one for each coordinate axis. The point $\boldsymbol{C}(z)$ is the center of mass of the shaft section for a $z$ position.

$$EJ\frac{\partial^4 w}{\partial z^4} + \rho\frac{\partial^2 w_C}{\partial t^2} = 0, \tag{52}$$

$$EJ\frac{\partial^4 v}{\partial z^4} + \rho\frac{\partial^2 v_C}{\partial t^2} = 0. \tag{53}$$

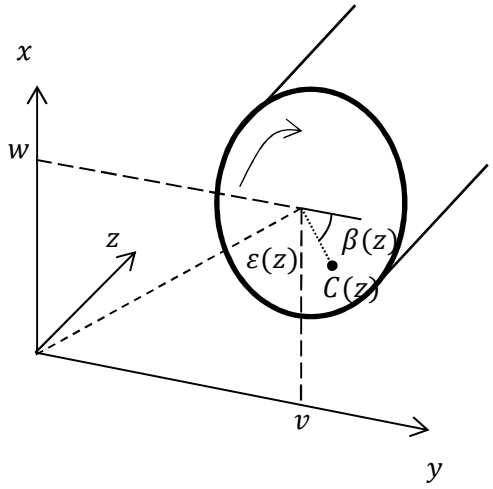


**Figure 2-12**: A shaft section with displacements $w$ and $v$ and eccentricity $\varepsilon$ and constant mass density $\rho$ (Gasch, Nordman, & Pfützner, Rotordynamik, 2002).

Since the relationships between $w_C$ and $w$, $v_C$ and $v$ are given by

$$w_C = w + \varepsilon(z)\cos(\Omega t + \beta), \tag{54}$$

$$v_C = v + \varepsilon(z)\sin(\Omega t + \beta), \tag{55}$$

we differentiate them twice with respect to time and insert them in eqs. (52) and (53), getting

$$EJw'''' + \rho\ddot{w} = \varepsilon(z)\rho\Omega^2\cos\big(\Omega t + \beta(z)\big), \tag{56}$$

$$EJv'''' + \rho\ddot{v} = \varepsilon(z)\rho\Omega^2 \sin\big(\Omega t + \beta(z)\big). \tag{57}$$

With the polar coordinate $\zeta = w(z) + iv(z)$ and with eqs. (56) and (57) we have

$$EI\zeta'''' + \rho\ddot{\zeta} = \Omega^2\varepsilon(z)e^{i(\Omega t+\beta(z))}. \tag{58}$$

The equation above can be solved by the method of separation of variables, which results in the following expression

$$\zeta(z,t) = \sum_n \varphi_n(z)\left(\frac{\Omega^2}{\omega^2 - \Omega^2}\right)\varepsilon_{\text{gen},n}(z)e^{i(\Omega t+\beta(z))}, \tag{59}$$

where the $\varphi_n(z)$ are the modal eigenfunctions given from the solution of eq. (51), according to the boundary conditions imposed and using the associated parameters $\alpha_n$ from Table 2.1. Also, a generalized eccentricity $\varepsilon_{\text{gen}}$ is defined as

$$\varepsilon_{\text{gen},n} = \frac{u_{\text{gen},n}}{m_{\text{gen},n}}, \tag{60}$$

where

$$u_{\text{gen},n} = \int \mu(z)\varepsilon(z)e^{i(\Omega t+\beta(z))}\varphi_n^2(z)\,dz \tag{61}$$

And

$$m_{\text{gen},n} = \int \mu(z)\varphi_n^2(z)\,dz. \tag{62}$$

## 2.7. The contact state

So far, the equations written were the basic ones of rotor dynamics. However, as seen before, because of the unbalance and elastic properties, amplitudes can reach high values as the rotation increases. In the real world it is important to restrain high amplitudes, due to different reasons such as safety measures. One does not

want a machine which oscillates significantly, that may cause small parts to get loose. Also, the rotor must be supported by bearings, either by sleeve or rolling bearings. In the case of the sleeve bearing, the thin layer of oil works as an external stiffness element. Even though, with amplitudes getting higher and higher, it is possible that the rotor collides with the bearing wall and starts to rub partially or completely. On the contact state, the rotor is also under the influence of the friction force which appears orthogonally against the rotational velocity.

The friction force is modeled as the dry friction, following the analysis of (Isaksson, 1994). The friction force maximal value is proportional to the normal force or to the impact force by a constant coefficient $\mu$:

$$\boldsymbol{f} = \mu \boldsymbol{N}. \tag{63}$$

The normal force exists only when the radial position of the disc center overpasses the difference between the radii (gap), $r \geq r_0$. In this case, the normal force $\boldsymbol{N}$ points to the disc center:

$$\boldsymbol{N} = (k_2 - k_1)(|\boldsymbol{r}| - r_0)\frac{-\boldsymbol{r}}{|\boldsymbol{r}|}, \qquad \text{if } |\boldsymbol{r}| \geq r_0. \tag{64}$$

We also take

$$\boldsymbol{N} = \boldsymbol{0}, \qquad \text{for } |\boldsymbol{r}| < r_0.$$

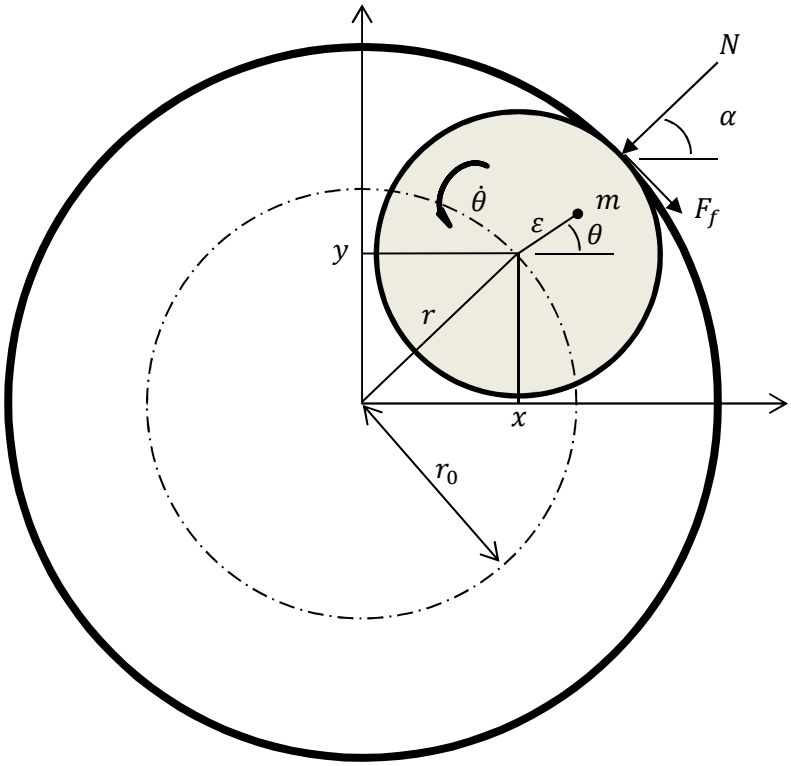


**Figure 2-13**: The contact state with the configuration of the normal and friction forces.

Figure 2-13 shows the configuration of forces when $r \geq r_0$. The normal force points to the center of the disc and the friction force must be along the opposite direction of the velocity at the contact point. Thus, the velocity of the edge of the disc is calculated by the expression:

$$\boldsymbol{V}_{\text{edge}} = \widetilde{\boldsymbol{\Omega}}\boldsymbol{R_d} + \boldsymbol{V_B}. \tag{65}$$

The operator ~ is the matricial representation of the cross product:

$$A = \begin{bmatrix} x_1 \\ x_2 \\ x_3 \end{bmatrix}, \qquad B = \begin{bmatrix} y_1 \\ y_2 \\ y_3 \end{bmatrix}$$

$$A \times B = \tilde{A}B = \begin{bmatrix} 0 & -x_3 & x_2 \\ x_3 & 0 & -x_1 \\ -x_2 & x_1 & 0 \end{bmatrix} \begin{bmatrix} y_1 \\ y_2 \\ y_3 \end{bmatrix}.$$

The friction force is mathematically expressed by

$$\boldsymbol{F}_{\mathrm{f}} = -\mu|\boldsymbol{N}| \cdot \frac{\boldsymbol{V}_{\mathrm{edge}}}{\left|\boldsymbol{V}_{\mathrm{edge}}\right|}. \tag{66}$$

The equations (6), (7) and (8) are rewritten to include both impact forces on them:

$$m\ddot{x} + c_1\dot{x} + k_1 x + |\boldsymbol{N}|(\cos\alpha - \mu\sin\alpha) = m\varepsilon\ddot{\theta}\sin\theta + m\varepsilon\dot{\theta}^2\cos\theta, \tag{67}$$

$$m\ddot{y} + c_1\dot{y} + k_1 y + |\boldsymbol{N}|(\sin\alpha + \mu\cos\alpha) = -m\varepsilon\ddot{\theta}\cos\theta + m\varepsilon\dot{\theta}^2\sin\theta, \tag{68}$$

$$I\ddot{\theta} = T_a + \varepsilon k_1(y\cos\theta - x\sin\theta) + \left|\widetilde{\boldsymbol{N}}\ {}_{\boldsymbol{C}}\boldsymbol{R}_{\boldsymbol{D}}\right| + \left|\widetilde{\boldsymbol{F}}_{\mathbf{f}}\ {}_{\boldsymbol{C}}\boldsymbol{R}_{\boldsymbol{D}}\right|. \tag{69}$$

## 2.8. The bearing with pins

One often designs a safety bearing with different geometries to restrain high vibrations. Moreover, the use of active pins modifies the internal geometry when needed. In this case, no special or complex geometry is required. First, some considerations must be made regarding the pin modeling.

A pin is like a small one-dimensional bar, and it deforms only along its length, *i.e.*, it does not suffer the effects of buckling or lateral deformation. It is considered a massless object and can resist fatigue and strong impacts. Its stiffness can be estimated by the expression found in every solid mechanics book in engineering (Gere, 2003).

$$K_p = \frac{E_p A_p}{L_p}. \tag{70}$$

While the Young elastic constant $E_p$ is characteristic to the material chosen to build the pin and the area $A_p$ is its cross section. The length $L_p$ of the pin is critical parameter and has to have a minimum value. The idea is that the pin is a retractile device which minimizes the gap and avoids impacts or high amplitudes.

The question is: how long they should go and how many pins are needed? Whether there are too few pins, or whether they are too short it is possible that the disc hits the wall or whether they are too long that they choke the rotor and it loses its ability to rotate.

An idealized concept to prevent any impact on the bearing structure is to leave the exact free space for the rotor to move without the possibility of hitting the wall. Figure 2-14 illustrates this condition.

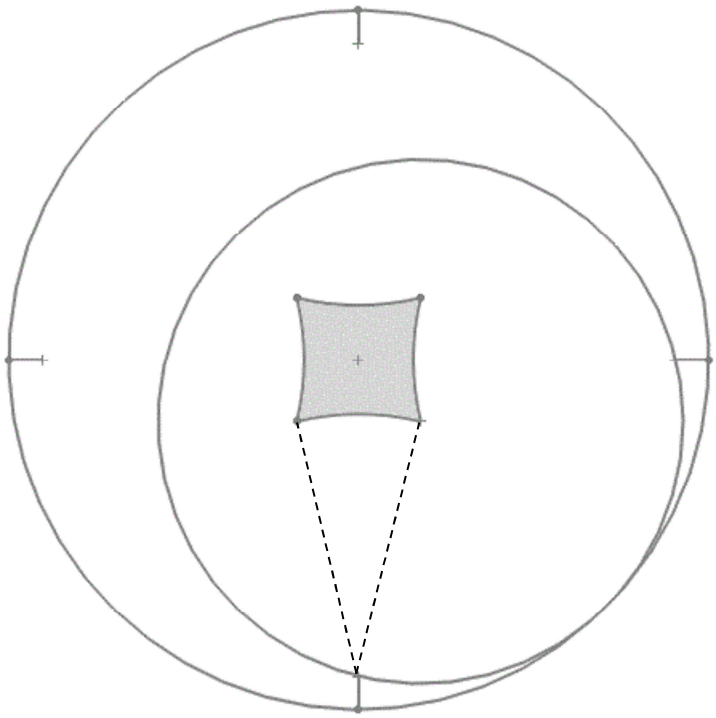

**Figure 2-14**: The configuration of the pins inside the bearing and the free area.

The shadowed area inside the image above is the space where the rotor is able to move. Its corners are the only points where the rotor really hits the structure of the bearing. Anything longer than this minimum length, $L_p$, will prevent the bearing from being hit by the rotor. The geometry of the free area is perimeter of the rotor center motion as it rolls on the edge of the pins until it hits the next pin and the bearing wall in just one point. Clearly, the minimum length $L_p$ is a geometric ratio of the radii of the disc $R_d$ and of the bearing $R_b$. It is easily calculated as the roots of a second order equation,

$$L_p > R_b - \sqrt{2R_d^2}. \tag{71}$$

## 2.9. The contact state with pins

When one considers the impacts now on the pins, but not on the bearing wall, the equations (67), (68) and (69) change a little bit because the direction of the normal force and likewise the friction force change. The normal force still points to the center of the disc. Its magnitude is calculated as how much the rotor's disc compresses the pin, *i.e.*, how much the disc edge deforms the pin. Mathematically, the contact happens when the distance from the disc center to the top of the pin is smaller than the size of the radius of the disc:

$$|\boldsymbol{\delta}_i| \equiv |\text{position vector of pin}_i - \boldsymbol{B}| = \begin{cases} |{}_P\boldsymbol{r}_B| \leq R_d \rightarrow \text{impact,} \\ |{}_P\boldsymbol{r}_B| > R_d \rightarrow \text{no impact.} \end{cases} \tag{72}$$

$\boldsymbol{\delta_i}$ is a vector pointing from the top of the $i^{\text{th}}$ pin to the disc edge and $\boldsymbol{B}$ is a vector pointing from the origin to the disc center, see Figure 2-5. This is an arbitrary convention which implies the sign on the impact formulation to be written below. The angle $\alpha$, defined in the previous section, is of no use for the impact calculus; instead, the angle of incidence $\beta$ on the impact in a local reference frame, see Figure 2-15.

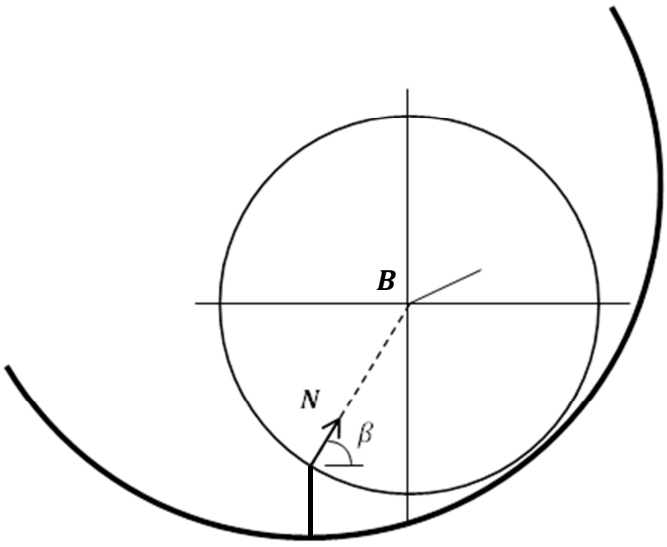


**Figure 2-15**: Angle of impact $\beta$ and the impact force $N$ pointing the rotor's center.

Thus, the vector $\boldsymbol{\delta}$ has the components

$$\boldsymbol{\delta} = \begin{pmatrix} \delta_x \\ \delta_y \\ 0 \end{pmatrix} = \begin{pmatrix} |\boldsymbol{\delta}| \cos\beta \\ |\boldsymbol{\delta}| \sin\beta \\ 0 \end{pmatrix}. \tag{73}$$

Then the normal force is an elastic response of the pin to the deformation and is written as

$$\boldsymbol{N} = -K_p \boldsymbol{\delta} = -K_p \begin{pmatrix} \delta_x \\ \delta_y \\ 0 \end{pmatrix} = -K_p \begin{pmatrix} |\boldsymbol{\delta}| \cos\beta \\ |\boldsymbol{\delta}| \sin\beta \\ 0 \end{pmatrix}. \tag{74}$$

Therefore, the friction force has the same formulation of equation (66) and is orthogonal with respect to the normal force. Since the center of mass is dislocated from the center of the disc, there is a torque applied from the normal force besides the torque of the friction force. The parameter $\boldsymbol{d}$ in Figure 2-16 is the distance

between the disc center to the top of the pin. Lastly, the contact state condition with pins, eq. (74) is inserted into equations (6), (7) and (8), putting $c_1 = 0$:

$$m\ddot{x} + k_1 x = m\varepsilon\dot{\theta}^2 \cos\theta + m\varepsilon\ddot{\theta} \sin\theta - K_p\delta_x + K_p\delta_y\mu \operatorname{sign}(\mathbf{V}_{\text{edge}}) \quad (75)$$

$$m\ddot{y} + k_1 y = m\varepsilon\dot{\theta}^2 \sin\theta - m\varepsilon\ddot{\theta} \cos\theta - K_p\delta_y - K_p\delta_y\mu \operatorname{sign}(\mathbf{V}_{\text{edge}}) \quad (76)$$

$$I\ddot{\theta} = T_a + k_1\varepsilon(\cos\theta\, y - \sin\theta\, x) + \left|\widetilde{\boldsymbol{d}}\boldsymbol{N}\right| + \left|\widetilde{\boldsymbol{d}}\boldsymbol{F}_{\text{f}}\right|\operatorname{sign}\left(\boldsymbol{V}_{\text{edge}}\right). \quad (77)$$

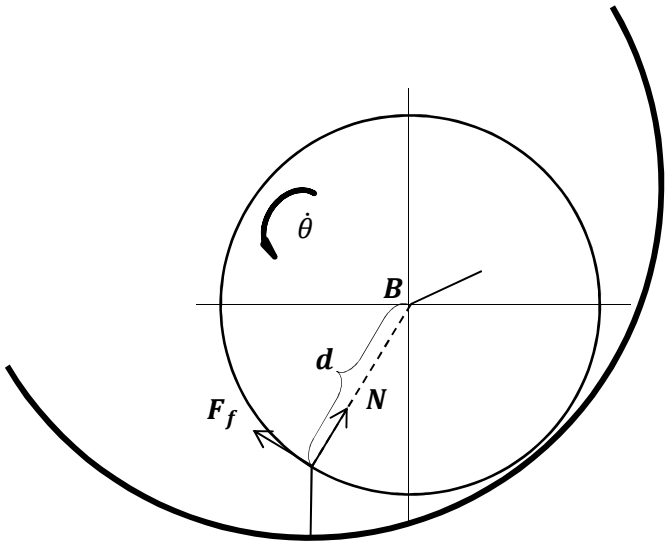


**Figure 2-16**: Explanation of vector $d$ when disc is impacting.

## 2.10. Dimensionless equations

Chapter 3 will present a mathematical program containing all developments made in the previous sections in order to simulate the impacts on the disc and on the pins. It is convenient to write the equations as dimensionless ones, because it helps the visualization of the relationship between the parameters, saves computational time and increases numerical precision since values are also normalized. The first

rule to write them in the non-dimensional form is to introduce a non-dimensional time $\tau$ as

$$\tau = \omega t, \tag{78}$$

where $\omega$ is the non-damped eigenfrequency (10). The time derivatives in all equations must obey the chain rule of derivation;

$$\frac{d}{dt} = \frac{d}{d\tau}\frac{d\tau}{dt} = \omega\frac{d}{d\tau} \tag{79}$$

$$\frac{d^2}{dt^2} = \left(\frac{d\tau}{d\tau}\right)^2 \frac{d^2}{d\tau^2} + \underbrace{\frac{d^2\tau}{dt^2}}_{=0}\frac{d}{d\tau} = \omega^2\frac{d^2}{d\tau^2}. \tag{80}$$

In order to generalize the coordinates $x$ and $y$, both must be divided by a common parameter of the same dimension of length. The unbalance parameter $\varepsilon$ is such an appropriate constant, so we may define

$$X = \frac{x}{\varepsilon};\ Y = \frac{y}{\varepsilon}. \tag{81}$$

Without contact on the disc surface, equations (6), (7) and (8) can be rewritten taking into account equations (78), (79), (80) and (81). For this formulation damping is not considered. We obtain

$$X'' + X = \theta'^2\cos\theta + \theta''\sin\theta, \tag{82}$$

$$Y'' + Y = \theta'^2\sin\theta + \theta''\cos\theta, \tag{83}$$

$$\theta'' = \frac{T_a}{\frac{1}{2}m{R_d}^2\omega^2} + \left(\frac{\varepsilon}{R_d}\right)^2(\cos\theta\, Y - \sin\theta\, X). \tag{84}$$

The same is done with the contact state equations (75), (76) and (77), which represent the dynamical analysis of impacts occurring on the pins,

$$X'' + X = \theta'^2 \cos\theta + \theta'' \sin\theta - \left(\frac{\omega_p}{\omega}\right)^2 \left(\frac{\delta_x}{\varepsilon}\right) + \left(\frac{\omega_p}{\omega}\right)^2 \left(\frac{\delta_y}{\varepsilon}\right) \mu \text{ sign } (\mathrm{V_t}) \tag{85}$$

$$Y'' + Y = \theta'^2 \sin\theta - \theta'' \cos\theta - \left(\frac{\omega_p}{\omega}\right)^2 \left(\frac{\delta_y}{\varepsilon}\right) - \left(\frac{\omega_p}{\omega}\right)^2 \left(\frac{\delta_x}{\varepsilon}\right) \mu \text{ sign } (\mathrm{V_t}) \tag{86}$$

$$\theta'' = \bar{T}_a + \left(\frac{\varepsilon}{R_d}\right)^2 (\cos\theta\, Y - \sin\theta\, X) + \left(\frac{\omega_p}{\omega}\right)^2 \left(\frac{2}{R_d^2}\right) |\tilde{\boldsymbol{d}}\boldsymbol{\delta}| \left(1 + \mu \text{sign}(\mathrm{V_t})\right), \tag{87}$$

where

$$\omega_p = \sqrt{\frac{K_p}{m}} \quad \text{and} \quad \bar{T}_a = \frac{T_a}{\frac{1}{2} m {R_d}^2 \omega^2}.$$

One can notice that there is a relationship between the frequencies involved in the equations above. By varying the coefficients of elasticity it is possible to perform a more profound analysis in the case of nonlinear fields.

# 3
# The numerical simulation

As part of the whole analysis of this work, the simulation plays an important role. It certifies before going to practice if an idea can actually work. Then, once it produces adequate results, the parameters can be adjusted to perform different situations.

The implemented model is that of a simple rotor inside a greater circular radius representing the retainer bearing. We consider a stiffness force coming from the shaft, which pushes back the rotor center as it moves sideways inside the bearing. In the last section of the previous chapter, the dynamical equations of motion are written in the non-dimensional form. Two main situations may occur; either the rotor is in the non-contact state or in the impacting one. Thus, the simulation program must have a rule that alternates accordingly the modeling the state space equations.

On circular bearings this rule is quite simple. The gap, or difference between the radii, indicates whether the rotor is impacting or not. It gets much more difficult when the pins are considered and the internal geometry changes. So the gap is larger or shorter in different places inside the bearing.

## 3.1.
## State space equations

As said before, the dimensionless equations are better for simulation because they require less memory from the computer and prevent numerical errors due to the normalized matrix components.

A state space of variables is chosen in the following order:

$$\boldsymbol{\psi} = \begin{bmatrix} X \\ Y \\ \theta \end{bmatrix}, \tag{88}$$

$$\boldsymbol{q} = \begin{pmatrix} \boldsymbol{\psi} \\ \boldsymbol{\psi}' \end{pmatrix} = \begin{bmatrix} X \\ Y \\ \theta \\ X' \\ Y' \\ \theta' \end{bmatrix}. \tag{89}$$

Equations (81), (83) and (84) of the non-contact state and eqs. (85), (86) and (87) can be rewritten again with the underline symbol, which denotes a matrix:

$$\underline{\boldsymbol{M}}\boldsymbol{\psi}'' + \underline{\boldsymbol{C}}\boldsymbol{\psi}' + \underline{\boldsymbol{K}}\boldsymbol{\psi} = \boldsymbol{F}. \tag{90}$$

Then

$$\boldsymbol{\psi}'' = \underline{\boldsymbol{M}}^{-1}\left(\boldsymbol{F} - \underline{\boldsymbol{C}}\boldsymbol{\psi}' - \underline{\boldsymbol{K}}\boldsymbol{\psi}\right). \tag{91}$$

They are written on the dimensionless form as:

$$\underline{\boldsymbol{M}} = \begin{bmatrix} 1 & 0 & -\sin\theta \\ 0 & 1 & \cos\theta \\ 0 & 0 & 1 \end{bmatrix}, \quad \underline{\boldsymbol{C}} = \begin{bmatrix} 2\xi & 0 & -\theta'\cos\theta \\ 0 & 2\xi & -\theta'\sin\theta \\ 0 & 0 & 0 \end{bmatrix}, \quad \underline{\boldsymbol{K}} = \begin{bmatrix} 1 & 0 & 0 \\ 0 & 1 & 0 \\ 0 & 0 & 0 \end{bmatrix},$$

$$\underline{\boldsymbol{M}}^{-1}\boldsymbol{F} = \begin{bmatrix} 0 \\ 0 \\ \bar{T}_a + \left(\dfrac{\varepsilon}{R_d}\right)^2 (\mathrm{Y}\cos\theta - X\sin\theta) \end{bmatrix}. \tag{92}$$

The same is done to the equation that corresponds to the impact state. The only change is in the force vector $\underline{\boldsymbol{M}}^{-1}\boldsymbol{F}$, which reads

$$\underline{\boldsymbol{M}}^{-1}\boldsymbol{F} = \begin{bmatrix} \left(F_{\mathrm{f}}^{x} + F_{\mathrm{imp}}^{x}\right) \\ \left(F_{\mathrm{f}}^{y} + F_{\mathrm{imp}}^{y}\right) \\ \bar{T}_a + \left(\dfrac{\varepsilon}{R_d}\right)^2 (Y\cos\theta - X\sin\theta) + \left(\dfrac{\omega_p}{\omega}\right)^2 \left(\dfrac{2}{R_d^2}\right) |\tilde{\boldsymbol{d}}\boldsymbol{\delta}| \left(1 + \mu \mathrm{sign}(\mathrm{V_t})\right) \end{bmatrix}. \tag{93}$$

We are now able to write the following dimensionless form of the system in terms of the state space variables

$$\boldsymbol{q}' = \begin{pmatrix} \underline{\mathbf{0}} & \underline{\boldsymbol{I}} \\ \underline{\boldsymbol{M}}^{-1}(-\underline{\boldsymbol{K}}) & \underline{\boldsymbol{M}}^{-1}(-\underline{\boldsymbol{C}}) \end{pmatrix} \boldsymbol{q} + \underline{\boldsymbol{M}}^{-1}\boldsymbol{F}, \tag{94}$$

where $\underline{\boldsymbol{I}}$ denotes the $3 \times 3$ identity matrix.

## 3.2. The Runge-Kutta method

Since we are facing non-linear equations even when there are no impacts, a numerical method must be taken account to solve and simulate the whole behavior through time. The Runge-Kutta method is a highly accurate technique of solving numerically differential equations. It was developed early 20th century by the German mathematicians Carl D. Runge and Martin W. Kutta. The most common form of the Runge-Kutta method is widely known as the Runge-Kutta of 4th order. It is the weighted average of four functions beginning with an initial value state. By defining a step size $\Delta t$ and $\boldsymbol{q}_0$ the initial state vector or

$$\dot{\boldsymbol{q}} = f(t, \boldsymbol{q}), \qquad \boldsymbol{q}(t_0) = \boldsymbol{q}_0$$

The next state is

$$\boldsymbol{q}_{n+1} = \boldsymbol{q}_n + \frac{1}{6}(\boldsymbol{K1} + 2\boldsymbol{K2} + 2\boldsymbol{K3} + \boldsymbol{K4}) \text{ and } t_{n+1} = t_n + \Delta t, \qquad n = 1, 2, 3, \ldots$$

where the coefficients $\boldsymbol{K1}$, $\boldsymbol{K2}$, $\boldsymbol{K3}$ and $\boldsymbol{K4}$ are functions to increment the actual state to the next one.

$$\boldsymbol{K1} = \Delta t f(t_n, \boldsymbol{q}_n), \tag{95}$$

$$\boldsymbol{K2} = \Delta t f\left(t_n + {}^{\Delta t}/_{2}, \boldsymbol{q}_n + {}^{\boldsymbol{K1}}/_{2}\right), \tag{96}$$

$$\boldsymbol{K3} = \Delta t f\left(t_n + {}^{\Delta t}/_{2}, \boldsymbol{q}_n + {}^{\boldsymbol{K2}}/_{2}\right), \tag{97}$$

$$\boldsymbol{K4} = \Delta t f(t_n + \Delta t, \boldsymbol{q}_n + \boldsymbol{K3}). \tag{98}$$

If one analyzes the coefficient of $\boldsymbol{K1}$, it is the Euler's method of solving numerical equations. It means that the next value, $\boldsymbol{q}_{n+1}$, is the derivative of the function applied to the next step $\boldsymbol{\Delta t}$ added to current $\boldsymbol{q}$. But, after some iteration, the Euler's methods deviate too much from the actual function. The Runge-Kutta improves it by adding a weighted average with the values at the middle point of the increment.

Next, the chosen software to perform the simulation and to solve the numerical equation is the Matlab®. It has already implemented a Runge-Kutta Algorithm *ode45* to solve equations numerically. In Figure 3-1, we can see graphically the difference between the Euler's method and the Runge-Kutta of an ordinary function $f(x)$.

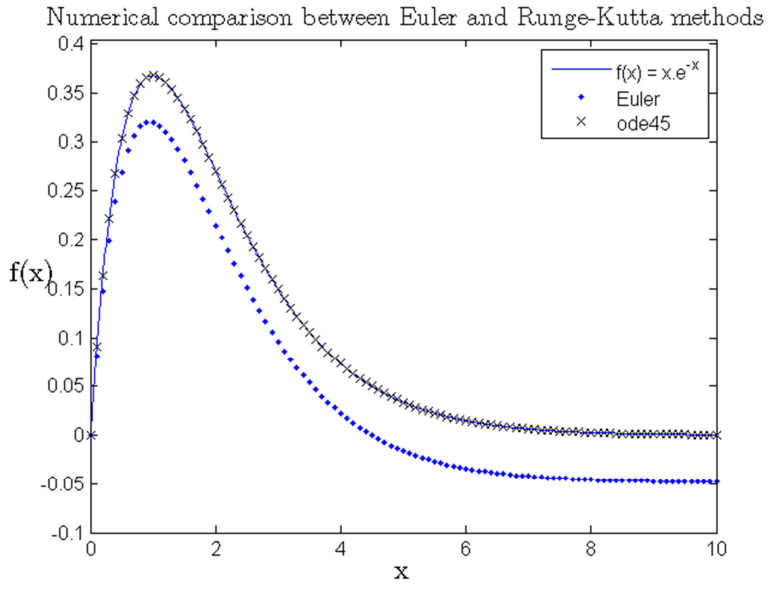


**Figure 3-1**: Comparison between the numerical method of an ordinary function.

Thus, due to the high precision and accuracy the *ode45* from Matlab® is the best choice for numerical analysis.

## 3.3. Simulation cases

The conducted studies were completely designed with the Matlab® software. It is a powerful tool full of embedded mathematical functions. There are two main cases, the first without pins and the second with pins. They show different situations and initial conditions. Regarding the simulation with pins, it has more boundaries conditions and limitations. All of them have the same parameters for disc and dimensions to ensure a good comparison. The simulation parameters are given on the Appendix A.

### 3.3.1. A disc without a shaft

As a matter of comparison with further experiments a disc without a shaft is an interesting case of study of how the friction force in the contact process acts on a metallic disc with unbalance. First a disc without rotational speed, but with an initial translational velocity of its center, floating on an air cushion, is simulated. The results of the hits are in Figure 3-2.

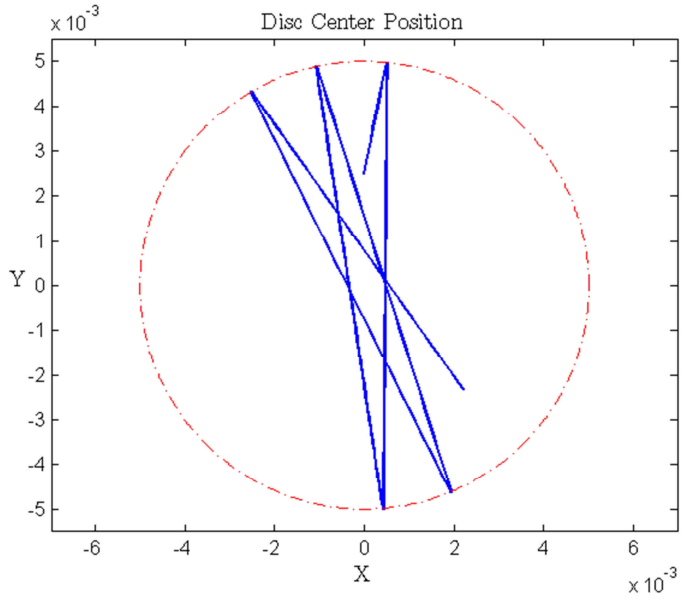


**Figure 3-2**: Series of hits of a shaftless rotor. Rotor does not rotate.

Then a second and a third case are shown when the rotor has a small angular velocity $\Omega = 1\text{Hz}$ or $\Omega = 2\text{Hz}$. Elastic impacts are considered here.

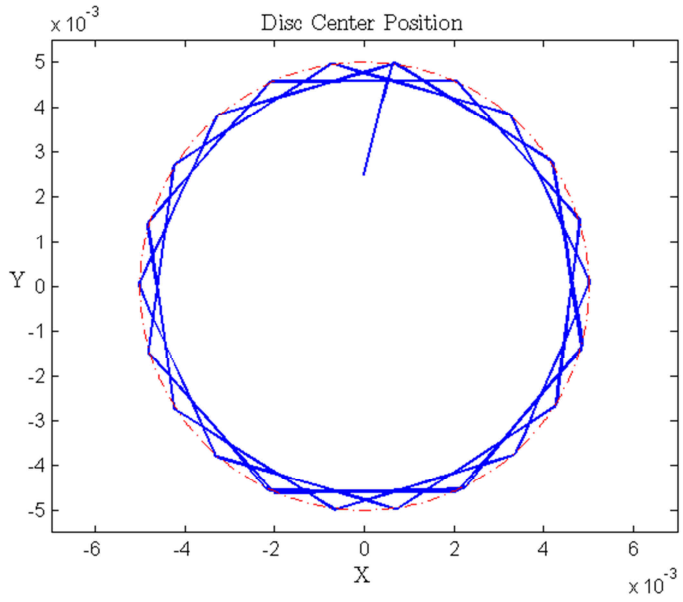


**Figure 3-3**: Whirl of the shaftless rotor on the bearing wall (1Hz).



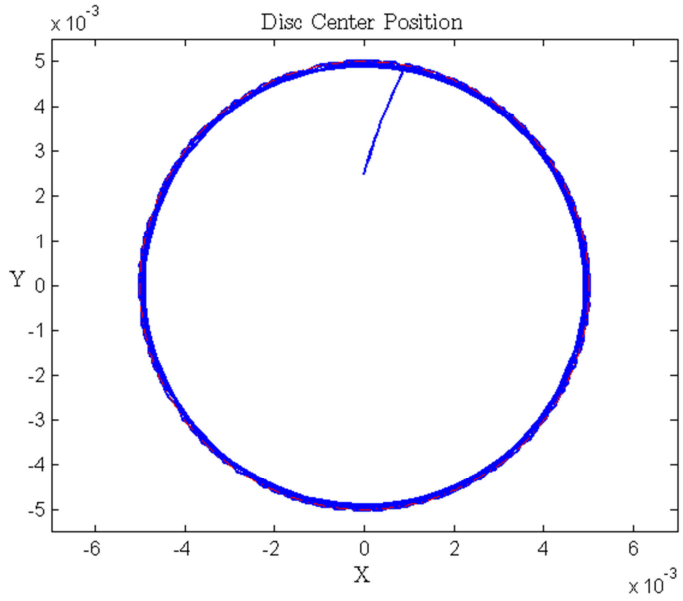


**Figure 3-4**: Whirl of the shaftless rotor on the bearing wall (2Hz).

### 3.3.2.
### Disc with shaft, simulations without pins

The first simulations show when the disc has an initial angular velocity and also some velocity of its center starting from origin. Then due to the imbalance the eccentric and transient motion appears. When there is no damping the motion orbits around the center of the bearing. The next figures Figure 3-5, Figure 3-6 and Figure 3-7 show the motion of 1Hz, 2Hz and 4Hz. Then on the following figures Figure 3-7, Figure 3-8 and Figure 3-9, the disc is accelerated by the minimum torque possible (30). The initial conditions set are all the same:

$$\boldsymbol{q_0} = [\,0\mathrm{m} \quad 0\mathrm{m} \quad 0\mathrm{rad} \quad 0.001\,{}^{\mathrm{m}}/_{\mathrm{s}} \quad 0.005\,{}^{\mathrm{m}}/_{\mathrm{s}} \quad 2\pi.\,\mathrm{Hz}]^T$$

or dimensionless written with $\omega = 14.0\,{}^{\mathrm{rad}}/_{\mathrm{s}}$

$$\boldsymbol{q_0} = \left[0 \quad 0 \quad 0 \quad 0.159 \quad 0.795 \quad {}^{2\pi.\,\mathrm{Hz}}/_{\omega}\right]^T.$$

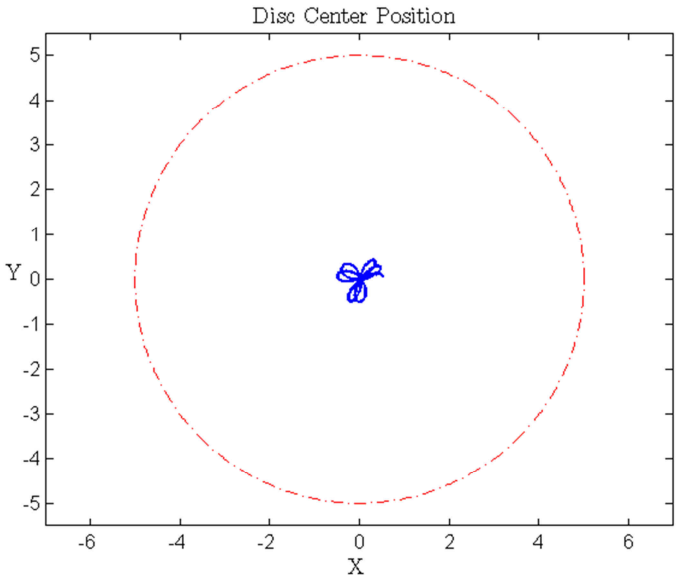


**Figure 3-5**: Movement of the disc center position inside the gap when rotating at 1Hz. The dashed red line is boundary without hitting the wall.

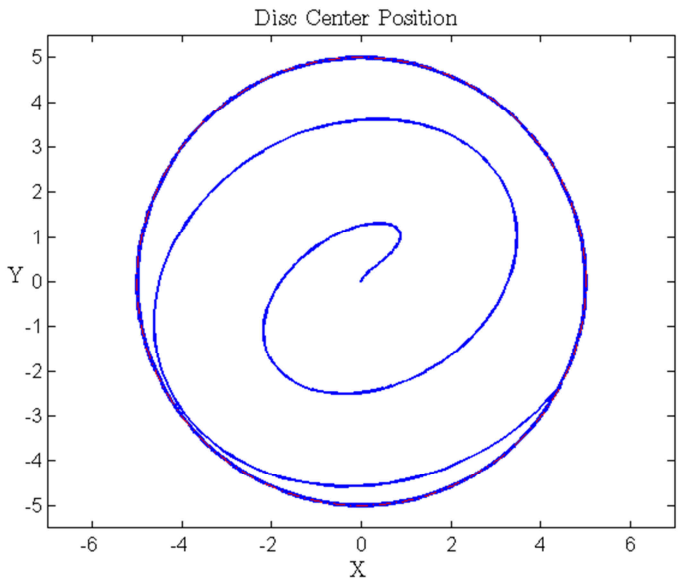


**Figure 3-6**: Same as Figure 3 4, but the disc is rotating 2Hz and starts hitting the wall.

In Figure 3-6 the disc moves near the resonance velocity of 2.22Hz and therefore its trajectory is a spiral and hits the wall once, bounces and then starts to move against the its own circular movement.

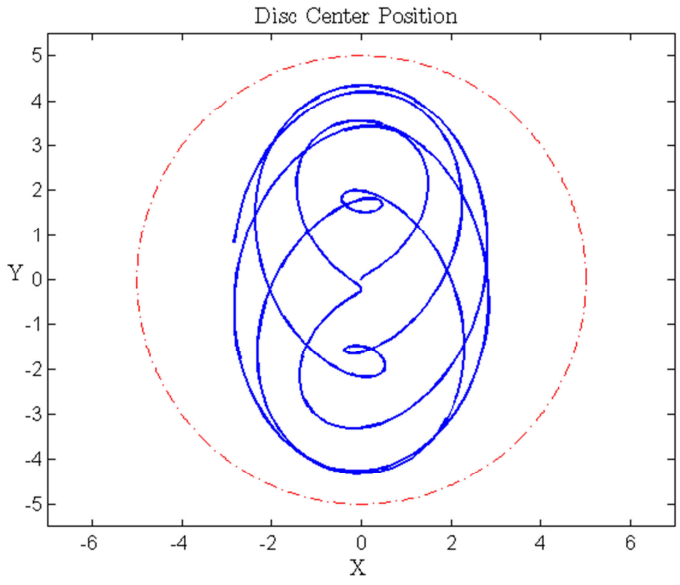


**Figure 3-7**: The orbit of the disc above the resonance rotation, 4Hz. No hits happen.

The friction force coefficient is according to (Kent, 1950) steel on steel dry.

$$\mu_{steel/steel} = 0.56.$$

So it is supposed that the disc does not slide on the wall.

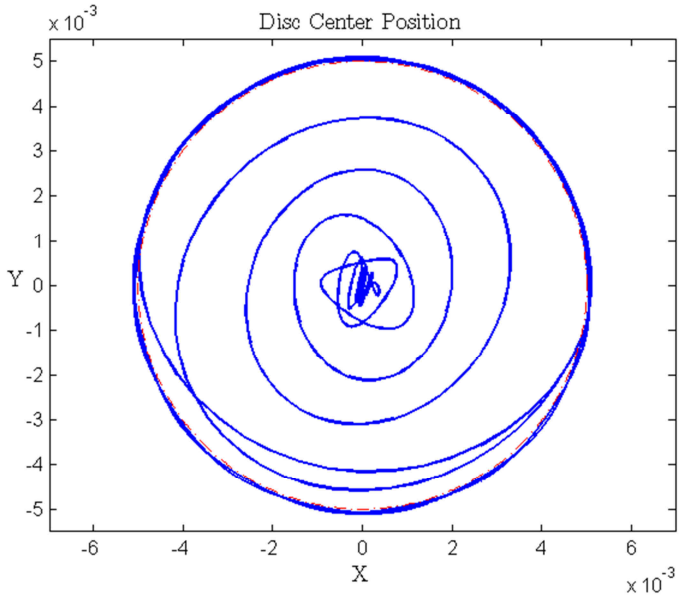


**Figure 3-8**: Movement of disc center when the minimum torque is applied to the dynamical system.

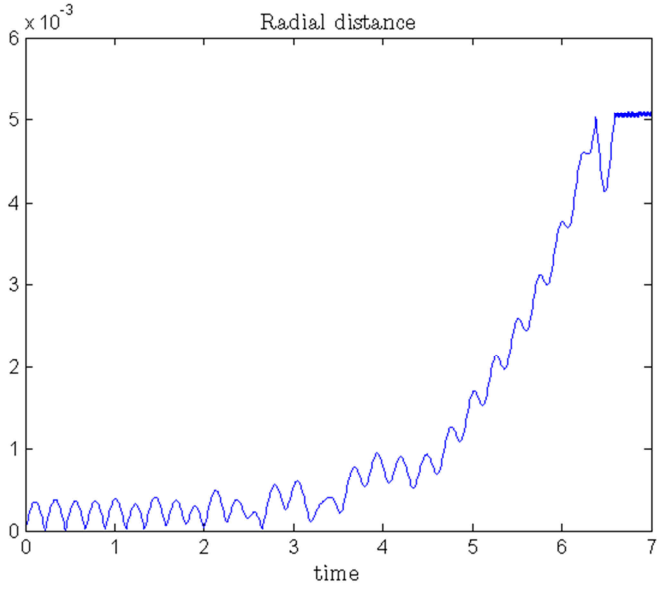


**Figure 3-9**: Radial distance of the disc center from origin in the middle of the bearing.

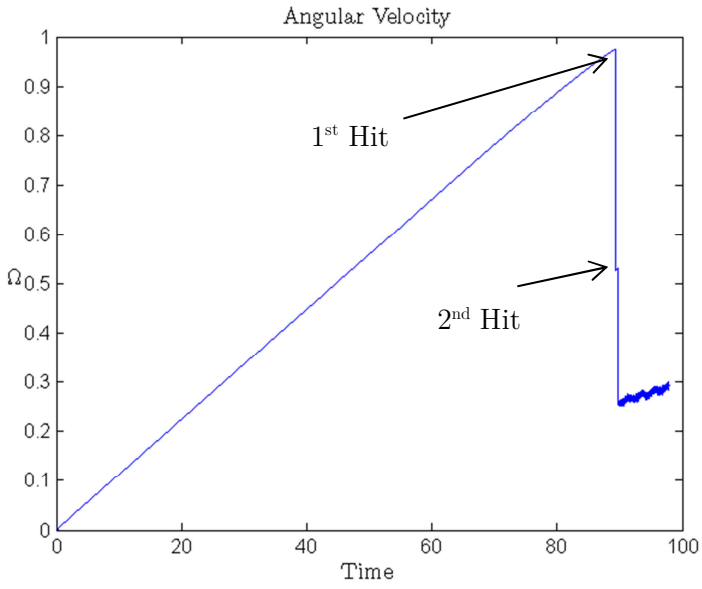


**Figure 3-10**: The rising angular speed by applying the minimum torque. Its two sudden decreases are shown when two close impacts occur. On the second impact it starts to roll.

Now, by changing the initial condition to

$$\boldsymbol{q_0} = \left[0\text{m} \quad 0.95r_0\text{m} \quad 0\text{rad} \quad 0.075\,{}^{\text{m}}/_{\text{s}} \quad 0\,{}^{\text{m}}/_{\text{s}} \quad 0\,{}^{\text{rad}}/_{\text{s}}\right]^T$$

So the disc is starting from an offset that almost touches the bearing's wall and also has an initial horizontal velocity. Neither there is an initial rotation velocity nor is a torque inserted into the system. The results of this case are shown on Figure 3-11.

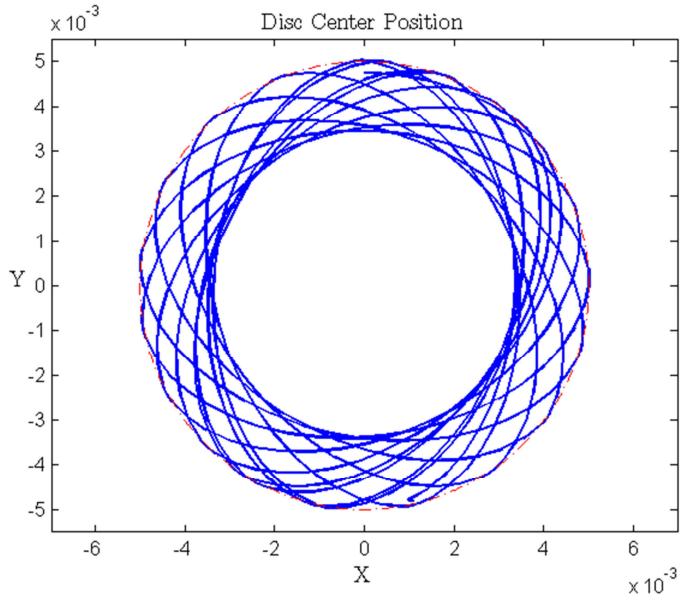


**Figure 3-11**: Series of hits when there is a bump and an offset as initial condition.



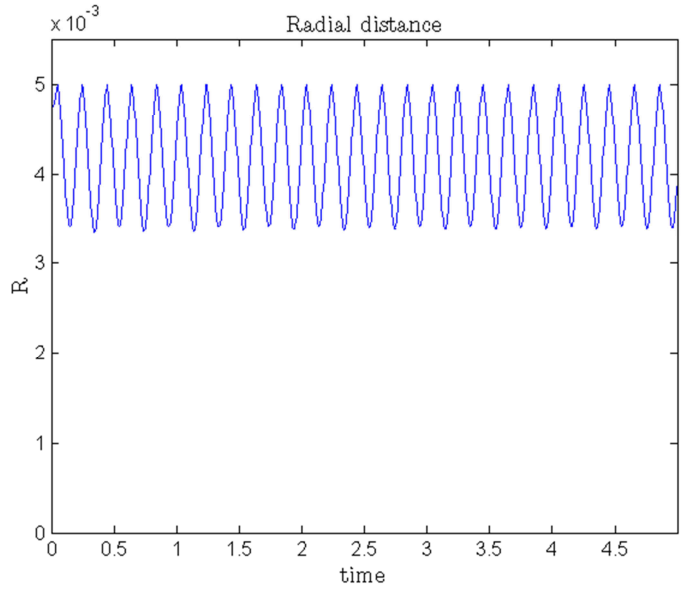


**Figure 3-12**: Oscillation of the disc's center from origin.

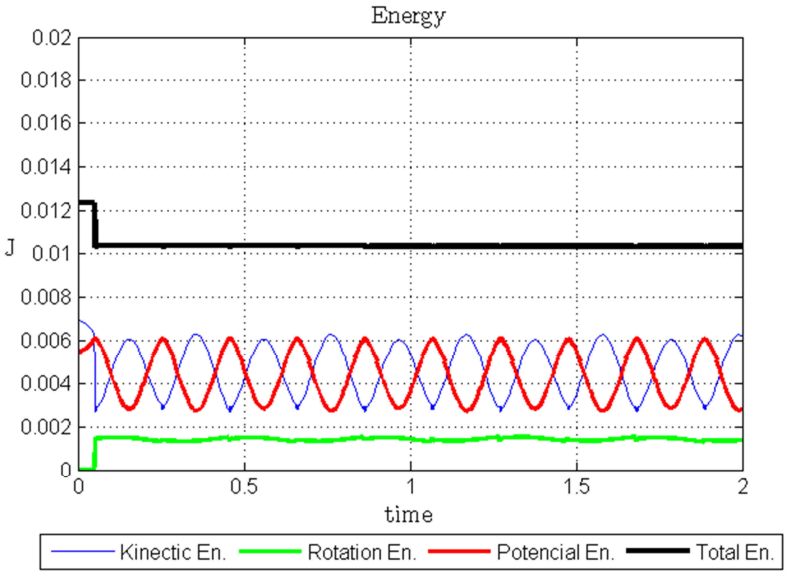


**Figure 3-13**: Variation of energy through from 0 to 2 seconds.



After the first impact the disc gets a slower speed, the next impacts now have a friction force against it, inducing a whirl on the wall. Since there is this no external damping, the total energy only decreases after each impact, see a more detailed plot in Figure 3-14.

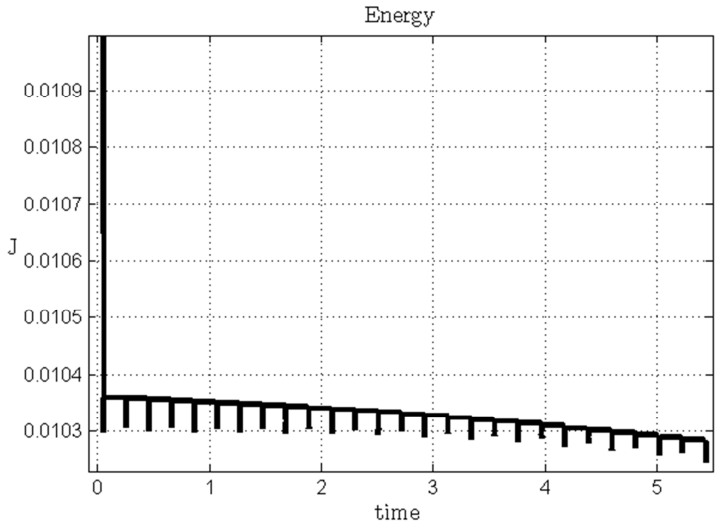


**Figure 3-14**: Close up showing the decrease of total energy after each impact.

A third simulation was conducted in order to demonstrate the backward whirl effect. Thus, once again, we changed the initial condition to the following condition:

$$\boldsymbol{q_0} = \left[0\text{m} \quad 0.9r_0\text{m} \quad 0\text{rad} \quad -0.1\,{}^{\text{m}}/_{\text{s}} \quad 0\,{}^{\text{m}}/_{\text{s}} \quad 2\pi 3.2\,{}^{\text{rad}}/_{\text{s}}\right]^T.$$

The results are shown in the next figure, Figure 3-15 and Figure 3-16.

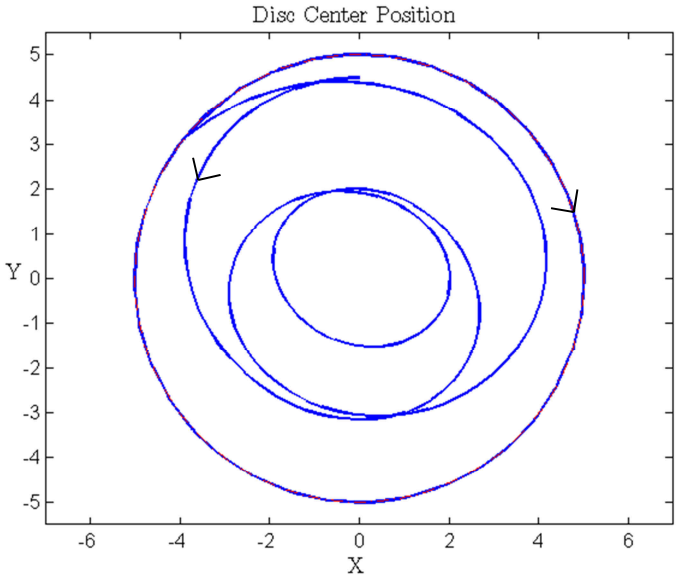


**Figure 3-15**: Backward whirl orbits at $r_0$ described in simulation.

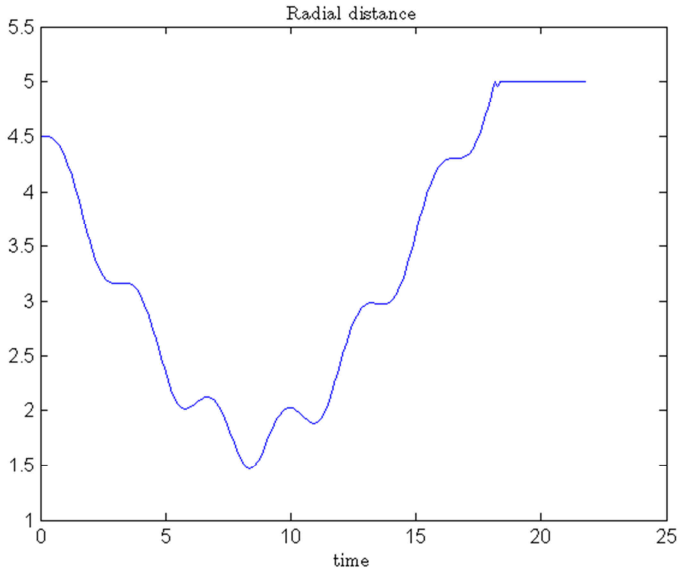


**Figure 3-16**: Radial distance from the origin and the disc center.

As it can be seen, the disc is rotating with angular velocity of 3.2Hz, and at the moment it hit the wall and friction starts to rub on the wall. This is the behavior we intent to avoid in the next section by adding the pins in the simulation and in the practical part in the next chapter.

### 3.3.3. Simulation with pins

The insertion of the pins on the simulation leads to a more complex boundary condition. At every step it is computed the distance of the edge of the disc to each pin inside and evaluates the necessary state-space of the dynamical analysis. Three situations are possible of happen. The non-collision state, the collision on a single pin, collision on two pins, and at last but highly improbable a hit on the wall. This last condition can exist because of the elastic modeling of the pins, if the disc penetrates deep inside the pin it could be possibly reach the bearing's wall. In order to prevent that the pin have a 10% larger length as defined from equation (71).

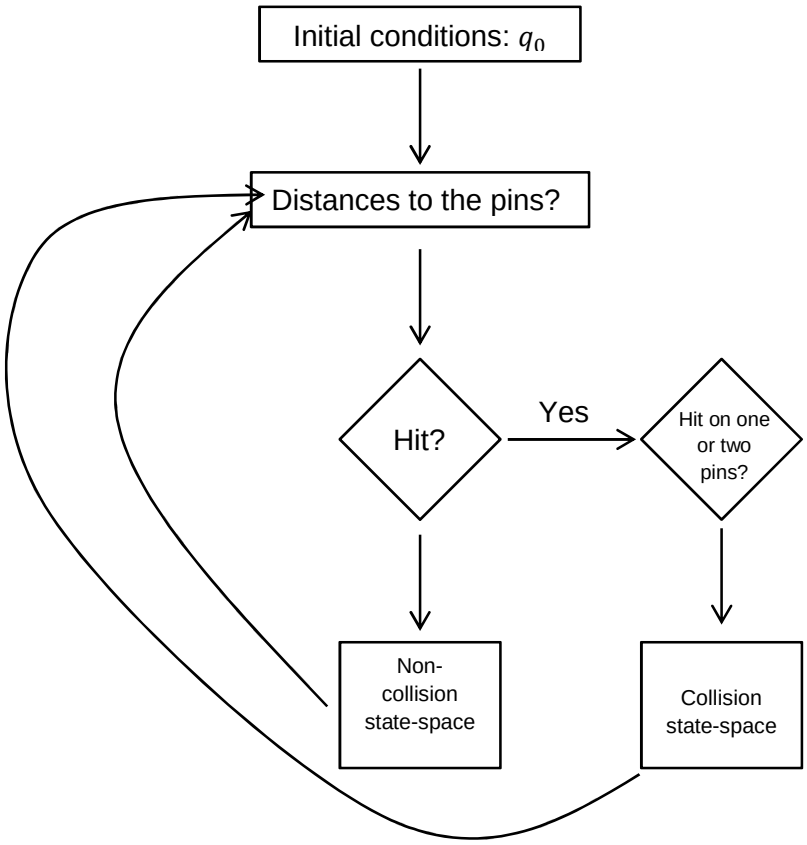


**Figure 3-17**: The flowchart of the simulation.

In this case the equations of motion implemented are the dimensionless from section 2.10, because it saves simulation time and guaranties convergence of the numerical solution by avoiding stiff matrices. However, it is not possible to simulate a shaftless rotor because of the chosen non-dimensional time rule (78), which depends of resonance and therefore the shaft elastic coefficient $k_1$. Another consideration is that the pins have a 10% larger than the minimum length from equation (71). This reduces the chances that the disc edge will hit the bearing wall. As there are only non-dimensional lengths in this case, the radii and the length of the pin should be adjusted too.

$$R_d^* = {R_d}/{\varepsilon},$$
$$R_b^* = {R_b}/{\varepsilon},$$
$$L_p^* = {L_p}/{\varepsilon}.$$

The first simulated case is a rotor which is already spinning from the beginning at a nominal velocity equal to the resonance velocity. It starts from the origin and because it is in the critical speed it moves on a spiral, like in previously cases. Now, before it hits the bearing wall, it reaches the pins, which *push* it back away from the wall. The disc begins to loose rotational energy after each impact. Figure 3-18 to Figure 3-22 illustrate the simulated behavior.

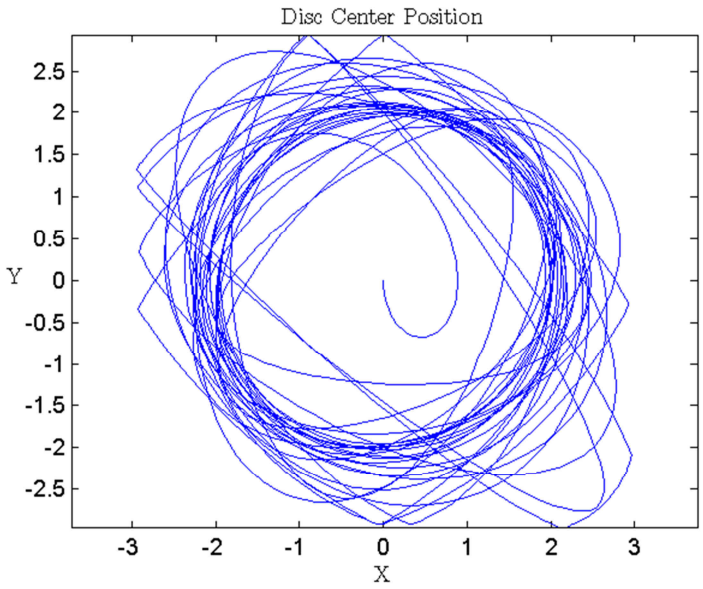


**Figure 3-18**: The disc center position being released from origin at the resonance speed.

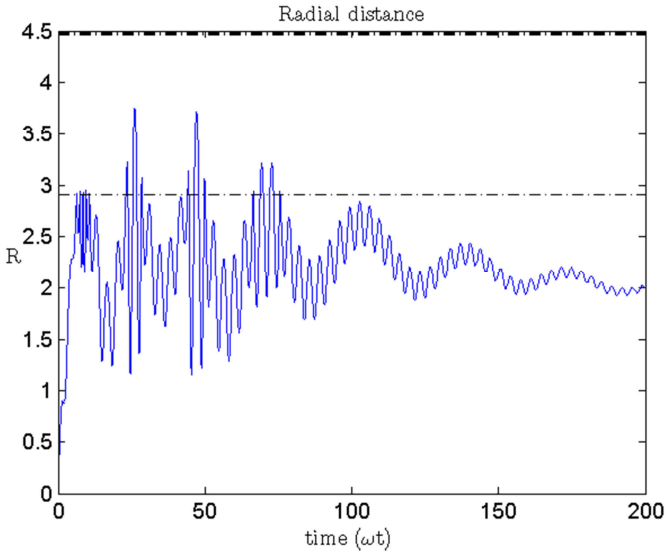


**Figure 3-19**: The radial distance $r$, its maximum value stays far away from the gap (top bold dashed line).

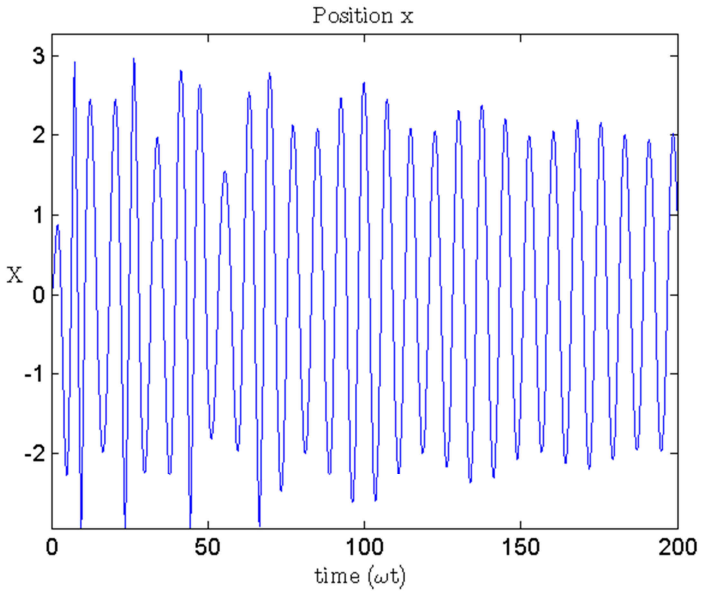


**Figure 3-20**: Oscillation of the X position through time.



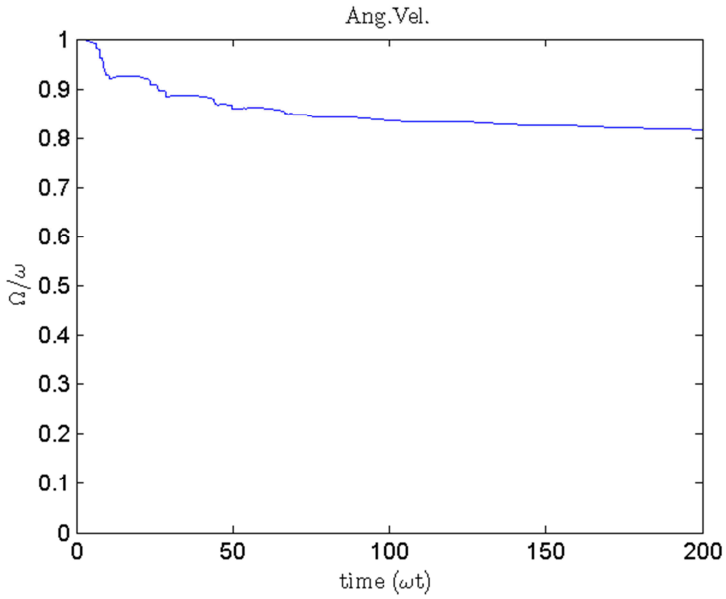


**Figure 3-21**: Angular velocity decreases after each impact.

In Figure 3-19, presents two dashed lines, the thin one represents the minimum distance allowed to hit the pins, the bold line is the maximum allowed displacement that the disc may move from the origin. It represents a hit on the wall; it is a situation we want to avoid. Observing these figures, there were no hits

on the wall. Figure 3-21, is the variation of angular velocity in time, after each impacts it is seems like small portions of rotational energy is withdrawn from the disc.

Figure 3-22 illustrates how the constrained free area looks like. The free area of motion is reduced by the pins.

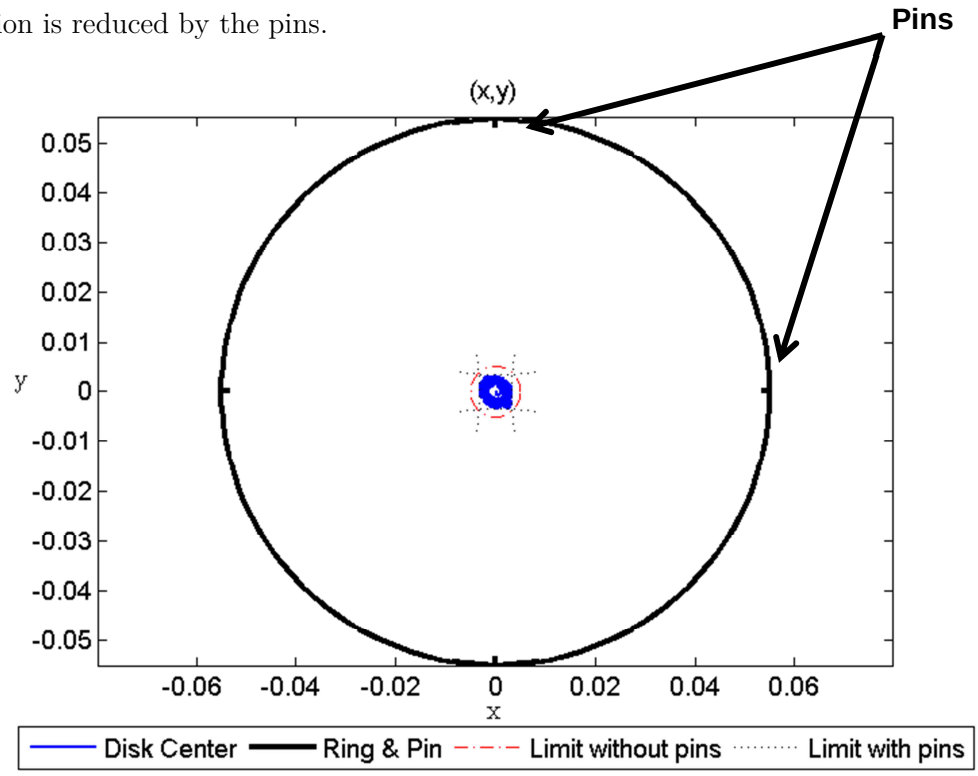


**Figure 3-22**: Larger view from the bearing with the four pins. The blue line is the constrained movement of the disc center. This figure is dimensionally corrected.

A second case was simulated with a slight different initial condition. The disc starts from the rest at the origin, but a constant torque is applied to the system equations. Its value is the minimum torque, defined by (Markert, Pfützner, & Gasch, 1980) from equation (30). The disc begins to rotate and rapidly reaches the resonance angular velocity. Then a spiral movement and high lateral vibrations take place, soon the rotor begins to hit every pin in a regular shape, Figure 3-23, although it is unable to surpass any higher speeds than 20% from the resonance velocity, because at every hit a portion of angular velocity is taken from the rotor

and as soon as it regained it a new hit happens, which removes it again, see Figure 3-25.

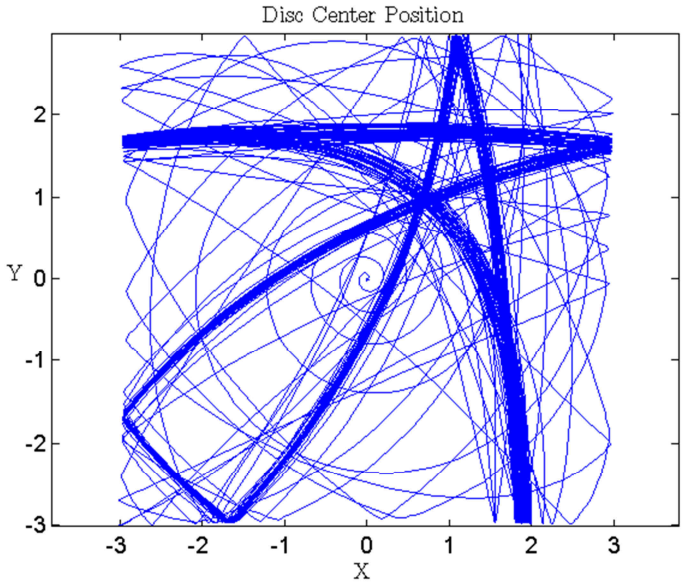


**Figure 3-23**: Disc center position trajectory. It does not hit the wall, but repeatedly hits the pins.

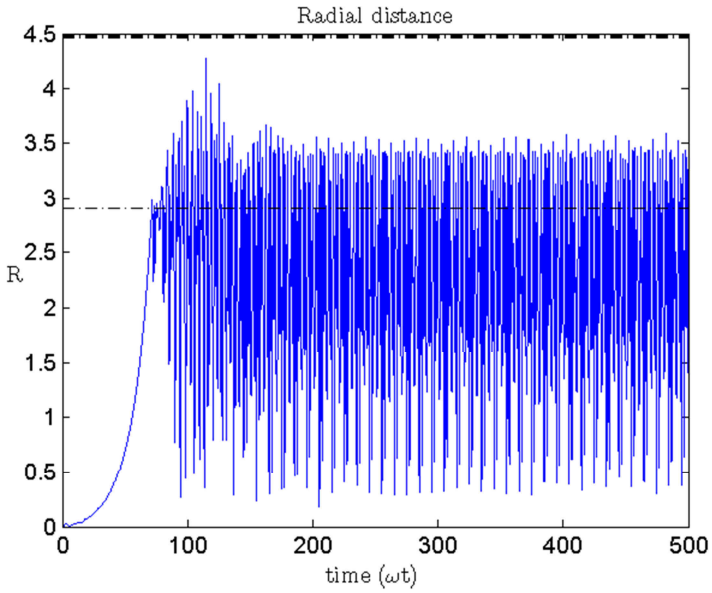


**Figure 3-24**: Radial distance of the disc center. It does not hit the wall, but repeatedly hits the pins.

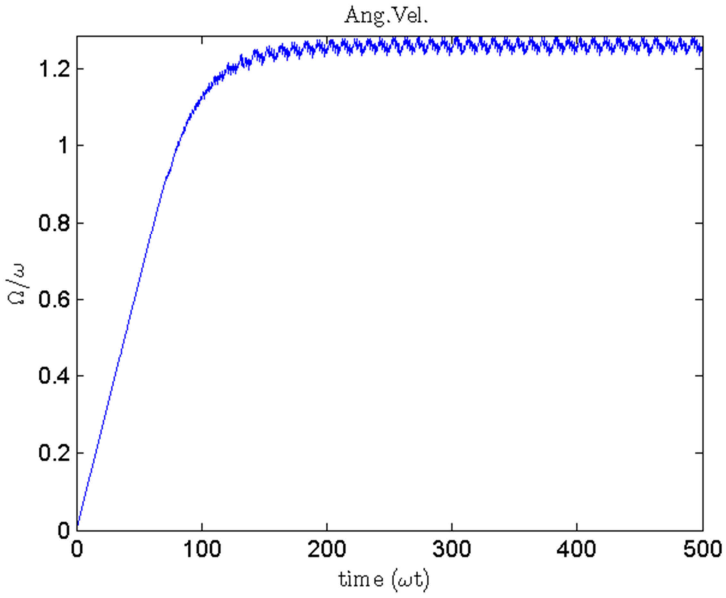


**Figure 3-25**: Although the angular velocity surpasses the critical speed, it is unable to reach higher velocities.

As seen in Figure 3-23, Figure 3-24 and Figure 3-25 the applied minimum torque is not enough to reach the stability. So a new case is presented, whose applied torque is five times greater than the minimum torque.

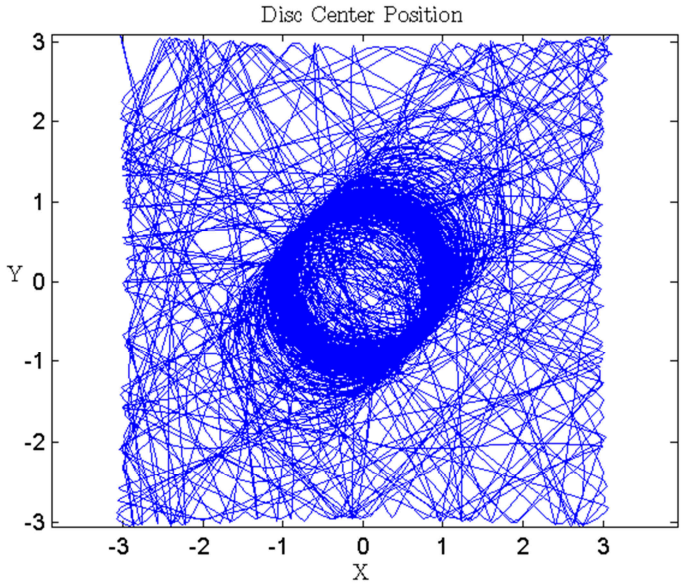


**Figure 3-26**: The disc center position with higher torque. The circular region shows a more stable orbit away from the wall and the pins

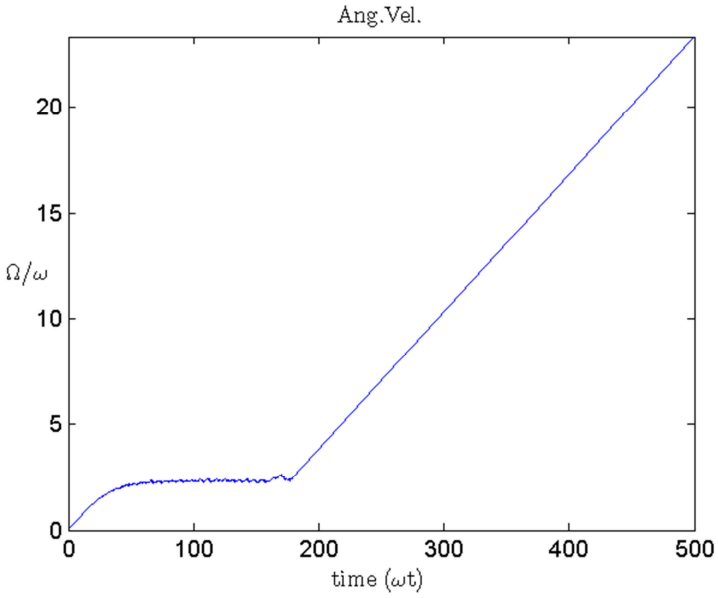


**Figure 3-27**: The angular velocity's slope indicates that it can accelerate after a series of hits on the pins.



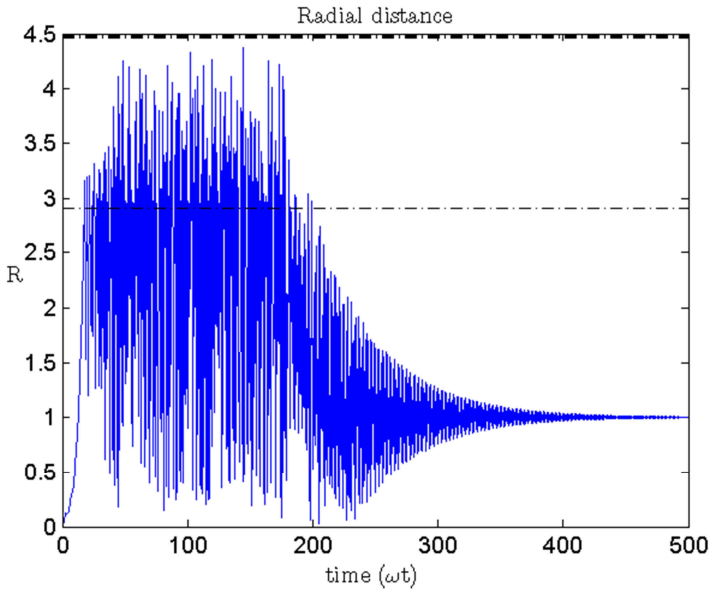


**Figure 3-28**: Radial distance. Does not touch on the wall and stabilizes at 1.

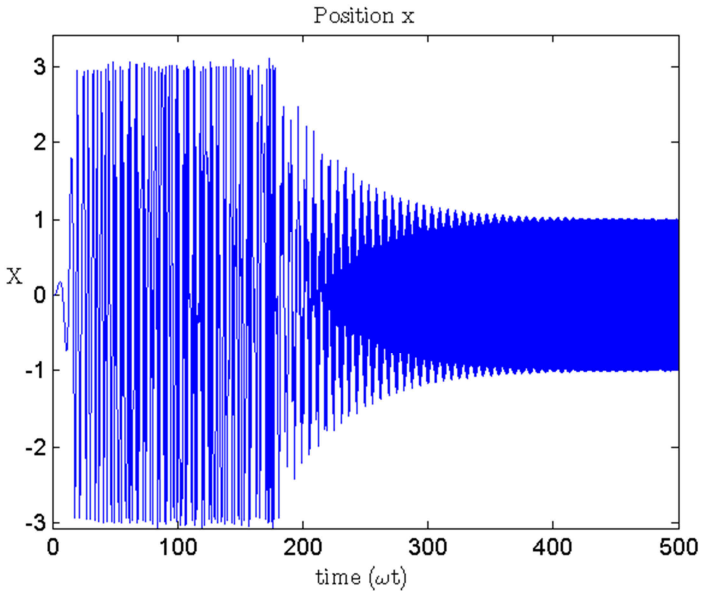


**Figure 3-29**: Oscillation of the horizontal coordinate $X$.

Figure 3-28 shows after $\tau = \omega t = 180$ a gradual decrease of the radial distance. It resembles the behavior theoretically shown in Figure 2-6 and Figure 2-7 where after the critical speed, or resonance frequency, the radial distance value $\boldsymbol{r}$ converges to the value of $\varepsilon$. This ensures of accuracy of the programs.

Through the simulation it was confirmed that it is possible to reach more stable orbits inside the bearing preventing it to collide and rub on the wall. By restraining the movement the pins do their job, the disc bounces on them and stays far away from the wall. The amount of torque required to accelerate the disc varies from each set up of rotation machine. It differs when the relationship between the radii of the disc and the dry friction coefficient.

# 4
# The test rigs

As part of the whole analysis of a new concept, an experimental part is required, so that a confirmation of what was simulated or stipulated theoretically is capable of happen in real machines. It was decided the test should progress step-by-step described in the following sectinos until it reaches its final stand. Besides, we preferred to use the tools available in the laboratory and the test rigs already developed from past works. Works from (Segayer, 2000), (Alvarado A. E., 1999) and (Lahiri, Santos, Weber, & Hartmann, 2012) provide a basis of study and opportunities to improve them.



## 4.1.
## Sensoring

### 4.1.1.
### Measuring position

The sensors used are the inductive proximity sensors made by Balluf®. They convert distance to electric current when metallic objects come closer. They have a rather linear region from 1.75 mm to 6mm: getting closer the current does not change and at larger gaps, it slowly saturates too. Consequently the sensor must be calibrated and positioned with a gap of 1.75mm from the nearest position of the disc rotor. Figure 4-1 is a chart from its datasheet which exhibits the current correspondence to the distance. Also it was established as origin the center of the safety bearing, considered as the zero point and the circular gap, previous determined theoretically as $r_0$, as having a range from $-1$ to $1$. Figure 4-2 allows us to visualize the coordinate system.

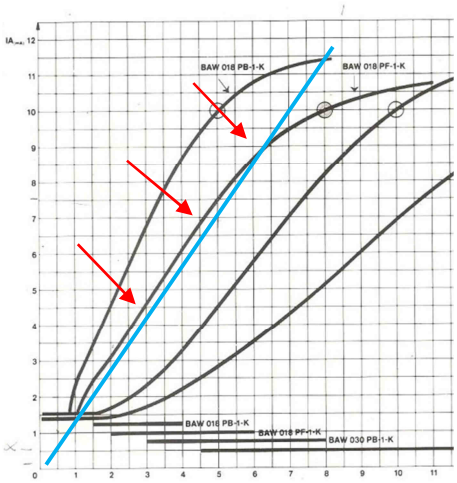


**Figure 4-1**: Current (mA) versus distance (mm) of the inductive sensor. The arrows point to correct curve. The blue line approximates the linear regions (Balluf, 1996).

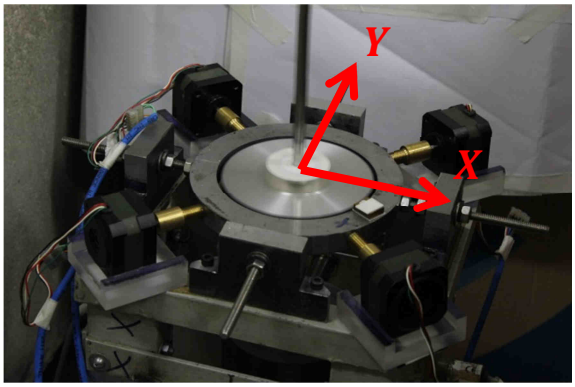


**Figure 4-2**: The coordinate system of the test rig.

A small board with resistances of 1kΩ nominal is used to convert the provided signal to voltage for sampling. They are supplied by a power source of 26V DC and the acquisition terminals are the electrical potential difference between the resistance terminals, see as sketched in Figure 4-3.

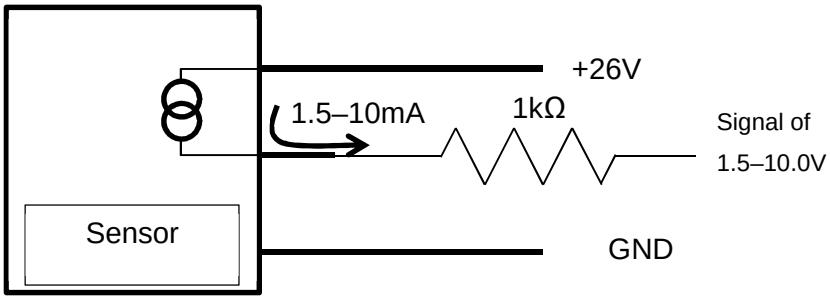


**Figure 4-3**: The sensor assembly diagram (Balluf, 1996).

### 4.1.2. Angular velocity

Another important magnitude to be collected and analyzed is the angular velocity. It is measured using a single Hall sensor with a TTL (5V) power source. It works similar as a transistor; when there is no magnetic field it closes the input terminal with the signal output. As the magnet approaches it changes and closes the signal with the ground terminal. Therefore, without any magnets in the proximity the output is 5V, on the contrary it is 0V. The small electronic device is seen in Figure 4-4. A small magnet $1\text{cm} \times 0.2\text{cm}$ of size is attached to a very light plastic disc on the top of the shaft. At every passage of the magnet, an inverted pulse is generated to the acquisition board.

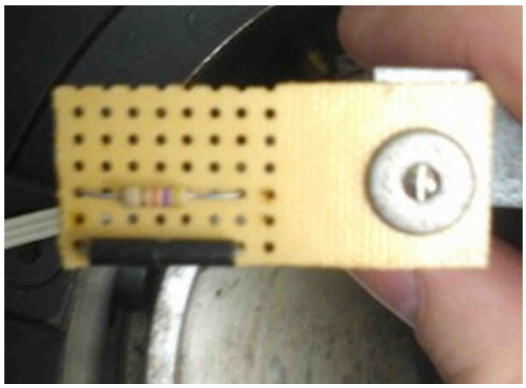

**Figure 4-4**: Hall sensor.

## 4.2. Shaft and rotor

From the beginning the shaft material was chosen to be steel, because of the availability in the laboratory and its well-known properties. The shaft has 1m of length and 8mm of diameter. It is precision manufactured, so that one can infer that it has a homogeneous mass distribution. It already has been used several times in past works and therefore before assembling and testing the skewness of the shaft was measured using a high-precision dial indicator and a standardized test rig, Figure 4-5. The maximum deviation measured from the shaft is 0.1mm, which was considered irrelevant for the experimental analysis.

**Figure 4-5**: Evaluating the skewness of the shaft.

## 4.3. The step motor

The step motor is a frequent tool in engineering and is a major component in different machines as actuators, like printers, robotic joint's motors and in automated machines in the industry. A step motor gives the advantage of working with discrete angles, but lacks in feedback control and modeled torque equations, (Cardozo, 2012). It works as an open loop control mesh. The motor receives a series of pulses and by each pulse the rotor moves the same amount of angles. They were used in the past in floppy discs drives to control the reading head position. The ones used in this work are four phase motor of 1.8°. It means that there are

necessary 200 pulses to make a full turn. Several configurations of setting the order of the phases are possible. The most common is a sequential one, where the each pulse is directed to one phase only. The next pulse goes to the following phase.

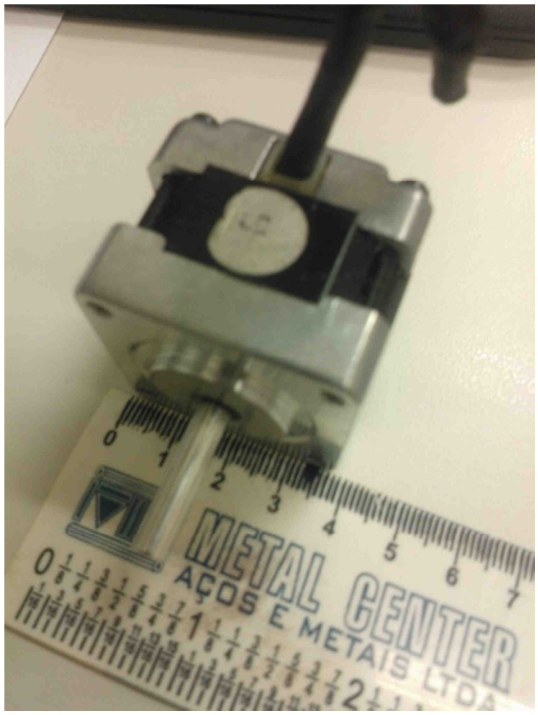


**Figure 4-6**: Size of the step motor.

## 4.4. The pin assembled prototype

The prototype was built to see the accuracy and the speed when the motion goes forth and back. It is a concept design that will serve as inspiration for the final test rig. It consists of three small walls and a block of acrylic, two rods, a step motor and a bronze round with a 1.25mm per turn screw. The motor is mounted and fixed on the block and its output shaft attached to a bronze rod. The steel rods work as a linear rail where the block can have a sliding oscillatory motion when moved due to the motion of the bronze screw in a fixed support. The photography from Figure 4-7 shows the assembly of the prototype.

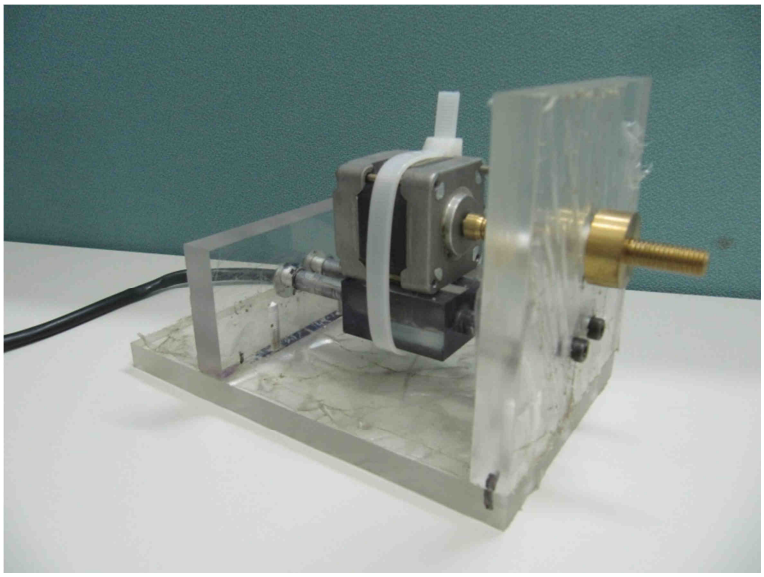

**Figure 4-7**: Prototype as assembled.

The prototype was controlled by a simple Labview® program which generated the chain of pulses to the phases. A measuring clock is positioned on the bronze rod end and adjusted the needle to mark zero, see Figure 4-8. The purpose of this test is to see whether the motor is capable to pull itself, if it loses a step and check the rotational speed.

By applying a series of 1000 pulses at 10 milliseconds the needle showed a variation of 5 to 10 microns $(10^{-6}\mathrm{m})$. But by turning back it came back to zero. The reason to this small error is that the prototype is not fixed on the table it moves a little bit. However, the test showed that the motor was capable of translate itself with an acceptable accuracy.

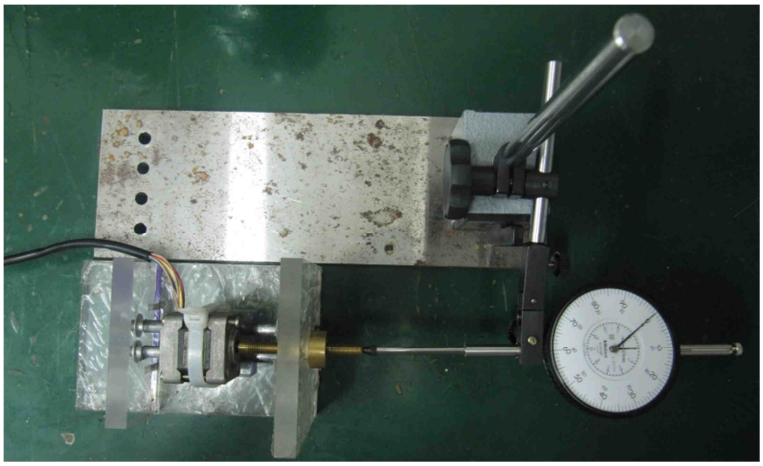

**Figure 4-8**: The prototype and the dial indicator.

## 4.5. The first experiment

In the following a rotor stator setup consisting of a disc suspended by a compressed air cushion in a metal cylinder stator is investigated. The aim of the project is to discover and describe trends in rotor stator contact dynamics, when the rotating rotor is excited by an impulse.

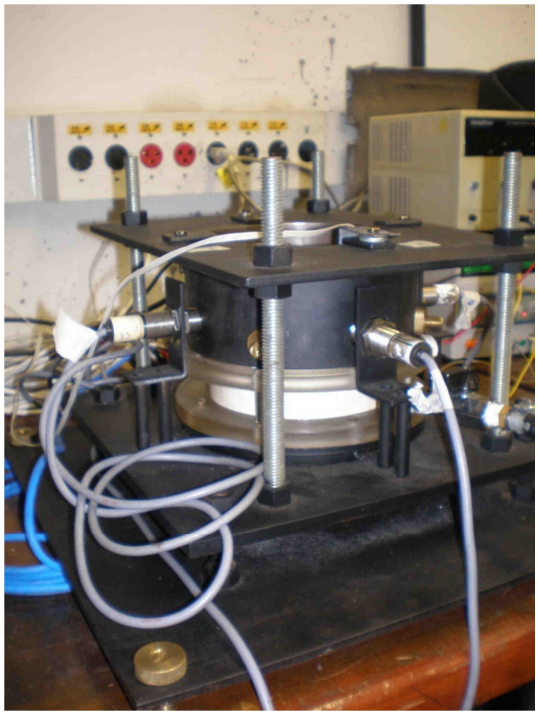

**Figure 4-9**: Test rig number 1.

The setup is a disc suspended by an air cushion obtained injecting compressed air through the basis of a metal cylinder. Four sensors embedded in the metal stator measure the disc location in the two lateral directions, with an approximate minimum distance of 1.75 mm between each sensor and the measuring surface on the disc. The measuring interval was for all tests one measurement per 10ms. The displacement readings were analog and the angular velocity readings digital. The concept design is illustrated in Figure 4-10, a vertical view in Figure 4-11 and a picture of the experimental setup above in Figure 4-9.

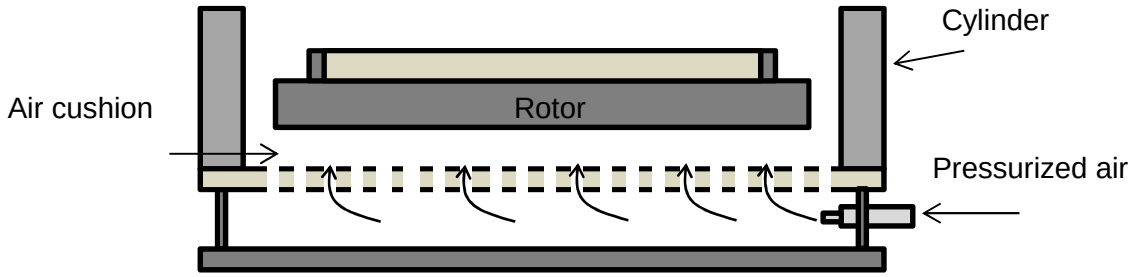


**Figure 4-10**: Illustration of the pressurized air levitating the rotor inside the cylinder (Segayer, 2000).

The minimum distances for each configuration (with pins and without pins) were determined by conducting three tests where the disc were positioned as close to each sensor as possible. The global minimum for the three tests were then found and used in the following calculations. For conducting the rotation tests the disc was spinned by hand. For the impact measurements, an impulse was exerted in the center of the disc once it had reached stable rotation, causing disc cylinder-pin contact.

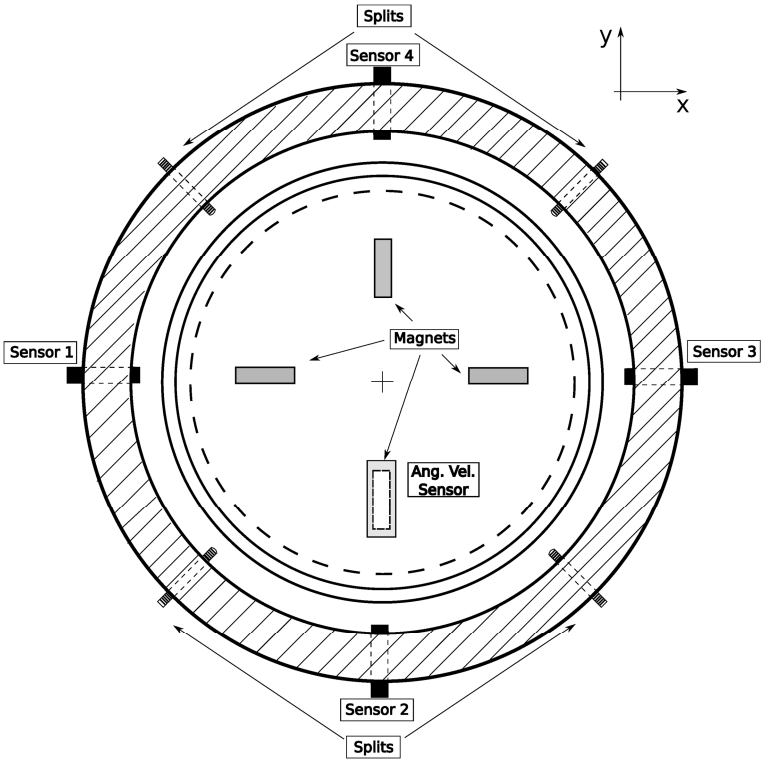


**Figure 4-11**: Vertical view of the rotor stator arrangement (Fleischer, 2011)

The first disc (in the following named the acrylic disc) is a three stage disc with an acrylic lid and bottom, but a polished metal annular piece and with magnets mounted on top in a 90 degrees arrangement. Its total weight is 472.5 g. The second disc (in the following named the metal disc) is also a three stage disc but with metal bottom and middle pieces, and with the same acrylic lid as the first disc. The total weight of the metal disc is 1543.3 g.

The position of the center of the disc in time is found by calculating an average between the two sensor signals in one direction. The maximum value for each sensor is subtracted from each reading and then divided by the full sensor span in order to normalize the sensor readings, as follow from equations (99) and (100).

$$x_1 = \frac{x_1 - x_{1,max}}{x_{1,max} - x_{1,min}}, \qquad x_2 = \frac{x_2 - x_{2,max}}{x_{2,max} - x_{2,min}}, \tag{99}$$

$$y_1 = \frac{y_1 - y_{1,max}}{y_{1,max} - y_{1,min}}, \qquad y_1 = \frac{y_2 - y_{2,max}}{y_{2,max} - y_{2,min}}, \tag{100}$$

$$X = \frac{x_1 + x_2}{2}, \qquad Y = \frac{y_1 + y_2}{2}. \tag{101}$$

The functions *polyval* and *polyfit* from Matlab® are used to fit a second degree polynomial to the angular velocity data.

The angular velocity signal is digital and displays ones when there is no magnet reading and 0 for a magnet reading. Since the time steps are fixed to 10ms the angular velocity is calculated as the distance between every 0 reading which is larger than 1 (more readings typically occur on one magnet), $\Delta d$ divided by $\Delta$t and multiplied with $2\pi$ to get it in radians per second.

$$\Omega = \frac{\Delta d}{\Delta t} \cdot \frac{2\pi}{4} \tag{102}$$

In equation (102) the one fourth factor appears, because of the four magnets on the lid and as such each reading corresponds to only one fourth of a rotation.

### 4.5.1. Results: no pins

The first experiments were conducted without the use of pins to see how the disc would react to an impulse exerted in the center once it had reached stable rotation. It was found that after a few impacts the disc reduced its angular velocity by a full annular rub. This was the case for both the acrylic and the heavy disc and two typical plots illustrating the accumulated disc center trajectory over the whole time range of the test can be found in Figure 4-13.

Looking more closely at these plots it is evident that the readings in the x direction are more aligned than in the y direction. This is likely due to one of the sensors not measuring directly perpendicular to the surface of the annular stator, but with a few degrees "turn" to one side or the other. The same tendency is seen in the measurements on the metal disc, but here it is the case for both the x and the y direction. The consequence of this is an average which is either too high or too low compared to the actual center of the disc. If we are only investigating the trends in disc stator contact this has however no significance.

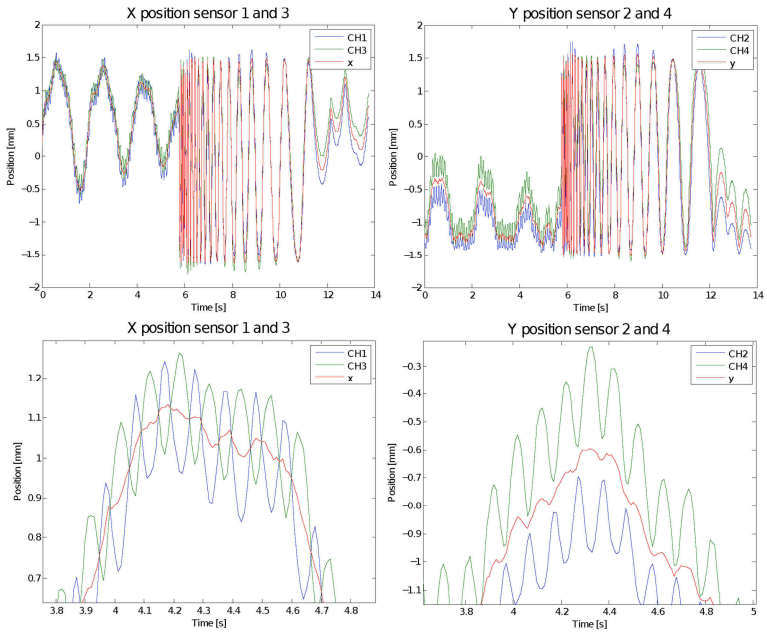


**Figure 4-12**: Readings from the channels and the average position, acrylic disc (Fleischer, 2011).

It can be noticed from Figure 4-13, that the metal disc seems to enter the full annular rub before the acrylic disc, which is also a general tendency for all the tests (Fleischer, 2011).

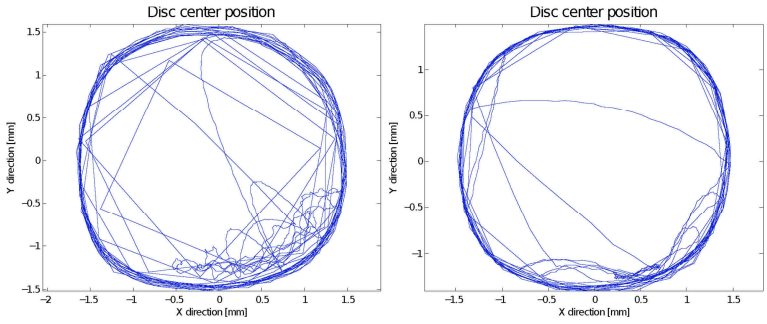


**Figure 4-13**: Movement of the disc center. **Left**: acrylic disc. **Right**: Metal disc (Fleischer, 2011).

### 4.5.2. Results: Minimum length pins

The term 'minimum length pins' means that the pins are at a minimum configuration, which just ensures that the disc makes contact only with the pins and not with the metal stator, as it is shown in Figure 2-14. The following average

position plots were standardized using a gap of 1 mm from the pin edge to the disc wall.

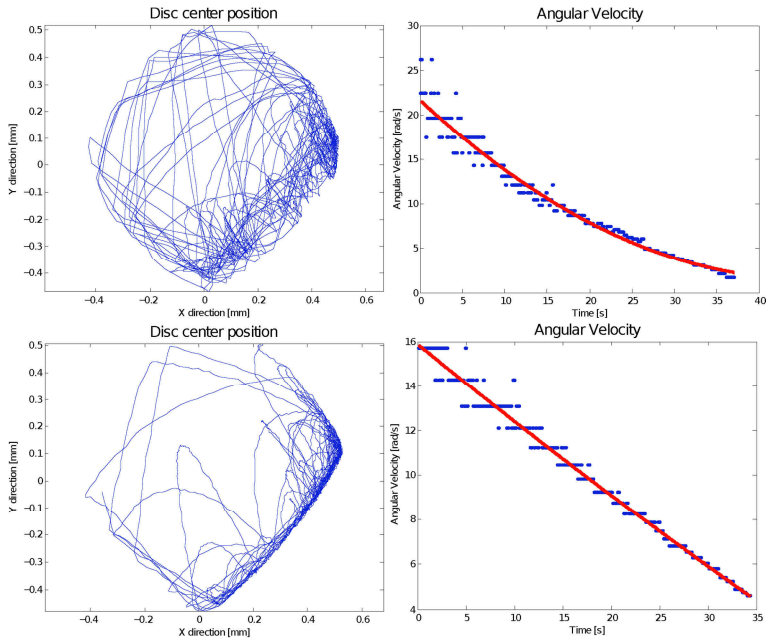


**Figure 4-14**: Minimum length pin configuration tests. **Top**: Acrylic disc. **Bottom**: Metal disc (Fleischer, 2011).

### 4.5.3. Results: Tight pins

The 'tight' pin configuration refers to a pin setup where the disc has very little space to move around because the pins restrict the movement. The results for the collision tests in this configuration are presented in Figure 4-15. From the position plot of the acrylic disc the crocked square shape is seen to be clearly defined, due to the restrictions of the disc movements. It is clear that the sample of points of the disc center represented in Figure 2-14 in the previous chapter, but with less space to move.

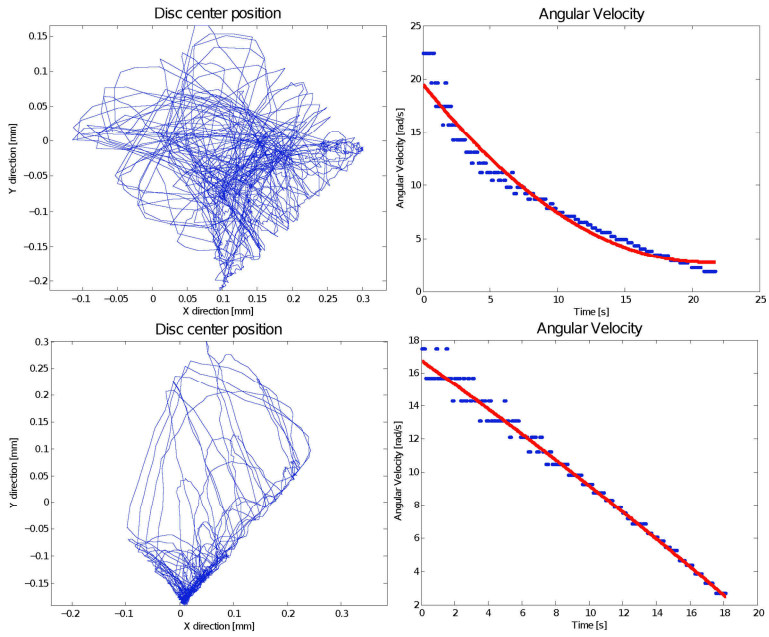


**Figure 4-15**: Tight pins configuration tests. **Top**: Acrylic disc. **Bottom**: Metal disc (Fleischer, 2011).

The angular velocity plots of both discs are relatively unaltered. However, the time the discs take to reach velocities below 4 rad/s is decreased in comparison to the minimum length pin configuration. From visually observing the tests this is due to an increased number of impacts and hence more energy dissipation over a shorter amount of time.

## 4.6. The final test rig

The final test rig is a full set for the study of rotors. The concept comes from the work of (Segayer, 2000) and the undergraduate project from (Aguiar, 2001) . Their project consists of a vertical rotor with one steel disc and a round bearing supported by four vertical rectangular shaped beams. The rotor has on the top a rolling bearing attached to an AC-synchronous motor; both are fixed on a C-shaped cantilever on the wall. Later it was used in the work of by (Lahiri, Weber, Santos, & Hartmann, 2012), where the ideas of pins were brought. The modifications done in this work are to introduce a second disc, much lighter and made of aluminum, to serve as the hitting disc in a retainer bearing that preserves

the original disc. Therefore a new round structure (that will contain the pins) will be introduced on the same plane as the lighter disc.

The steel disc has no bearing around it, only the position sensors are positioned on its plane. The angular velocity sensor is positioned on the cantilever where a light plastic disc is with one small magnet is fixed on the shaft. The structure of the retainer bearing received a small support for the new surface with pins and the step motors trails. The trails are small acrylic blocks glued to the structure and the step motor is allowed to slides in radial direction. The step motor's axis has a bronze screw, which is the active pin. The whole setup is shown in Figure 4-16.

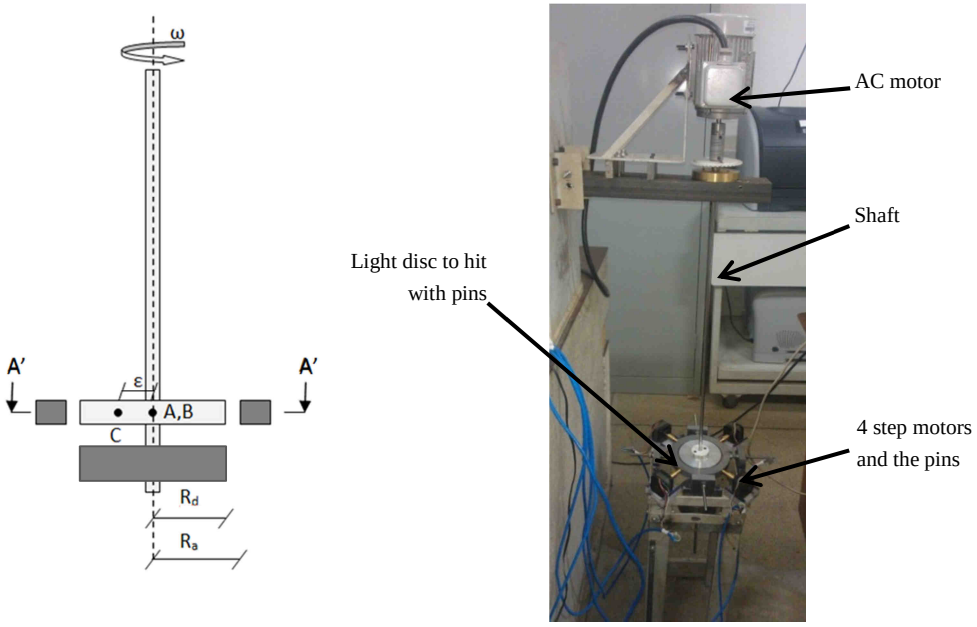


**Figure 4-16**: Setup of the final test rig. **Left**: Sketch of the discs. **Right**: The real assembly.

### 4.6.1. Acquiring and actuating the system

#### 4.6.1.1. Angular velocity

The rotor has a free end and the other coupled to an AC motor, which gives it angular speed. The motor is controlled by a frequency inverter; which changes the frequency of electric grid to a desired one. Unfortunately, by now, it was not

possible to change the frequency automatically, only manually and direct on its display.

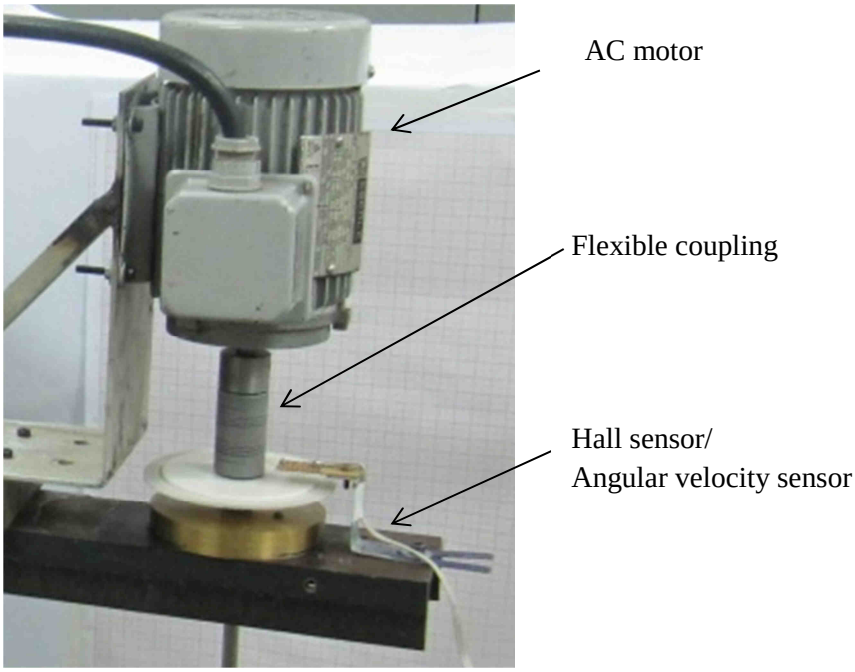


**Figure 4-17**: Coupling motor/shaft.

The angular velocity is measured in the same as the previously experiments, but with one difference: There is one magnet on the plastic disc, so each pulse represents one angular revolution. Equation (102) is multiplied by four to give the exact number of revolutions per minute.

The motor specifications are:

- Three phase 2-poles induction motor
- Externally sealed;
- Mass: 3.3kg
- Power: 1/6 (0.12KW)
- Rotation: Variable, controlled by frequency inverter
- Nominal voltage: 220V
- Nominal current: 1.1A

### 4.6.1.2. Acquisition boards

Two I/O[1] boards were used in the experimental analysis. The NI-6229 from National Instruments® and the Arduino Uno(CC). The NI-6229 is a powerful laboratory tool with four 16-bit analogs outputs, thirty-two 16-bit analog inputs and forty-eight digital I/O. It is already assembled and communicates with an USB cable with a regular PC. From the computer the user can program with the software Labview® the processing of the signals.


**Figure 4-18**: The NI-6229 acquisition board with its lid open used in all experimental parts.

The Arduino UNO(CC) board is well known nowadays because it is fitted to a huge variety of uses. It has a processing unit, thirteen digital I/O and five analog inputs. A small programing with a PC-interface, its programing language is similar to C, so one can develop innumerous types of programs and embark them on the electronic board.

The flow of data shown in Figure 4-20, the proximity probes and the angular velocity sensor send their voltage to the NI-6229 board and then to the PC to be computed. The Labview® program and the NI-6229 analyze all data and change information with the Arduino board. The Arduino is responsible to generate the series of pulses to the step motors drive.

[1] Input & Output

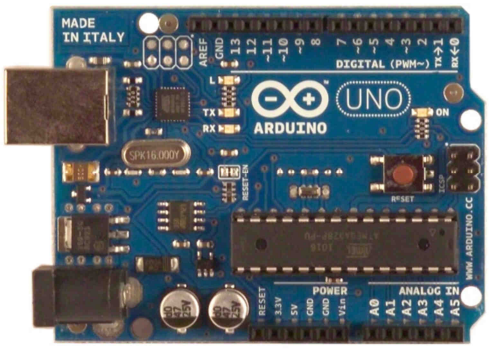


**Figure 4-19**: The Arduino board showing its I/O ports and electronic components.

Two digitals signals are sent from the Arduino back to the NI-6229. A digital signal goes back to program when the chain of pulses ends and one that gives the status of the pins, whether they are inside or outside the bearing wall.

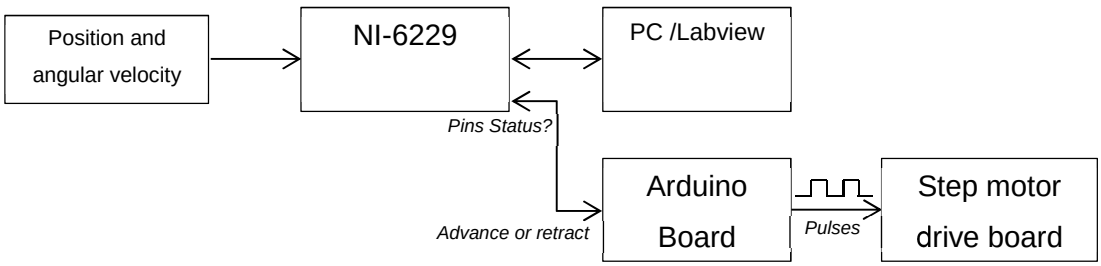


**Figure 4-20**: Information exchange diagram of the elements.

The pins stop to screw when the series of pulses end.

### 4.6.2. Labview Software and Controlling

Labview® is a block programing tool, whose blocks have embedded programs and the functions communicate through lines. The program is responsible to optimize the line codes. The advantage of this kind of software is to allow the user to have a panoramic view of the program and the flow of data inside it. Figure 4-20 and Figure 4-21 are pictures taken from the screen.


**Figure 4-21**: Labview control screen.



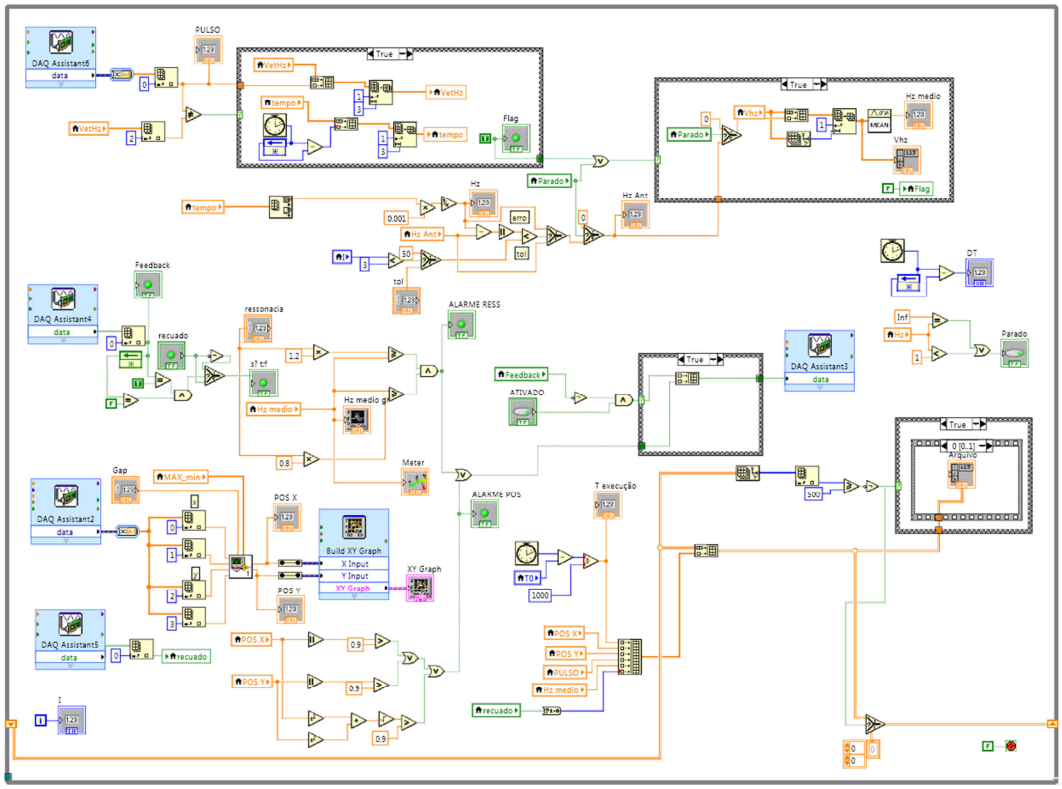

**Figure 4-22**: Labview block program.

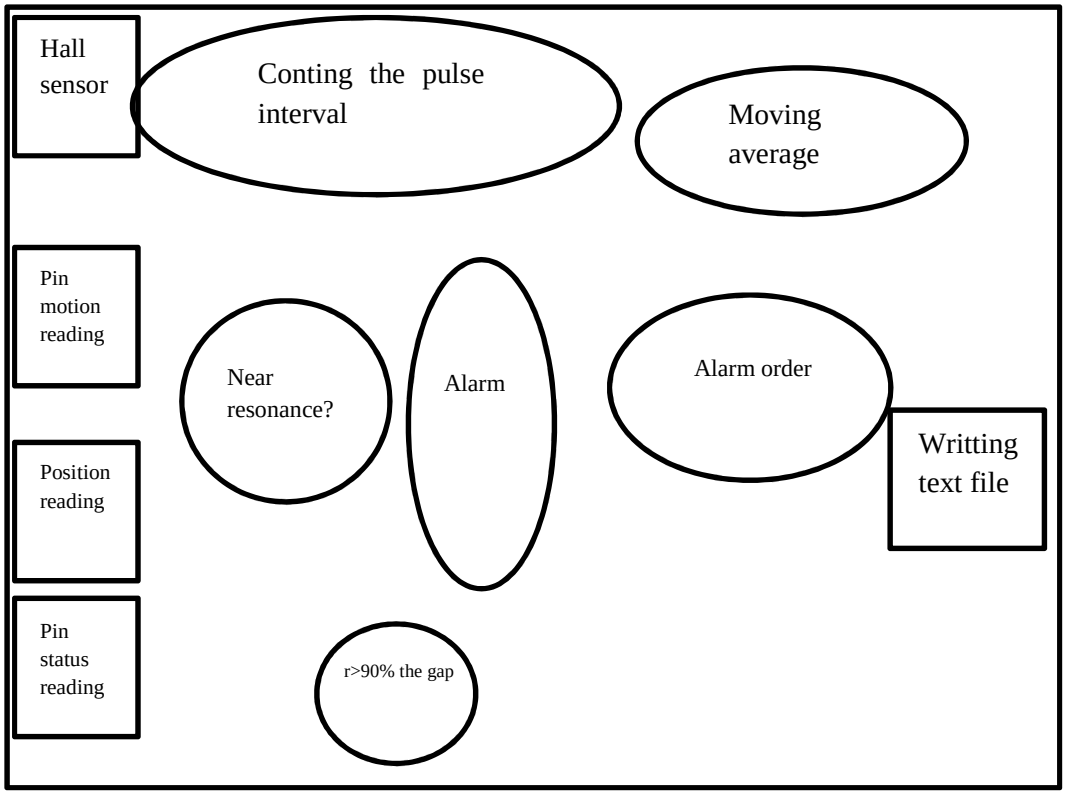


**Figure 4-23**: Detailing the Labview program.

Due to high noise gathered by the angular velocity small data processing must have been done. Mean time between the velocity two positive transitions of the velocity pulses and a moving average of five data was implemented as well whist the running experiment.

There were two types of alarms that triggered the Arduino board to generate the pulses. A resonance alarm and a position alarm. The resonance points should be identified before running the experiment and set as variable to the program. They are explained in the next section as the eigenfrenquencies of the beam. Additionally, a position alarm is present in the controlling logic too. The position measured by the proximity probes is compared against the gap. The rules for controlling the pins are:

*If the measured angular velocity is near ±20% of the known resonance or if the measured position reaches 90% of the gap, an alarm of actuation of the pins is set to ON. Otherwise, the pins stay as they are. If the pins are already advanced*

*and the alarm is set to ON, no action is taken. With no angular velocity the pins are always retrieved.*

### 4.6.3. Vibration modes

Although the beam is much lighter than the mass of the metallic disc making the center of mass virtually be on the disc, as the rotor rotates, the beams induces natural modes shapes. The shaft is free in one end and it can be considered only supported, since the coupling shaft-motor and the upper ball rolling bearing allow the shaft to have an angular deflection, but no displacements. In other words, the shaft is in the condition known as hinged-free (Thomson, 1972).

Experimentally, three stages of high vibration were detected. One is at very low angular velocity, the other two, around 23Hz and around 75Hz. The first one is considered to be cause by a pendulum oscillation; the other two are visually categorized as the first and the second modes of a beam deflection. When the shaft rotates around a 23Hz the whole beam bends in the form of an arch. By rotating it around 75Hz, the shape of the deflection is different leaving a small region without moving, hence it is a nodal point. Further resonance points were not searched due to the high velocity we were leading with (75Hz equals to 4500RPM).

Theoretically, the natural vibration frequencies are calculated as follows.

$$F_{res} = \frac{1}{2\pi}\left(\frac{\beta}{L}\right)^2 \sqrt{\frac{\rho A}{EI}}.$$

According to Table 2.1, the hinged-free $\beta$ coefficients give the results

$$F_1 = 24.82Hz \quad \text{and} \quad F_2 = 80.59Hz.$$

The resonance frequencies match the experimental ones with errors of 5.3% and 6.9%. It is a quite satisfactory comparison of both experimental and theoretical.

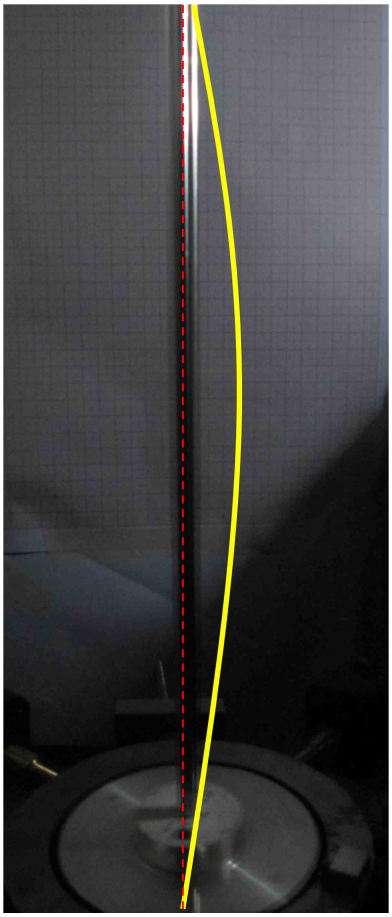

**Figure 4-24**: First resonance (23Hz) as seen experimentally with a strobe light. Yellow line is an exaggerated representation of the deformed shaft.

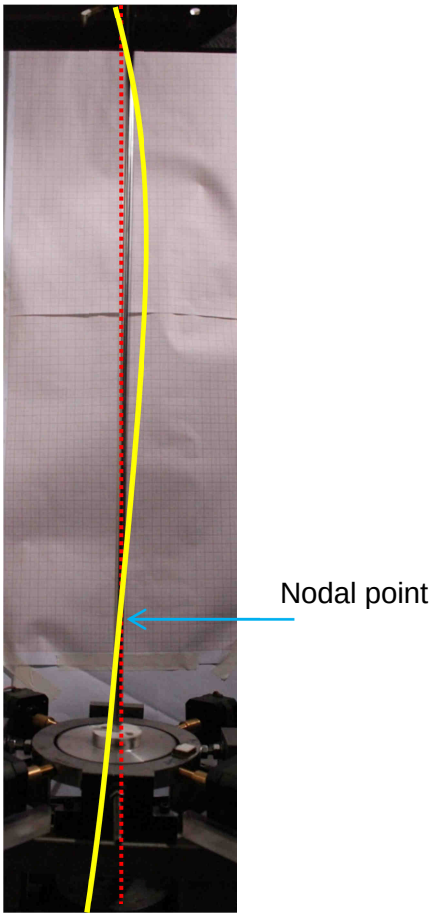


**Figure 4-25**: Second resonance (75Hz) as seen experimentally with a strobe light. Yellow line is an exaggerated representation of the deformed shaft.

## 4.7. Results and graphs

The gathered data is collected and shrunk in one text file for post-processing. Again Matlab® is the chosen software for plotting and analyzing. Three types of test were done:

- One without the actuation of the pins;
- the passage through the first resonance velocity of 23Hz;
- at high angular velocity an impulse is given to the shaft.

It was stipulated that in all test the nominal angular speed should not pass 50Hz (3000RPM) due to potential damage it can cause to the structure and the

pins. The motor can deliver high torques, so in order to simulate a low torque condition, the velocity grows slowly and manually operated on the frequency inverter's console-table.

The first test begun from zero velocity and as it gained speed the radial position increases until a long series of hits happen even when the disc was spinning at 50Hz. Also a full rub happen on the safety bearing wall. It took a while to the rotor to stay away from any critical speed. Rubbing and impacts are the worst conditions to be expected from a rotating machine. If it stays like this or operates like this for a long time, a dangerous situation may occur. This should be avoided at all.

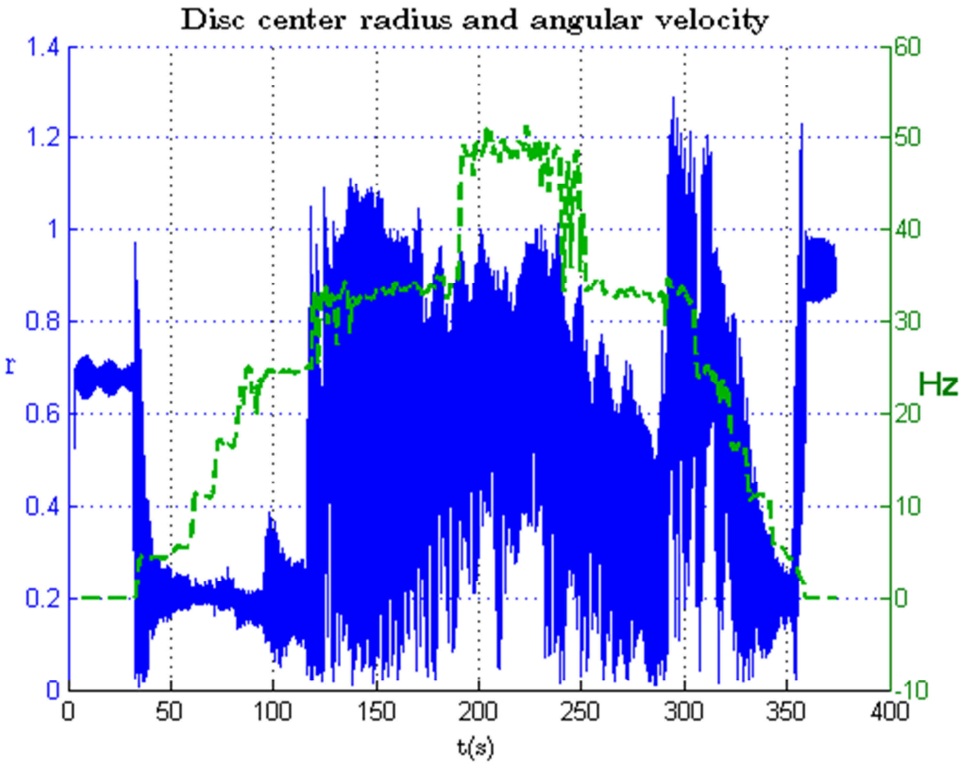


**Figure 4-26**: Radial position. No pin configuration

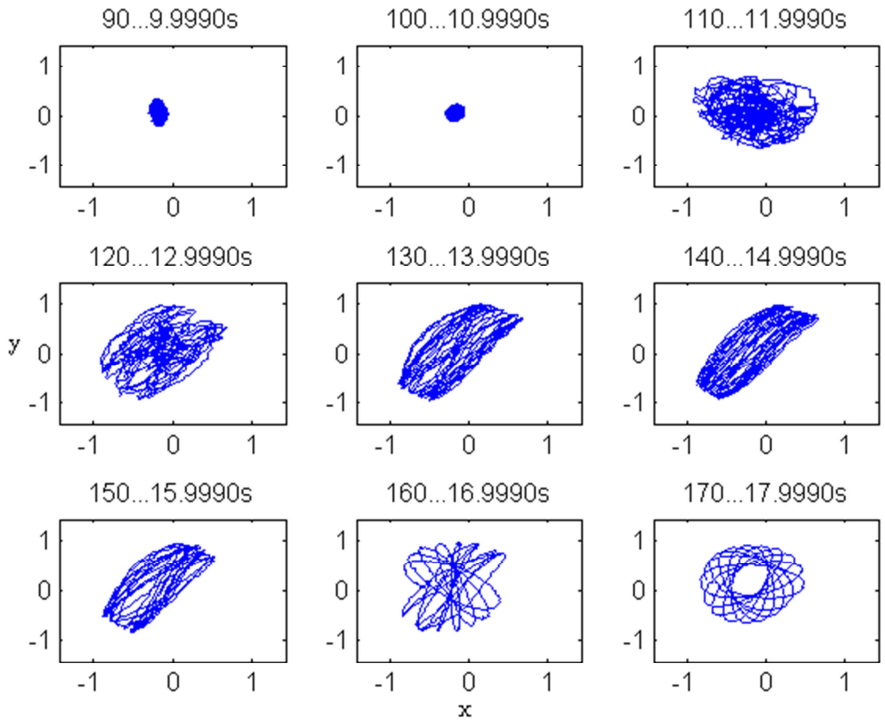


**Figure 4-27**: XY plot of the disc center.

The second experiment begins also from the resting condition. The disc accelerates and passes through the critical velocity until it rotates at 50Hz. However, the pins are active, and the controlling units are sending their signals to the step motors. As the rotor reaches 80% of the resonance point the pins are ordered to advance. The hits happen, but constrained. They are not on the wall, only on the pins. After 50Hz of rotational speed it stabilizes. Then, due to the vibration of other components like the C-shaped horizontal beam, the radial position induces a slow growth. Thanks to the position alarm, the pins prevent anything contact to the wall and push the disc back to a smaller orbit. In Figure 4-28 and Figure 4-29 the red dot means that the pins are inside the structure.

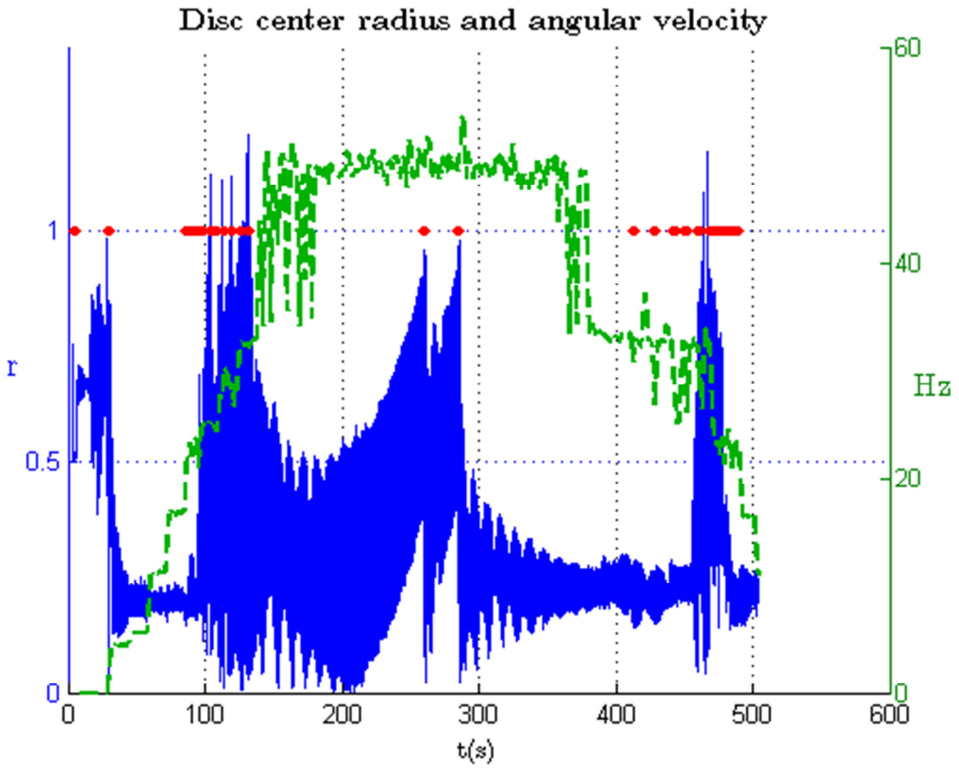


**Figure 4-28**: Radial position. Active pin configuration. Blue line: Radial position; Dashed green line: Angular velocity.

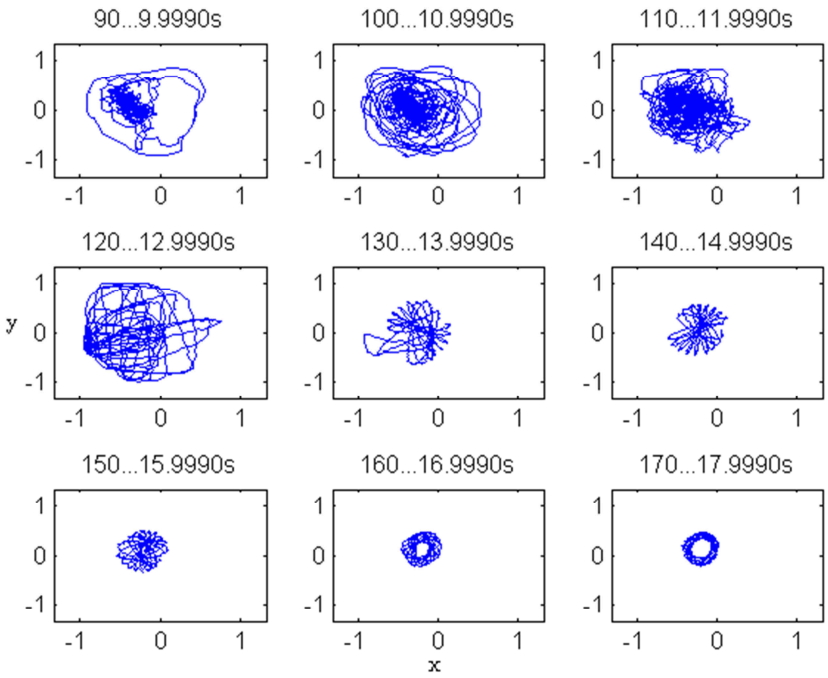


**Figure 4-29**: XY plot of the disc center. After collisions on the pins the rotor reaches stable orbits.

The third experiment is simpler; it measures the reaction time of the pins when the shaft receives an external hit. It starts with the rotor already rotating at 50Hz, when a bump is given to the shaft the disc indeed rubs the bearing wall, because the pins did not have enough time to counter-react, but as the pins are screwing themselves into the inner structure, the disc deviates from the wall and the disc stays on a safer orbit. Then, the same happened as the previous test, the radial position increases slowly. Likewise, the pins prevented the disc to rub the wall. Soon the rotor stays in a much safer orbit. The behavior can be seen in Figure 4-30 and Figure 4-31.

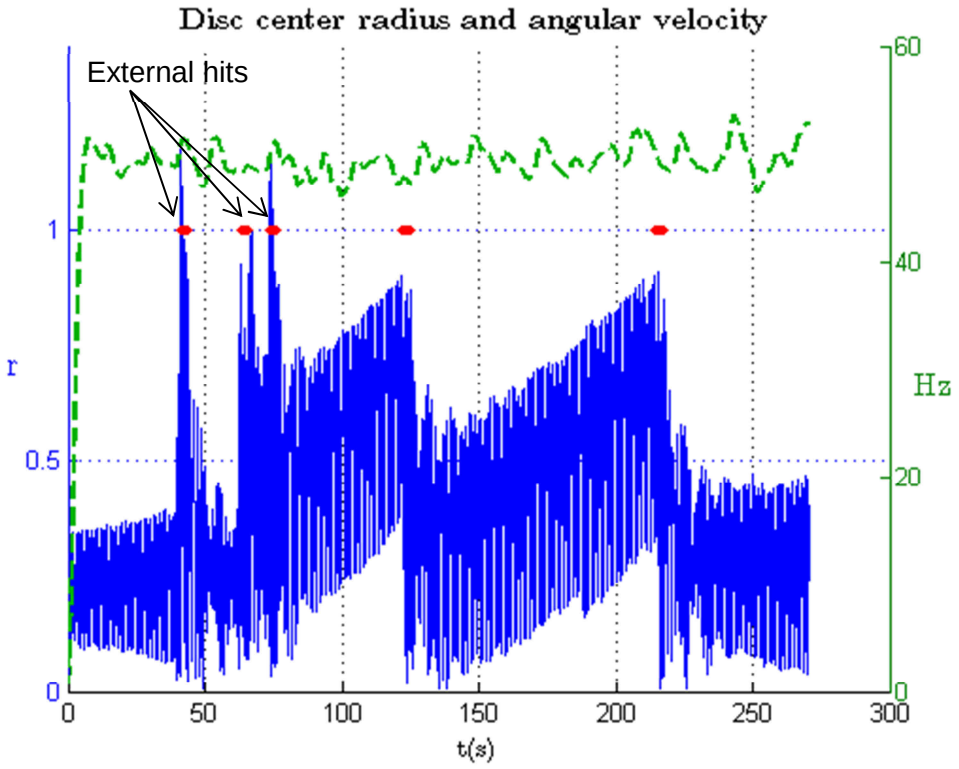


**Figure 4-30**: Radial position. Active pins configuration. Blue line: Radial position; Dashed green line: Angular velocity.

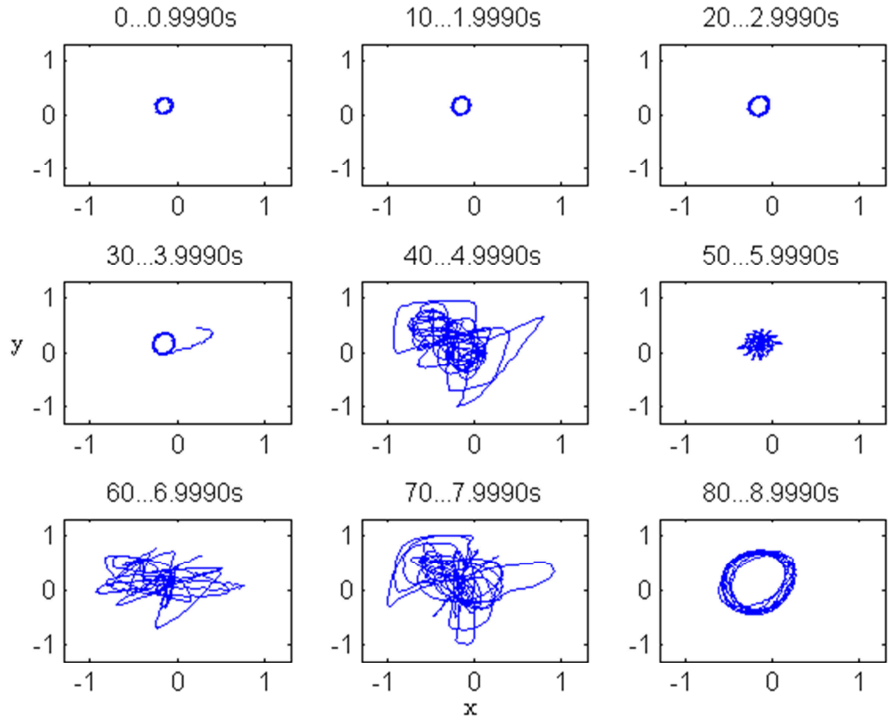


**Figure 4-31**: XY plot of the disc center. First hit from 3 to 4 seconds; Second hit from 6 to 7seconds.

# 5
# Conclusions

The use of pins inside the structure of a bearing has shown us that they can provide a good solution on restraining abnormal oscillatory movements of the rotors, which may occur by any reason. Numerical simulations in this work were created to model the impacts on the wall and on the pins. They showed that the behavior of the disc causes either a full annular rub, or a series of impacts of the disc on the wall.

The next simulated case models the behavior of the disc in the presence of pins. First, the disc is released from the origin at the critical speed. It starts with spiral trajectory and a few instants later, the disc begins to hit the pins, thereby losing a small amount of energy after each impact, and then stays on safer inner orbits. This is a much better choice than to expect it to rub on surface of the bearing. Since most rotating machines work above the critical speed, a new case considering an accelerating movement is conducted. It consists of including a constant torque term to the system of equations. In this case, the disc starts from rest and begins to impact several times on the pins. After a while, the disc returns to much safer orbits inside the bearing and accelerates without restriction.

The simulated results showed that the pins were able to prevent the full or partial annular rub, when the disc is about to collide on the bearing wall. Also, it is seen in the simulation that, when the disc is accelerated with minimum torque, causing high amplitudes of oscillation, the pins help the disc to surpass the critical speed without any hit on the wall.

Afterwards, the experiments were conducted to test the simulated behavior. The design of the pin has proved to be efficient and adaptable on the existing test rig. Experimental results on the first and on the second test rig demonstrate that the concept works and limits the oscillations during the expected resonance point

and they help to overpass it, or when the shaft receives an external thump. Moreover, the pins are automatic and move in and out when requested by a program. When not needed, they are automatically retracted, leaving a usual round bearing.

The concept of pins inside the retainer bearing is fitted for critical systems, which either rub constantly the wall, or have fragile elements and require that no impacts are allowed. Machines like magnetic bearings work in vacuum or thin air and, therefore, have low damping. Also, they rely on the electric grid, so safety measures are required in order to prevent a sudden blackout or instability of the grid. A safety bearing containing active pins could work as an emergency tool until the machine return to normality.

## 5.1. Difficulties and future works

In order to improve the work done, some features of the assembly should further analyzed and some others should be modified:

- The step motors can offer a good precision in its angular position, but lack in feedback control and, after a series of impacts on the pins, their position may be altered. Besides, the time to generate the chain of pulses was considered too long, causing a slow actuation.
- Controlling strategies: The control of the length of the pins using standard control techniques such as PID and Fuzzy logic should be implemented.
- Although the linear impact showed in simulation a good response, for a more profound and realistic mathematical modeling of the impacts, non-linear considerations are needed.
- The angular velocity sensor gathered data with high levels of noise, which should be minimized by standard filtering methods.
- Measurement of the impacts magnitude on the pins.

# 6
# References

Aguiar, R. R. (2001). *Interação Rotor/Estator em Máquinas Rotativas - Impacto com Rotação.* Undergraduate Project, PUC-Rio.

Alvarado, A. C. (2006). *Minimierung von Kontaktkräfte bei Anstreifvorgängen durch Regelung.* Doctorate Thesis, Technische Universität München, Angewandte Mechanik, Munich.

Alvarado, A. E. (1999). *Concepção de uma bancada para análise de fenômenos rotativos.* Master Thesis, PUC-Rio, Mech. Engineering Department, Rio de Janeiro.

Balluf. (1996). *Sensores de Proximidade Indutivos, Capacitivos, Optoeletrônicos de Campo Magnético, Ultrassônicos.* Technical Datasheet, Campo Belo, SP, Brazil.

Banakh, L., & Nikiforov, A. (2009). Backward Whirl of Unbalanced Shaft at Elastically Constrained Journal Bearings and Floating Seals Due to Mechanical Contact. *Proceedings of the 7th Int. Scientific and Practical Conference*, (pp. 234-240). Rēzekne, Latvia.

Bankh, L., & Nikiforov, A. (2009). Backward whirl of unbalanced shaft at elastically constrained bearings and floating seas due to mechanical contact. *Proceeding of the 7th International Scientific and Practical Conference, II.*

Bently, D. E., & Hatch, C. T. (2002). *Fundamentals of rotating machinery diagnostics.* Minden, NV: Bently Pressurized Bearing Press.

Braga, A. (2012). *Mechanical Vibrations.* Lecture's notes, PUC-Rio.

Campbell, W. (1924). *Protection of Steam Turbine Disk Wheels from Axial Vibration.* Schenectady, N.Y.: General Electric Co.

Cardozo, W. S. (2012). *Controle de motores de passo aplicado a um manipulador robótico.* Master Dissertation, PUC-Rio, Mechanical Engineering Department, Rio de Janeiro.

Chavez, R. G. (2003). *Dinâmica de um Rotor Horizontal em Apoios Elásticos.* Master Thesis, PUC-Rio, Departamento de Engenharia Mecânica, Rio de Janeiro.

Diken, H. (2000). Non-linear vibration analysis an subharmonic whirl frequencies of the Jeffcott rotor model. *Journal of Sound and Vibration.*

Ebersbach, P. (1989). *Rechnerunterstützte Methoden der Messwertfassung und Parameteridentifikation (Modelanalyse) und ihre Anwendbarkeit auf rotierende Maschinen.* Doctorate Thesis, Universität-Gesamthochschule Kassel, Institut für Mechanik, Kassel.

Eckert, H., & Popprath, P. (June de 2007). Nonlinear dynamics of a rotor contacting an elastically suspended stator. *Journal of Sound and Vibration, 308*, 767-784.

Ehrich, F. (November de 1969). The Dynamic Stability of Rotor/Stator Radial Rubs in Rotating Machinery. *J. Eng. for Industry, 91*(4), pp. 1025-1028.

Fleischer, P. F. (2011). *Experimental Rotor Stator Contact.* Research Report, PUC-Rio/DTU, Rio de Janeiro.

Fumagalli, M. (1997). *Modelling and Measurement Analysis of the Contact Interaction between a High Speed Rotor and its Stator.* Doctorate Thesis, Swiss Federal Institute of Technology, Zurich.

Gasch, R., Markert, R., & Pfützner, H. (1979). Acceleration of unbalanced flexible rotors thorugh the critical speeds. *Journal of Sound and Vibration, 63*(3), pp. 393-409.

Gasch, R., Nordman, R., & Pfützner, H. (2002). *Rotordynamik.* Berlin: Springer Verlag.

Gere, J. M. (2003). *Mechanics of Materials.* São Paulo: Thomson Learning.

Ginzinger, L., & Ulbrich, H. (2007). Control of a Rubbing Rotor Using an Active Auxiliary Bearing. *Journal of Mechanical Science and Technology*, 851-854.

Isaksson, J. L. (1994). *On the dynamics of a rotor interacting with non-rotating parts.* Linköping University, Department of Mechanical Design. Linköping, Sweden: Linköping of Studies in Sciences and Technologies.

Ishida, Y., Hossain, M. Z., & Inoue, T. (2006). Analysis and Suppression of Rubbing due to Contact in Rotating Machinery. *7th IFToMM.* Vienna.

Jiang, J., Ulbrich, H., & Chavez, A. (2006). Improvement of rotor performance under rubbing conditions though active bearings. *International Journal of Non-LInear Mechanics*, 949-957.

Kaidalov, V. B., Patrushev, V. L., Solov'ev, S. A., & Ruin, A. A. (2012). Simulation of Flexible Turbine Rotors in the Design of Safety Bearings. *Vestnik Mashinostroeniya*, 15-18.

Kent, W. (1950). *Mechanical Engineers' Handbook* (12th ed., Vol. Design and Production). New York, NY, USA: John Wiley & Sons, INC.

Lahiri, S., Santos, I. F., Weber, H. I., & Hartmann, H. (2012). On the Nonlinear Dynamics of two Types of Backup Bearings - theoretical and experimental aspects. *Journal of Engineering for Gas Turbines and Power, 134*, 112503-1/13.

Lahiri, S., Weber, H. I., Santos, I. F., & Hartmann, H. (8 de June de 2012). Rotor-Stator contact dynamics using a non-ideal drive - Theorectical and experimental aspects. *Journal of Sound and Vibrations*, pp. 4518-4536.

Lalanne, M. (1990). *Rotordynamics Prediction in Engineering.* England: John Wiley & Sons.

Markert, R., & Seidler, M. (1999, December 7). Analytically-based estimation of the maximum amplitude during passage through resonance. *International Journal of Solids and Structures*, pp. 1975-1992.

Markert, R., Pfützner, H., & Gasch, R. (1980). Mindestantriebsmoment zur Resonanzdurchfahrt von unwuchtigen elastischen Rotoren. *Forsch. Ing._Wes., 46*(2), 33-68.

Meggiolaro, M. (1996). *Modelagem de Mancais Hidrodinâmicos na Simulação de Sistemas Rotativos.* Master Thesis, PUC-Rio, Mechanical Engineering Department, Rio de Janeiro.

Schweitzer, G. (1989). *Magnetic Bearings* (1st ed.). Zurich: Springer-Verlag.

Segayer, A. M. (2000). *Análise do Processo de Contato entre Rotor e estator em uma máquina Rotativa.* Doctorate Thesis, PUC-Rio, Mech. Engineering Department, Rio de Janeiro.

Simon, U. (2000). *Rotor-Stator-Kontakt in polygonförmigen Fanglagern.* Doctorate Thesis, TU Braunschweig.

Szczygielsky, W. (1986). *Dynamisches Verhalten eines schnell drehenden Rotors bei Anstreifvorgängen.* Eidgenössischen Technischen Hochschule Zürich. Zurich: ADAG administration & Druck AG.

Tenreiro Machedo, J. (1994). *Motores Passo a Passo: Controlo e Modos de Funcionamento* (1 ed.). Porto: Publindústria.

Thomson, W. T. (1972). *Theory of Vibration with Applications* (1 ed.). Englewoods, N.J., USA: Prentice-Hall.

Weber, H. I. (2011). *Classical Mechanics.* Lecture's note, PUC-Rio.

Weber, H. I. (2011). *Rotordynamics.* Lecture's notes, PUC-Rio.

Zülow, D., & Liebich, R. (2009). Ein Aussenrollenlager als Fanglagerkonzept für magnetgelagerte Rotores. *SIRM 2009.* Vienna, Austria.

# Appendix A

This appendix has the values which were used in the numerical simulations.

**Table 2**: Parameter values used in simulations.

| | |
|---|---|
| $m = 2.46\,kg$ | Disc mass |
| $R_d = 0.05$ | Disc radius |
| $R_b = 0.055$ | Disc bearing |
| $\varepsilon = 1\text{mm}$ | Mass eccentricity |
| $\mu = 0.56$ | Friction coefficient (no pins) |
| $\mu = 0.08$ | Friction coefficient (with pins) |
| $k_1 = 482.54\text{N/m}$ | Shaft elastic coeficient |
| $c_1 = 0.012\,Nm/s$ | Damping coefficient (simulation |

# Appendix B

**Table 3**: Size of the components of test rigs.

| | |
|---|---|
| Shaft diameter | 8mm |
| Shaft length | 1m |
| Distance from the shaft end to the disc | 0,8m |
| Light rotor diameter | 10cm |
| Heavy rotor diameter | 10cm |
| Bearing inner diameter | 105.5mm |
| Diameter of the pin | 0,375in |

# Appendix C

This Appendix contains the isometric, lateral and superior views of the concept made with CAD software.

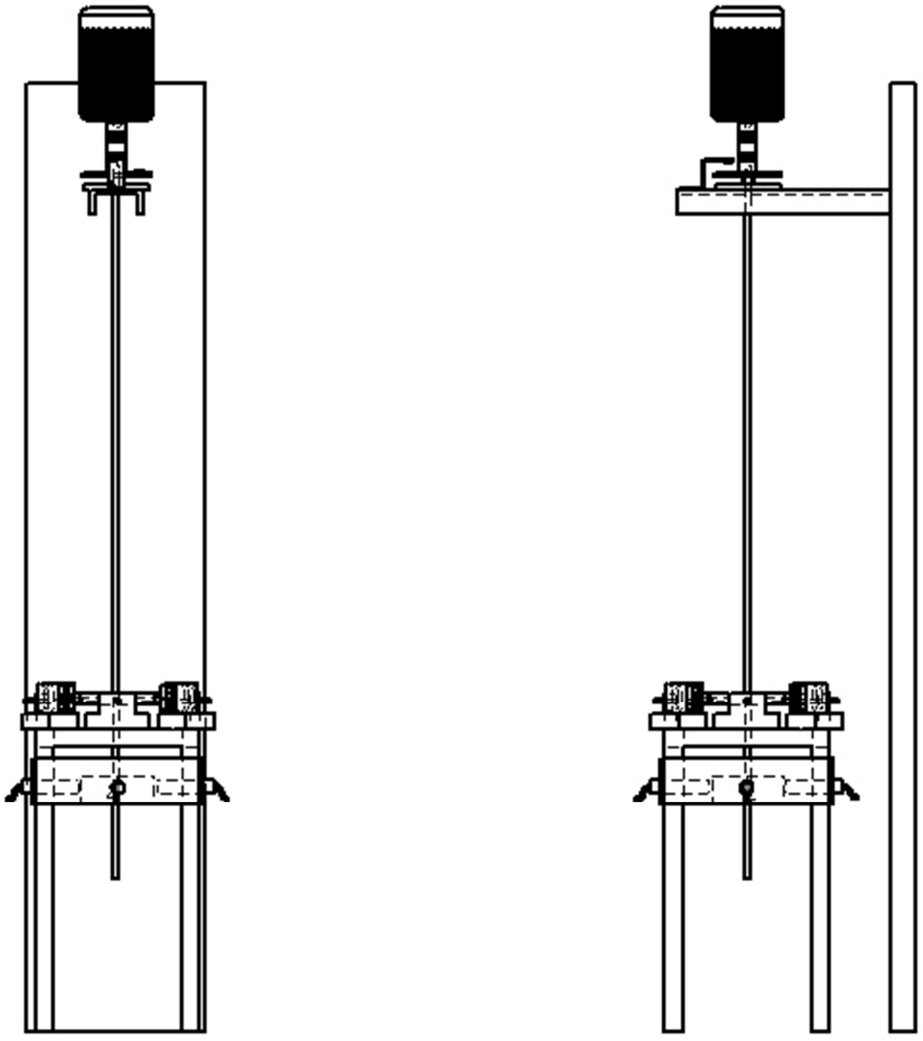

**Figure C-1**: Lateral views from the assembly.

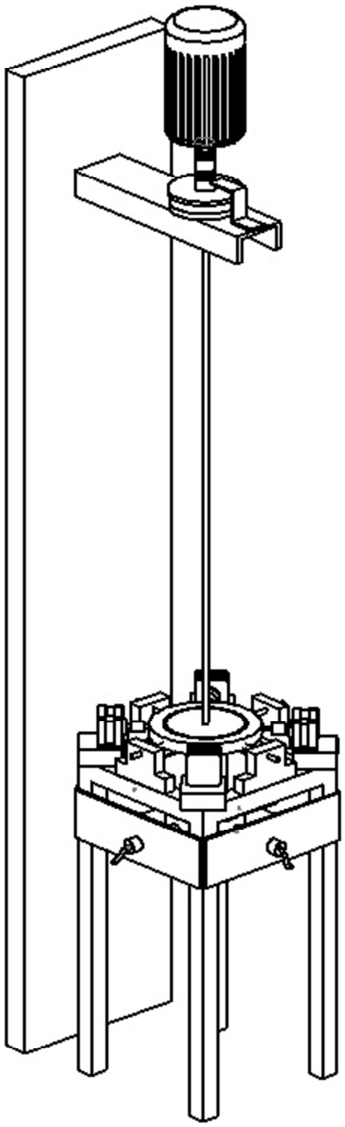

**Figure C-2**: Isometric view of the whole set up.

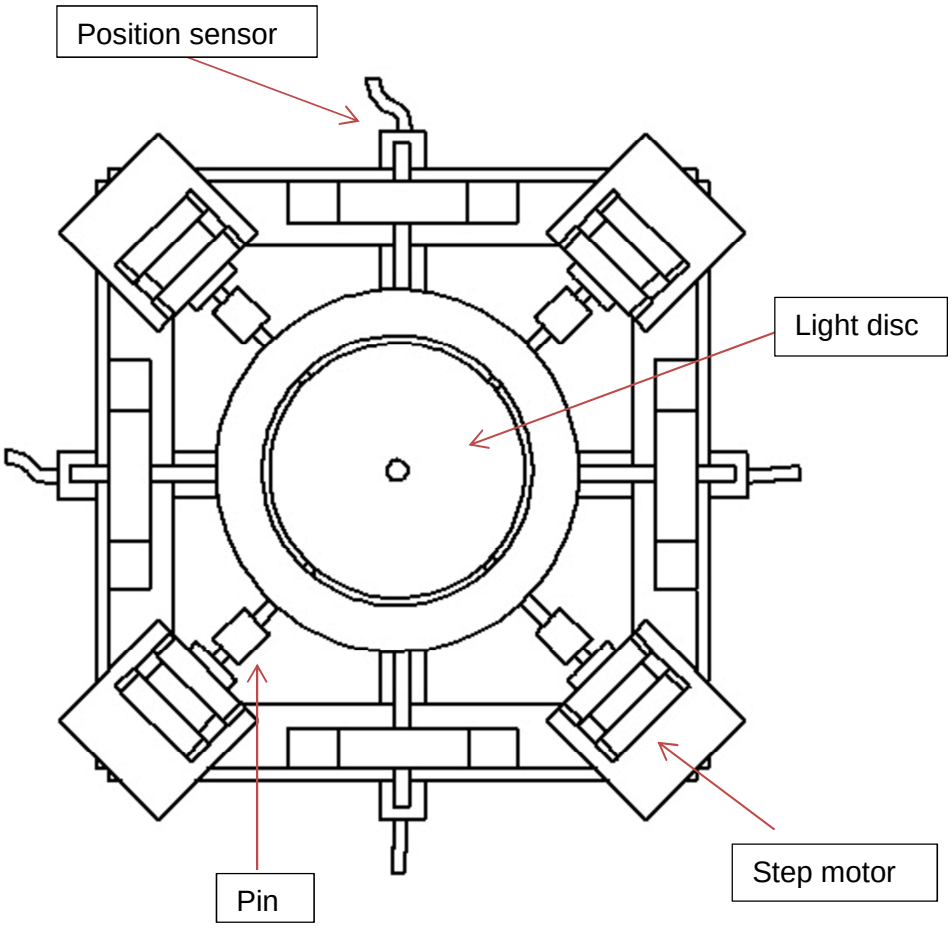


**Figure C-3**: Superior view without the AC motor. Representation of the positioning of the pins and stepmotors.